Indian Institute of Technology Guwahati

Doctoral Thesis

# Performance Enhancement in a Modal Wavefront Sensor and its Application to Free Space Optical Communication


Thesis submitted in partial fulfilment of the requirements for the degree of Doctor of Philosophy of the Indian Institute of Technology Guwahati.

**Santanu Konwar**

Computer Generated Holography Laboratory

Department of Physics

Indian Institute of Technology Guwahati

Guwahati, India.

May, 2019

*Dedicated to my Beloved Parents*

# Declaration

**Santanu Konwar**
Roll No. 136121029
Department of Physics
Indian Institute of Technology Guwahati
Guwahati, India
Email: k.santanu@iitg.ac.in

---

I hereby declare that the results embodied in this thesis is the result of theory and experiment carried out by me at the Department of Physics, Indian Institute of Technology Guwahati, Guwahati, India, under the supervision of **Prof. Bosanta R. Boruah**. This thesis has not been submitted to any university/ institute or elsewhere for the award of any degree, diploma or associateship.

Santanu Konwar

Date

# Certificate

**Prof. Bosanta R. Boruah**
Department of Physics
Indian Institute of Technology Guwahati
Guwahati, India
Email:brboruah@iitg.ac.in

---

This is to certify that the work contained in the thesis entitled **'Performance enhancement in a modal wavefront sensor and its application to free space optical communication'** by **Santanu Konwar** (Roll No. 136121029), a student of Department of Physics, Indian Institute of Technology Guwahati, for the award of degree of Doctor of Philosophy, has been carried out under my supervision.

The present thesis or any part thereof has not been submitted elsewhere for award of any other degree, diploma or associateship.

Bosanta R. Boruah

Date

# Acknowledgements

I would like to offer my sincere thanks and gratitude to my thesis supervisor Prof. Bosanta R. Boruah for his continuous motivation and support throughout my Ph.D. work. His constant guidance and valuable suggestions kept me in the right track during the course of my research work. The thesis could not have been presented in final finesse form without his constant help, guidance and encouragement.

My gratitude also goes to my Doctoral committee members: Prof. Alika Khare, Dr. Ashwini Kumar Sharma and Dr. Ramesh Kumar Sonkar for their encouragement, insightful comments and suggestions.

My sincere thanks also goes to the former and present HoDs of Physics, Prof. Saurabh Basu, Prof. Poulose Poulose and Prof. Subhradip Ghosh for providing me the opportunity to utilize different resources of the department to carry out my Ph.D. work.

I take this opportunity to thank Dr. Sidananda Sarma, Mr. Lokesh Chakravorty, Mr. Aditya Kalita and the entire staff of the Department of Physics IIT Guwahati for their service, help and encouraging advices.

I would also like to thank all my past and present lab members: Dr. Abijit Das, Dr. Md. Gaffar, Dr. Biswajit Pathak, Ranjan Kalita, S S Goutam Buddha, Nagendra Kumar, Karuna S. Malik and Akanshu Chauhan for the stimulating discussions and quality time that we had during the tenure of my Ph.D. work.

I am grateful to all my friends at IIT Guwahati for providing a smoothing environment and the necessary distraction from the stressful situations. My sincere thanks also goes to Dr. Partha P. Dey and Dr. Kamal K. Paul for making the stay in the hostel a joyful one. I would like to acknowledge all my close friends, Monuj, Pranjal, Bidyut, Dhanjit, Jishu, Bitu, Sajal and others for being with me in all the thicks and thins of my life.

I also take this opportunity to sincerely acknowledge the financial support from Ministry of Human Resource and Development (MHRD), Government of India during my Ph.D.

I am deeply indebted to my parents: Lt. Mukti Nath Konwar and Mrs. Bidyawati Konwar, my brother: Sorat Konwar and all other family members for their unconditional love and support throughout my life and my studies. Their patience and sacrifice will remain my inspiration throughout my life. Particular thanks goes to

my wife, Mrs. Shilpi Chutia, for her infallible love and support during my stressful and testing times. She has always been my strength and moral support.

Last but not the least, I would like to thank all my teachers at schools (Don Bosco High School Silapathar and Jawahar Novodaya Vidyalaya Dhemaji), at colleges (Dhemaji College and Silapathar Science College) and at the university (Gauhati University) for their personal and professional guidance and encouragement towards my journey to the present stage. I would also like to offer my sincere thanks to all the faculty members of IIT Guwahati for their valuable suggestions and encouragements.

# Abstract

Wavefront is a fundamental feature of a light beam. It can be defined as the surface constructed by the loci of points having the same phase or the points that correspond to equal optical path lengths starting from the source. When a coherent light beam such as a laser beam passes through certain medium or gets reflected by certain surface, the wavefront of the light beam gets modified in such a way that the modification is characteristic of the transmitting medium or the reflecting surface. Thus a plane wavefront after being transmitted by the medium or after being reflected by the surface may get distorted. Such distortions which are nothing but deviations in the phase profile from an ideal plane wavefront are termed as wavefront aberrations. Wavefront aberration if introduced may result in loss of information carried by the beam and it requires removal of the aberration to extract the original information. On the other hand the aberrations introduced by a reflecting surface can provide information regarding the profile of the surface roughness. The setup to measure the wavefront of a light beam is known as wavefront sensor. There is an important type of wavefront sensor called the modal wavefront sensor that can provide a direct estimation of the strength of the orthogonal aberration modes present in a beam of light. One of the most widespread used modal wavefront sensors is the bias beam based modal wavefront sensor which is based on estimating the strength of an aberration mode by measuring the difference in the central focal intensities of two bias beams. The two bias beams are two copies of the same incident beam with the addition of a certain aberration to the phase profile in the case of one and the subtraction of the same aberration from the phase profile in the case of the other. The bias beam based modal wavefront sensor provides direct measurement of the aberration mode strengths and has found applications in diverse areas. However, the output of the basic modal wavefront sensor has a limited range of linear response and the output gets effected by inter-modal cross talk. Holographic version of the modal wavefront sensor is easily implementable using a liquid crystal spatial light modulator (LCSLM). However, beams diffracted by the LCSLM is observed to be susceptible to temperature dependant wandering which degrades the performance of the sensor. In this thesis the issue of beam wandering associated with an LCSLM is first investigated and a means to minimize such beam movement is proposed. We then implement an LCSLM based modal wavefront sensor that has improved

beam stability. We then investigate the issue of inter-modal cross talk by developing a theoretical expression for quick quantitative estimation of the cross talk and results are verified experimentally. We then introduce a multiplex hologram based modal wavefront sensor that facilitates measurement of multiple aberrations with an enhanced linear response range and immunity from inter-modal cross talk. The proposed sensing scheme can perform without effecting the sensitivity and the sensing speed. The thesis ends with an application of our proposed wavefront sensor in free space line of sight optical communication system.

# Acronyms

| | | |
|---|---|---|
| BS | - | Beam Splitter |
| CCD | - | Charged Coupled Device |
| CGH | - | Computer Generated Holography |
| CMOS | - | Complementary Metal Oxide Semiconductor |
| DMD | - | Digital Micromirror Device |
| DPSS | - | Diod-Pumped Solid State Laser |
| FLCSLM | - | Ferroelectric Liquid Crystal Spatial Light Modulator |
| FSOC | - | Free Space Optical Communication |
| HMWS | - | Holographic Modal Wavefront Sensor |
| ID | - | Iris Diaphragm |
| LC | - | Liquid Crystal |
| LCSLM | - | Liquid Crystal Spatial Light Modulator |
| NDF | - | Neutral Density Filter |
| NLCSLM | - | Nematic Liquid Crystal Spatial Light Modulator |
| OAM | - | Orbital Angular Momentum |
| PC | - | Personal Computer |
| RF | - | Radio Frequency |
| RHS | - | Right Hand Side |
| SLM | - | Spatial Light Modulator |

# Contents

# List of Figures

# List of Tables

# Chapter 1

# General Introduction

## 1.1 Introduction

The surface formed by the loci of all the points of a light beam that are in the same phase or the points at equal optical path length from the source, is known as the wavefront of the light beam. A coherent light beam, such as a laser beam, when propagates through a transparent medium or reflects from a surface undergoes a change in the shape of the wavefront according to the characteristic of the transmitting medium or the reflecting surface. This change in the shape of the wavefront or deviation from an ideal wavefront can be termed as aberration introduced by the transmitting medium or the reflecting surface. The aberration thus introduced in the incident beam may lead to loss of information carried by the incident beam. It is possible to retrieve the information by knowing the strength of aberrations introduced during its propagation. If the incident beam has a plane wavefront then the aberrations introduced can be estimated from a measure of the wavefront of the transmitted or reflected beam. The wavefront corresponding to the transmitted or the reflected beam in such case may also provide information regarding the nature of the transmitting medium or the reflecting surface. The technique to measure the shape of the wavefront is known as wavefront sensing and the devices that perform wavefront sensing are known as wavefront sensors. The wavefront sensors find applications in diverse areas such as in the field of astronomy [1, 2], in optical shop testing [3, 4], in imaging biological tissues [5, 6], in high resolution optical microscopes [7, 8], in the correction of vision [9, 10], in high density data storage devices [11], in fluid dynamics [12], in free space optical communication [13, 14, 15],

etc. One can express the wavefront in terms of the constituent aberration modes. Thus an effective measurement of the wavefront or the aberrations present, can be carried out by measuring these constituent aberration modes. Though there are different approaches of representing the aberrations such as power series representation [16], Fourier series representation [17], Zernike polynomial representation [18], Walsh function representation [19] and so on, the Zernike polynomial representation is the most convenient approach and the same are used extensively.

The most widely used commercial wavefront sensor is the Shack-Hartmann wavefront sensor that came up in the 1970s out of the effort of Roland Shack and Ben Platt [20]. Apart from the Shack-Hartmann wavefront sensor other wavefront sensing techniques include the interferometric approach [21, 22], curvature sensing [23], pyramid sensing [24], bias beam based modal wavefront sensing [25], hybrid curvature and gradient wavefront sensing [26], etc. The commonly used wavefront sensors are broadly classified as zonal wavefront sensors and modal wavefront sensors. The zonal wavefront sensors divide the test wavefront into a number of sub-apertures or zones and the slope of each zone is measured individually. The combined slope information of all the zones is used to reconstruct the test wavefront. One can calculate the amount of aberrations present in the beam using a suitable algorithm [27, 28]. The Shack-Hartmann wavefront sensor and pyramid sensor fall under the category of zonal wavefront sensor. On the other hand, a modal wavefront sensor considers the wavefront to be a linear combination of a set of orthogonal aberration modes (say Zernike polynomials) whose coefficients give a measure of the amplitude of the respective aberration modes. A modal wavefront sensor measures the strength of each of the constituent aberration modes individually. The curvature sensor and the bias beam based modal wavefront sensor fall under this category. Thus the zonal wavefront sensors follow an indirect approach [27, 28] whereas the modal wavefront sensors follow a direct approach [25, 29] to estimate the various aberration modes present in the incident beam. The present work deals with the issues and limitations of the modal wavefront sensors.

Though the curvature sensor proposed by Roddier can be considered as the precursor to the modal wavefront sensor, the development of the generalized version of the curvature sensor (termed as bias beam based modal wavefront sensor or modal wavefront sensor) by Neil in 2000 [25] led to the effective implementation of the modal wavefront sensor. Neil's modal wavefront sensor works first by dividing the

incident beam into two beams with identical wavefronts as the incident beam and equal intensity which then pass through two bias plates. One of the bias plates adds a fixed amount of an orthogonal aberration mode to one of the beams (resulting in the positive bias beam) while the other bias plate subtracts the same amount of the aberration mode from the other beam (resulting in the negative bias beam). The presence of the given aberration mode in the incident beam will raise the focal intensity of one of the beams and lower the focal intensity of the other. This creates a difference in central intensities between the two focused beams. The difference in central intensities of the two focal spots gives a direct measure of the strength of the particular aberration mode present in the incident beam. One can measure the strengths of all other aberration modes present in the incident beam in a similar way. The scheme being simple and easily implementable has wide range of applications such as in close loop aberration correction [30], confocal microscopy [31], ophthalmology [32], free space optical communication [14], etc. There are also reports on modal wavefront sensor being used in high-contrast imaging [33] and precise positioning of a light emitter [34].

The accuracy of measurement of a given aberration mode is often affected if the beam contains an additional aberration mode. This phenomenon is called inter-modal cross talk and is considered as an intrinsic issue of a modal wavefront sensor. There are reports on the observation of inter-modal cross talk in modal wavefront sensors [34, 35, 36, 37, 38] and how it effects the sensor output. It is noticed that the influence of the presence of different additional aberration modes on the detection of a certain aberration mode is not same and varies for different aberration modes. However, a detailed analysis of this phenomenon is yet to be carried out. Therefore a comprehensive analysis on the issue of inter-modal cross talk is important in order to assess the limitations of the modal wavefront sensor.

Two other important parameters of a modal wavefront sensor are linear response range of the sensor (linearity of sensor output versus strength of the aberration present) and the capability of the sensor to detect a very small change in strength of the aberration present in the incident beam (called the sensitivity of the sensor). It is observed that a modal wavefront sensor shows a linear response over a very small range, i.e. for small magnitudes of the aberration mode. Though efforts were put to increase the range of linear response by varying the amount of the deliberately added aberration (termed as bias aberration) [29] or changing the size of the detector aperture [38], however, they come at the expense of the sensitivity

of the sensor. The modal wavefront sensor can be operated in an iterative feedback mode in conjunction with a phase correcting element to measure large amplitude of aberrations. However, iterative operation of the sensor increases the sensing time. Thus an alternative approach that leads to a larger range of linear response without compromising the sensitivity and speed of the sensor needs to be explored.

Implementation of the bias beam based modal wavefront sensor was made easier through the introduction of computer generated holograms (CGH) [25]. In the computer generated holography technique, interference patterns are calculated using a plane reference wavefront and a user defined object beam wavefront. The computed interference patterns can be used to fabricate a hologram which is then called CGH. The interference pattern can be binarized using an appropriate threshold condition in which case the hologram is called binary hologram. Such a binary hologram when placed in the path of an incident plane wave, gives rise to diffraction orders $(0, \pm1, \pm2, \pm3,,$ etc.). The propagation direction of the diffracted beam is decided by the fringe width in the hologram and the diffraction order. The zero order beam has the phase profile of the reference or the incident beam while the +1 and -1 order beams have the phase profiles of the object beam and the complex conjugate of the object beam, respectively. Thus if $\Phi$ is the phase profile of the beam incident on the hologram and $\Psi$ is the phase profile of the object beam constituting the hologram, the phase profile of the $+1$ order beam takes the form $\Phi + \Psi$ and that of the $-1$ order beam takes the form $\Phi - \Psi$. Therefore if $\Psi$ represents the bias aberration, the $+1$ and $-1$ order beams can act as the positive and the negative bias beams of a modal wavefront sensor, respectively, for the corresponding aberration mode.

The binary holograms are easily implementable with the help of Optical Modulators (OM) such as liquid crystal spatial light modulators (LCSLM) [39]. An LCSLM is a device that comprises a two dimensional array of liquid crystal pixels. The light transmittance of each liquid crystal pixel can be controlled via a computer interface. Thus it is possible to implement a modal wavefront sensor using the diffracted light from a binary hologram displayed on an LCSLM.

Though the LCSLMs enable easy implementation of the modal wavefront sensor, they have an inherent issue of molecular realignment due to the temperature dependence of the liquid crystal molecules constituting the LCSLM pixels. This may cause the beam diffracted from the LCSLM to digress with time from its ideal direction. A modal wavefront sensor measures the intensities at the centers of the bias beams. So, it is essential that the focal spot remains steady at a specific position while the

measurement is in progress. The unwanted deflection of the diffracted beam coming from the LCSLM will lead to the wrong measurements. Therefore the issue of the beam movement is important and requires an extensive study to come up with an effective means to reduce the amount of beam wandering.

In this thesis we address the above stated issues inherent to the basic modal wavefront sensors and issues arising during LCSLM based implementation of the modal wavefront sensor. We first investigate the orientational stability of the beams diffracted by an LCLSM to understand the root cause behind the unwanted beam movements. We also come up with a means to minimize the temperature dependent beam movements. We then develop a binary hologram based modal wavefront sensor using an LCSLM that has reduced beam fluctuations. We also perform a detailed analysis of the inter-modal cross talk present in the modal wavefront sensor and develop expressions to quantify the effect for various aberration modes in a less computationally intensive manner. The correctness of the theoretical expressions are assessed experimentally using the binary hologram based modal wavefront sensor. We then introduce a multiplex hologram based modal wavefront sensing scheme that has a much larger linear response range and superior cross talk immunity. The two inherent issues of the modal wavefront sensor are addressed without compromising the sensing speed and sensitivity of the sensor. We develop the necessary theory and implement an experimental setup to demonstrate the advantages of the proposed sensing scheme. Our sensing scheme can detect the presence of multiple aberration modes simultaneously from just one focal spot pattern. We then employ our proposed multiplex hologram based sensor to implement a free space line of sight optical communication system.

Below we provide a chapter wise overview of the present thesis.

**Chapter 2**: In this chapter, we provide a detail discussion on the wavefront aberration, their representations and wavefront sensors. We start with the description of the wavefront aberration using the scalar diffraction theory and then discuss about its representation using a set of orthogonal polynomials i.e. the Zernike polynomials. The later part of the chapter includes wavefront sensing and wavefront sensors where we discuss the basic principle of the zonal wavefront sensor and the modal wavefront sensor. Since the present research work is based on the modal wavefront sensor proposed by Neil, the working principle and the theoretical considerations of this particular sensor are presented in greater details. We then focus on the limitations and the issues associated with the modal wavefront sensors.

**Chapter 3**: This chapter begins with a brief introduction to classical and computer generated holography and how a user defined wavefront can be constructed using the computer generated holography. It then explains how the bias beam based modal wavefront sensor can be implemented using the computer generated holography technique in which case it is called holographic modal wavefront sensing. The chapter describes two holographic modal wavefront sensing schemes to measure multiple aberration modes, namely the sequential and the simultaneous measurement schemes. Simulation results to validate the principle of the holographic modal wavefront sensor are presented towards the end of the chapter.

**Chapter 4**: In this chapter, we describe the experimental implementation of the holographic modal wavefront sensor. We first provide brief introductions to the important devices used during the experimental implementation of the sensor. We implement the modal wavefront sensor using an LCSLM, hence we also investigate an issue arising out of the temperature dependence of the liquid crystal molecules constituting the LCSLMs leading to unwanted beam movements. Such unwanted deflection of the diffracted beams may lead to the wrong measurements. We present here a way to minimize these unwanted beam movements. The chapter ends with experimental results to show the working the holographic modal wavefront sensor using a proof of principle setup.

**Chapter 5**: In this chapter, we address the issue of the presence of the inter-modal cross talk in a modal wavefront sensor. We first provide a detail theoretical analysis and come with an expression that facilitates quick computation to quantify the effect of inter-modal cross talk. We verify the results of our expression with analytical results and experimental results. We also employ our expressions to get an in-depth view of the issue of inter-modal cross talk.

**Chapter 6**: In this chapter, we introduce a multiplex hologram based modal wavefront sensor which we name as the type-K modal wavefront sensor. We first develop theory of the proposed sensor to show that the proposed wavefront sensor provides superior linear response and immunity from inter-modal cross talk relative to the basic modal wavefront sensor. The improvements are achieved without compromising on the sensitivity and speed of the sensor. We also propose multiplex hologram design scheme that enables measurement of multiple aberration modes present in the incident beam from just one camera image. The advantages of the proposed sensing scheme is demonstrated through numerical simulation and experiment.

**Chapter 7**: In this chapter, we present an application of the proposed type-K modal wavefront sensor in free space optical communication. We show how information can be encoded using multiple Zernike modes, deliberately incorporated into a laser beam which propagates through certain free space. The receiver station uses a type-K modal wavefront sensor to decode the information present in the wavefront. We present experimental results showing successful transmission of text data and image data using our proof of principle setup.

**Chapter 8**: In this chapter we provide a brief summary of the important findings of the research work along with the future prospects.

## 1.2 Conclusion

This chapter provides a general introduction to the primary objective of the research followed by a chapter wise overview of the thesis. The chapter begins with a brief discussion on the wavefront and wavefront sensors. The chapter also includes a brief discussion on the principle of an important wavefront sensor, the modal wavefront sensor, and the various issues and limitations associated with it. It then discusses how some of important issues associated with the modal wavefront sensor are addressed in the thesis. The chapter ends with a chapter wise overview of the present thesis.

# Chapter 2

# Introduction to Wavefront Aberration and Wavefront Sensing

## 2.1 Introduction

This chapter discusses the wavefront aberration and wavefront sensing. Our focus will be mainly on the monochromatic wave aberrations and their representations. The later part of the chapter involves discussion on the wavefront sensing and wavefront sensors. These include the basic principle of two broad categories of wavefront sensors: the zonal wavefront sensors and the modal wavefront sensors. As the primary objective of the current thesis is based on the modal wavefront sensor, the chapter provides a detail discussion on the theory behind the modal wavefront sensor. The chapter also provides a discussion on the various issues and limitations of the modal wavefront sensor.

## 2.2 Wavefront aberration

Wavefront aberration can be considered as the deviation in the shape of the wavefront from that of the ideal wavefront or the deviation of the optical path traveled from that of the ideal path. The basic aberrations are of two types, namely, the chromatic aberrations and the monochromatic aberrations. The chromatic aberrations are the aberrations that arise when waves with different frequencies or wavelengths (colors) refract at different angles as they pass through the traversing medium which then converge to different focal planes. This is due to the frequency or wavelength

dependence of the refractive index of the traversing medium, resulting in an image of an object with colored fringes at its sharp edges. On the other hand the monochromatic aberrations arise even when the image is formed with monochromatic (single color) light waves. Since all our experimental work in this thesis include the use of monochromatic light from a laser source, we will restrict our discussion to the monochromatic aberrations only. Further, experimental setups presented here to study the aberrations are designed to satisfy the paraxial approximation and hence we will use the scalar diffraction theory to understand the different aspect of aberrations.

### 2.2.1 Monochromatic aberration using scaler diffraction theory

Let us start with the integral expression of the diffraction theory to represent the aberration. Let $P_o$ be a point source of monochromatic light positioned at a height $h$ from the axis (optical axis) of an optical system and $W$ be the wavefront located at $O$, the center of the exit pupil of the optical system (shown in Fig. 2.1 (i)). The wavefront of an aberration free optical system, will coincide with a sphere $G$ with its center of curvature at the Gaussian image point $P_o'$ formed at a height $h'$ with respect to the optical axis. The sphere $G$ is known as the Gaussian reference sphere. Let us also consider that a ray from $Q'$ to an arbitrary point $P'$ in the image space intersect the wavefront $W$ and the Gaussian reference sphere $G$ at $Q'$ and $Q$, respectively. The optical path length $Q'Q$ or the corresponding phase $\Phi = \frac{2\pi}{\lambda}Q'Q$ is the aberration of the wave element at $Q$ in the length unit or in radian, respectively. The wavefront aberration is positive if $Q'$ and $P'$ lies on the opposite side of $Q$ otherwise the wavefront aberration is negative. If $R$ and $s$ denotes the radius of the Gaussian reference sphere $OP_o'$ and the length $QP'$, respectively, the disturbance at $P'$ according to Huygens-Fresnel principle can be written as [16],

$$E(P') = -\frac{iCexp\,[-ikR]}{\lambda R}\int\int\frac{exp\,[-ik(\Phi+s)]}{s}dw \tag{2.1}$$

The integration of Eq. 2.1 is extended over the whole exit pupil and $dw$ is an infinitesimal surface element of the wavefront. $C$ is a constant over the whole wavefront and the angles subtended are assumed to be very small. Let $l$ be the radius of the exit pupil and, $(x, y, z)$ and $(\epsilon, \eta, \zeta)$ be the Cartesian coordinates of $Q$ and $P'$

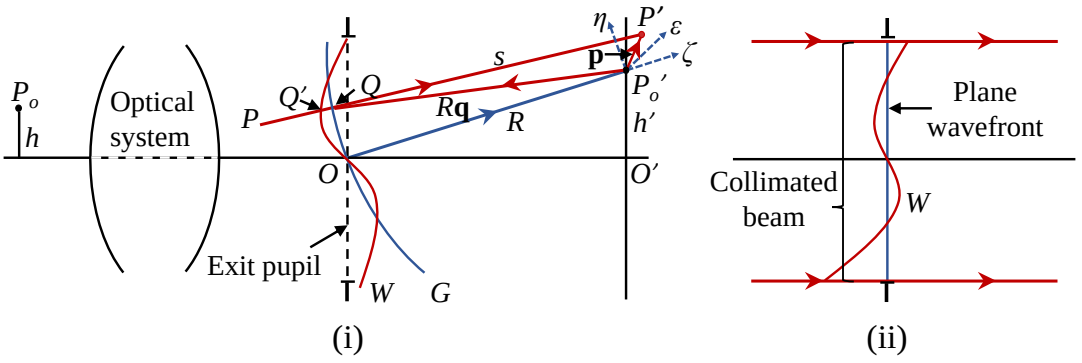


**Figure 2.1:** Representation of wavefront aberration (i) in terms of Gaussian reference sphere, and (ii) in terms of deviation from a plane wavefront for a collimated beam.

with their polar coordinates as $(r, \theta)$ and $(\rho, \alpha)$, respectively. Let the $\eta$ axis be in the plane containing $P_o$ and the optical axis of the system and $\zeta$ axis is along $OP'_o$. Then for an aberration free case one can write

$$\begin{aligned} x = lrsin\theta,\ y = lrcos\theta, \\ \epsilon = \rho sin\psi,\ \eta = \rho cos\psi \end{aligned} \tag{2.2}$$

and for a spherical wavefront $(R^2 = x^2 + y^2 + z^2)$

$$z = -\sqrt{R^2 - l^2r^2} = R\left[1 - \frac{l^2r^2}{2R^2} + ...\right] \tag{2.3}$$

If $\mathbf{q}$ is a unit vector in the direction $P'_oQ$ and $\mathbf{p} = \mathbf{P'_oP'}$, then

$$\mathbf{q}.\mathbf{p} = -(s - R) = \frac{\epsilon x + \eta y + \zeta z}{R} \tag{2.4}$$

Now, substituting the parameters from Eq. 2.2 in Eq. 2.4 and keeping only upto second order term of $\zeta$, we get

$$k(s - R) = -vrcos(\theta - \alpha) - \frac{1}{2}ur^2 + \left(\frac{R}{l}\right)^2 u \tag{2.5}$$

where, $u$ and $v$ are the two optical coordinates of $P'$ defined as,

$$u = \frac{2\pi}{\lambda}\left(\frac{l}{R}\right)^2 \zeta,\ v = \frac{2\pi}{\lambda}\left(\frac{l}{R}\right)\sqrt{\epsilon^2 + \eta^2} \tag{2.6}$$

Now using Eq. 2.5 and $dw = l^2 r dr d\theta$, Eq. 2.1 can be rewritten as,

$$\begin{aligned} E(P') &= E(u,v,\theta) = -\frac{iCl^2}{\lambda R^2} exp\left[i\left(\frac{R}{l}\right)^2 u\right] \\ &\times \int_0^1 \int_0^{2\pi} exp\left[i\left(k\Phi(h',r,\theta) - vrcos(\theta-\alpha) - \frac{1}{2}ur^2\right)\right] r dr d\theta \end{aligned} \tag{2.7}$$

And the intensity at $P'$ can be written as,

$$\begin{aligned} I(P') &= |E(P')|^2 = \left(\frac{Cl^2}{\lambda R^2}\right)^2 \\ &\times \left|\int_0^1 \int_0^{2\pi} exp\left[i\left(k\Phi(h',r,\theta) - vrcos(\theta-\alpha) - \frac{1}{2}ur^2\right)\right] r dr d\theta\right|^2 \end{aligned} \tag{2.8}$$

The expression for intensity can be normalized by the intensity at the Gaussian image point $P'$ obtained under the aberration free condition, i.e. $I_o(P') = \pi^2 \left(\frac{Cl^2}{\lambda R^2}\right)^2$. Thus, the expression for the normalized intensity at the Gaussian image point $P'$ can be written as,

$$I_n(P') = \frac{I(P')}{I_o(P')} = \frac{1}{\pi^2}\left|\int_0^1 \int_0^{2\pi} exp\left[i\left(k\Phi(h',r,\theta) - vrcos(\theta-\alpha) - \frac{1}{2}ur^2\right)\right] r dr d\theta\right|^2 \tag{2.9}$$

Therefore, the presence of aberration reduces the intensity at the Gaussian image point which has the maximum intensity in the aberration free case. $I_n(P'_o)$ of Eq. 2.9 can also be called the Strehl ratio which can be defined as the ratio of the central intensity of the image of a point object in the presence of aberration to that without aberration and is a measure of the image quality of an optical system. Eq. 2.9 provides a relation between the normalized intensity at a Gaussian image point and the wave aberration at the exit pupil of an optical system. If we consider the point $P'$ to lie on the $\epsilon\eta$-plane containing the point $O'$ (center of the Gaussian reference sphere) i.e. $\zeta = 0$, then Eq. 2.9 takes the form

$$\begin{aligned} I_n(P') &= \frac{1}{\pi^2}\left|\int_0^1 \int_0^{2\pi} exp\left[i\left(k\Phi(h',r,\theta) - vrcos(\theta-\alpha)\right)\right] r dr d\theta\right|^2 \\ &= \frac{1}{\pi^2}\left|\mathscr{F}\left(exp\left[ik\Phi(h',r,\theta)\right]\right)\right|^2 \end{aligned} \tag{2.10}$$

where, $\mathscr{F}\left(exp\left[ik\Phi(h',r,\theta)\right]\right)$ is the Fourier transform of the function $exp\left[ik\Phi(h',r,\theta)\right]$ [40]. The $\epsilon\eta$-plane can be called the Fourier plane.

From Fig. 2.1 (i) it is clear that the coordinate of the center of the Gaussian reference sphere $P'_o$ is $(0,0,0)$ i.e. $\epsilon = 0$, $\eta = 0$ and $\zeta = 0$. Thus, the normalized intensity at the center of the Gaussian reference sphere or at the focal point of a lens representing the optical system, $P'_o$ is

$$\begin{aligned} I_n(P'_o) &= \frac{1}{\pi^2}\left|\int_0^1\int_0^{2\pi} exp\left[ik\Phi\right] r dr d\theta\right|^2 \\ &= \frac{1}{\pi^2}\left|\int_0^1\int_0^{2\pi} [1 + ik\Phi + \frac{1}{2}(ik\Phi)^2 + ... + \frac{1}{n}(ik\Phi)^n + ...] r dr d\theta\right|^2 \end{aligned} \quad (2.11)$$

The exponential term, $exp\left[ik\Phi\right]$, on the RHS (right hand side) of Eq. 2.11 is expanded using Taylor series expansion. The average value of $\Phi^n$ can be written as

$$\overline{\Phi^n} = \frac{\int_0^1\int_0^{2\pi}\Phi^n r dr d\theta}{\int_0^1\int_0^{2\pi} r dr d\theta} = \frac{1}{\pi}\int_0^1\int_0^{2\pi}\Phi^n r dr d\theta \quad (2.12)$$

Now, for small aberration ($\Phi$ is small) the terms with third and higher power of $\Phi$ can be neglected. So, Eq. 2.11 becomes

$$I_n(P'_o) \approx \left|1 + ik\overline{\Phi} - \frac{1}{2}k^2\overline{\Phi^2}\right|^2 = 1 - \left(\frac{2\pi}{\lambda}\right)^2\left[\overline{\Phi^2} - \left(\overline{\Phi}\right)^2\right] \quad (2.13)$$

Here the quantity $\overline{\Phi^2} - \left(\overline{\Phi}\right)^2 = (\Delta\Phi)^2$ is the mean square wavefront error or the variance of the wave aberration. Therefore Eq. 2.13 can now be simplified to

$$I_n(P'_o) \approx 1 - \left(\frac{2\pi}{\lambda}\right)^2 (\Delta\Phi)^2 \approx \quad Strehl \quad ratio \quad (2.14)$$

From Eq. 2.14 it is clear that the normalized intensity for small aberration measured at the center of the Gaussian reference sphere does not depends on the nature of the aberration and is less than the ideal value by $\left(\frac{2\pi}{\lambda}\right)^2$ times the mean square wavefront error. Using Eq. 2.14, we can also express the root mean square (RMS) wavefront error, $\Phi_{RMS}$ in terms of the normalized intensity at the center of the Gaussian reference sphere, such that

$$\Phi_{RMS} = \Delta\Phi \approx \frac{\lambda}{2\pi}\left[1 - I_n(P'_o)\right]^{\frac{1}{2}} \quad (2.15)$$

Thus, $\Phi_{RMS}$ which gives a quantitative measure of the wavefront aberration can be estimated from the normalized intensity or the Strehl ratio at the center of the

Gaussian reference sphere or at the focal point of a lens representing the optical system. The above definitions of $\Phi$ and $\Phi_{RMS}$ also hold when we consider a collimated beam instead of a convergent beam as in Fig. 2.1 (i). In Fig. 2.1 (ii) we see a collimated beam equivalent to the convergent beam. The wavefront aberration $\Phi$ is now defined as the deviation of the aberrated wavefront from a plane wavefront. The focal point of such a collimated beam when focused by a lens now corresponds to the Gaussian image point $P'_o$.

### 2.2.2 Representation of wavefront aberration

The aberration function of an optical system with a circulat pupil can be expanded in terms of a power series or a complete set of orthogonal functions. The optical imaging systems on the other hand normally have an axis of rotational symmetry. Thus the aberration function of the optical imaging systems can be expanded as a power series of three rotational invariants $h^2$, $r^2$ and $hrcos(\theta)$, considering the point object to lie along the $x$ axis [41] as,

$$\begin{aligned}\Phi(h';r,\theta) &= \sum_{p=0}^{\infty}\sum_{q=0}^{\infty}\sum_{m=0}^{\infty} C_{pqm}\left(h'^2\right)^p\left(r^2\right)^q(hrcos\theta)^m \\ &= \sum_{p=0}^{\infty}\sum_{n=1}^{\infty}\sum_{m=0}^{n} {}_{(2p+m)}a_{nm}h'^{(2p+m)}r^n cos^m\theta \end{aligned} \tag{2.16}$$

where $p$, $q$ and $m$ are whole numbers, $C_{pqm}$ and ${}_{(2p+m)}a_{nm}$ are expansion coefficients and $n = 2q + m$ ($n - m \geq 0$ and even). If we combine all the terms with different dependencies on the object plane coordinates but with the same dependencies on the image plane coordinates, we can reduce the terms of the power series expansion to one term par $(n, m)$ pair. Thus Eq. 2.16 can be reduced to

$$\Phi(r,\theta) = \sum_{n=1}^{\infty}\sum_{m=0}^{n} a_{nm}r^n cos^m\theta \tag{2.17}$$

where $a_{nm} = \sum_{p=0}^{\infty} {}_{(2p+m)}a_{nm}h'^{(2p+m)}$ is the expansion coefficient term representing the peak value of the respective aberration term and the various terms represent the classical aberrations. A parameter $e = 2p + n + m$ can be defined to represent the degree of the different terms of the power series expansion. All the terms with $e = 4$ represent the primary aberrations (Seidel aberrations) while the terms with $e = 6$

**Table 2.1:** Primary aberrations and their variance.

| **Aberration** | $\mathbf{\Phi(r,\theta)}$ | $\mathbf{(\Delta\Phi)^2}$ | $\mathbf{\Phi_B(r,\theta)}$ | $\mathbf{(\Delta\Phi_B)^2}$ |
|---|---|---|---|---|
| Spherical | $a_{40}r^4$ | $2a_{40}/3\sqrt{5}$ | $a_{40}(r^4+r^2)$ | $a_{40}/6\sqrt{5}$ |
| Coma | $a_{31}r^3cos\theta$ | $a_{31}/2\sqrt{2}$ | $a_{31}(r^3-\frac{2}{3}r)cos\theta$ | $a_{31}/6\sqrt{2}$ |
| Astigmatism | $a_{22}r^2cos^2\theta$ | $a_{22}/4$ | $a_{22}r^2(cos^2\theta-\frac{1}{2})$ | $a_{22}/2\sqrt{6}$ |
| Field curvature | $a_{20}r^2$ | $a_{20}/2\sqrt{3}$ | $a_{20}r^2$ | $a_{20}/2\sqrt{3}$ |
| Distortion | $a_{11}rcos\theta$ | $a_{11}/2$ | $a_{11}rcos\theta$ | $a_{11}/2$ |

represent the secondary aberrations (Schwarzschild aberrations). On expanding Eqs. 2.16 and 2.17 to obtain all the terms with $e = 4$ we get

$$\begin{aligned} \Phi(h';r,\theta) &= {}_0a_{40}r^4 + {}_1a_{31}h'r^3cos\theta + {}_2a_{22}h'^2r^2cos^2\theta + {}_2a_{20}h'^2r^2 \qquad (2.18)\\ &+ {}_3a_{11}h'^3rcos\theta \\ \Phi(r,\theta) &= a_{40}r^4 + a_{31}r^3cos\theta + a_{22}r^2cos^2\theta + a_{20}r^2 + a_{11}rcos\theta \qquad (2.19) \end{aligned}$$

Equations 2.18 and 2.19 show the representation of the aberration function $\Phi(h';r,\theta)$ and $\Phi(r,\theta)$, respectively, in terms of the primary or the Seidel aberrations namely spherical aberration, coma, astigmatism, field curvature and distortion (starting from the first term). From Eq. 2.14 it is seen that in order to have a maximum Strehl ratio, the variance should be minimum. The variance of a particular aberration on the other hand can be reduced by combining it with certain lower order aberrations, i.e. with lower $n+m$ values. The variance of spherical aberration can be reduced by four times when combined with equal and opposite amount of field curvature (or defocus). Similarly coma and astigmatism are combined with distortion (or wavefront tilt) and field curvature, respectively, to reduce their respective variance. This technique of reducing the variance of the aberrations by combining them with lower order aberrations is known as aberration balancing and the aberrations so obtained are known as balanced aberrations. Table 2.1 shows the expression and the variance ($\Phi(r,\theta)$ and $(\Delta\Phi)^2$) before balancing and ($\Phi_B(r,\theta)$ and $(\Delta\Phi_B)^2$) after balancing of the five primary aberrations. The variance $(\Delta\Phi)^2$ can be obtained using the expression $\overline{\Phi^2} - \left(\overline{\Phi}\right)^2 = (\Delta\Phi)^2$ where $\overline{\Phi^2}$ is defined in Eq. 2.12.

Apart from the power series expansion, the wavefront aberration can also be represented in terms of a set of orthogonal polynomials. The most convenient and

the most commonly used such polynomials are the Zernike polynomials [16]. This set of polynomials were first derived by Fritz Zernike in 1934 for determining the error of a mirror surface in his phase contrast method [42]. The Zernike polynomials defined over a circular aperture, known as the Zernike circle polynomials, form a complete set and are orthogonal over a unit circle.

Though there are several indexing scheme of the Zernike circle polynomials, in the present work we follow the Noll's convention [18] of single index Zernike mode representation. The Zernike mode using Noll's convention can be written in polar coordinate as,

$$\left.\begin{aligned} Z_{even\,j}(r,\theta) &= \sqrt{n+1}R_n^m(r)\sqrt{2}\cos(m\theta) \\ Z_{odd\,j}(r,\theta) &= \sqrt{n+1}R_n^m(r)\sqrt{2}\sin(m\theta) \end{aligned}\right\} \text{for } m \neq 0$$
$$Z_j(r,\theta) = \sqrt{n+1}R_n^m(r) \qquad \text{for } m = 0 \tag{2.20}$$

where, $n$ and $m$ are radial degree and azimuthal frequency, respectively, such that they are positive integers including zero, $m \leq n$ and $n - m = even$. $j$ is the order or the index of the Zernike modes and the function $R_n^m(r)$ is expressed as,

$$R_n^m(r) = \sum_{g=0}^{\frac{(n-m)}{2}} \frac{(-1)^g (n-g)!}{g!\left[\frac{n+m}{2}-g\right]!\left[\frac{n-m}{2}-g\right]!} r^{n-2g} \tag{2.21}$$

Thus, the aberration function $\Phi(r,\theta)$ for an incident wavefront can be written as a linear combination of various Zernike circle polynomials $Z_j(r,\theta)$ [43][16] so that

$$\Phi(r,\theta) = \sum_{j=1}^{\infty} a_j Z_j(r,\theta) \tag{2.22}$$

where $a_j$ is the expansion coefficient or the aberration coefficient.

Table 2.2 shows the first few Zernike modes both in Polar and Cartesian coordinates, with the common aberration that each mode represents. The first Zernike mode i.e. $Z_1$ represents the piston and has no effect on the shape of the wavefront or the image. It only gives a constant shift to the wavefront along the direction of propagation (i.e. $z$ direction). The next two modes i.e. $Z_2$ and $Z_3$ represent a tilt to the incident wavefront in the $x$ and $y$ directions, respectively. The fourth term $Z_4$ (defocus) basically represents a focusing error and can be eliminated by shifting the focal plane along the axis of the system. Thus the first four Zernike modes are

**Table 2.2:** Noll's convention of single index Zernike mode representation.

| j | n | m | $Z_j(r,\theta)$(Polar coordinates) | $Z_j(x,y)$(Cartesian coordinates) | Common aberration |
|---|---|---|---|---|---|
| 1 | 0 | 0 | $1$ | $1$ | Piston |
| 2 | 1 | 1 | $2rcos\theta$ | $2x$ | x tilt |
| 3 | 1 | 1 | $2rsin\theta$ | $2y$ | y tilt |
| 4 | 2 | 0 | $\sqrt{3}(2r^2-1)$ | $\sqrt{3}(2(x^2+y^2)-1)$ | Defocus |
| 5 | 2 | 2 | $\sqrt{6}r^2sin2\theta$ | $2\sqrt{6}xy$ | Primary astigmatism at $\pm$ 45° |
| 6 | 2 | 2 | $\sqrt{6}r^2cos2\theta$ | $\sqrt{6}(x^2-y^2)$ | Primary astigmatism at 0° |
| 7 | 3 | 1 | $\sqrt{8}(3r^2-2r)sin\theta$ | $\sqrt{8}(3(x^2+y^2)-2)y$ | Primary y coma |
| 8 | 3 | 1 | $\sqrt{8}(3r^2-2r)cos\theta$ | $\sqrt{8}(3(x^2+y^2)-2)x$ | Primary x coma |
| 9 | 3 | 3 | $\sqrt{8}r^3sin3\theta$ | $\sqrt{8}(3x^2y-y^3)$ | Trefoil y |
| 10 | 3 | 3 | $\sqrt{8}r^3cos3\theta$ | $\sqrt{8}(x^3-3y^2x)$ | Trefoil x |
| 11 | 4 | 0 | $\sqrt{5}(6r^4-6r^2+1)$ | $\sqrt{5}(6(x^2+y^2)^2-6(x^2+y^2)+1)$ | Primary spherical aberration |
| 12 | 4 | 2 | $\sqrt{10}(4r^4-3r^2)cos2\theta$ | $\sqrt{10}(4(x^2+y^2)-3)2xy$ | Secondary astigmatism at 0° |
| 13 | 4 | 2 | $\sqrt{10}(4r^4-3r^2)sin2\theta$ | $\sqrt{10}(4(x^2+y^2)-3)(x^2-y^2)$ | Secondary astigmatism at $\pm$ 45° |
| 14 | 4 | 4 | $\sqrt{10}r^4cos4\theta$ | $\sqrt{10}(4(x^4+y^4)-6x^2y^2)$ | Tetrafoil x |
| 15 | 4 | 4 | $\sqrt{10}r^4sin4\theta$ | $\sqrt{10}(4xy(x^2-y^2))$ | Tetrafoil y |
| 16 | 5 | 1 | $\sqrt{12}(10r^5-12r^3+3r)cos\theta$ | $\sqrt{12}(10(x^2+y^2)^2-12(x^2+y^2)+3)x$ | Secondary x coma |
| 17 | 5 | 1 | $\sqrt{12}(10r^5-12r^3+3r)sin\theta$ | $\sqrt{12}(10(x^2+y^2)^2-12(x^2+y^2)+3)y$ | Secondary y coma |
| 18 | 5 | 3 | $\sqrt{12}(5r^5-4r^3)cos3\theta$ | $\sqrt{12}(10(x^2+y^2)-4)(x^3-3y^2x)$ | Secondary y trefoil |
| 19 | 5 | 3 | $\sqrt{12}(5r^5-4r^3)sin3\theta$ | $\sqrt{12}(5(x^2+y^2)-4)(3x^2y-y^3)$ | Secondary x trefoil |
| 20 | 5 | 5 | $\sqrt{12}r^5cos5\theta$ | $\sqrt{12}(5x(x^2+y^2)^2-4x^5-20y^2x^3)$ | Pentafoil x |
| 21 | 5 | 5 | $\sqrt{12}r^5sin5\theta$ | $\sqrt{12}(5y(x^2+y^2)^2-4y^5-20x^2y^3)$ | Pentafoil y |
| 22 | 6 | 0 | $\sqrt{7}(20r^6-30r^4+12r^2-1)$ | $\sqrt{7}(20(x^2+y^2)^3-30(x^2+y^2)^2+12(x^2+y^2)-1)$ | Secondary spherical aberration |

generally not considered as aberrations as they indicate only a shift or translation in the image plane. All the rest of the Zernike modes are considered as aberrations since they reduce the sharpness in even a correctly positioned image plane.

### Properties of the Zernike polynomials

**(A) Orthogonal over a unit circle**: The orthogonality of the radial ($R_n^m(r)$) and the angular ($cos(m\theta), sin(m\theta)$) functions are expressed as,

$$\begin{aligned} &\int_0^1 R_n^m(r)R_{n'}^m(r)rdr = \tfrac{1}{2(n+1)}\delta_{nn'}, \\ &\int_0^{2\pi} cos(m\theta)cos(m'\theta)d\theta = \pi(1+\delta_{m0})\delta_{mm'}, \\ &\int_0^{2\pi} sin(m\theta)sin(m'\theta)d\theta = \pi\delta_{mm'}, \\ &\int_0^{2\pi} cos(m\theta)sin(m'\theta)d\theta = 0 \end{aligned} \tag{2.23}$$

Thus the polynomials satisfy the condition of orthogonality, such that

$$\frac{\int_0^1\int_0^{2\pi} Z_j Z_{j'} r dr d\theta}{\int_0^1\int_0^{2\pi} r dr d\theta} = \delta_{jj'} \tag{2.24}$$

where, $\delta_{jj'}$ is a Kronecker delta function.

**(B) Zero mean over a unit circle**: The Zernike polynomials, except $Z_1$ (piston), have a zero mean over a unit circle, thus

$$\int_0^1\int_0^{2\pi} Z_j r dr d\theta = 0 \tag{2.25}$$

**(C) Rotationally invariant**: The Zernike polynomials are invariant against the rotation of the coordinate axes about the origin. This property enables the implementation of the Zernike polynomials for a rotationally symmetric system. Since an optical imaging system has an axis of rotational symmetry, the Zernike polynomials can be conveniently used to represent the aberration function of such a system.

**(D) Self balanced**: If we compare the representative aberrations of Tables 2.1 and 2.2, it is observed that the Zernike polynomial expressions represent balanced aberrations. Thus they are balanced in itself to minimize their variance, thereby increasing the Strehl ratio.

**(E) Expansion coefficient as root mean square value of the aberration function**: The mean $\overline{\Phi(r,\theta)}$ and the mean square $\overline{\Phi^2(r,\theta)}$ values of the aberration

function can be written as,

$$\overline{\Phi(r,\theta)} = \frac{\int_0^1 \int_0^{2\pi} \Phi r dr d\theta}{\int_0^1 \int_0^{2\pi} r dr d\theta} = a_1 \tag{2.26}$$

$$\overline{\Phi^2(r,\theta)} = \frac{\int_0^1 \int_0^{2\pi} \Phi^2 r dr d\theta}{\int_0^1 \int_0^{2\pi} r dr d\theta} = \sum_{j=1}^{\infty} a_j^2 \tag{2.27}$$

Thus the variance of the aberration function will be

$$[\Delta\Phi(r,\theta)]^2 = \left[\overline{\Phi(r,\theta)}\right]^2 - \overline{\Phi^2(r,\theta)} = \sum_{j=2}^{\infty} a_j^2 \tag{2.28}$$

Therefore, variance of the aberration function is equal to the summation of the squares of the expansion co-efficients barring that of piston ($Z_1$). Thus if the aberration function comprises just one Zernike term then the standard deviation of the aberration function $\Delta\Phi(r,\theta)$ and hence the RMS wavefront error $\Phi_{RMS}$ is the expansion co-efficient of the Zernike mode itself. In this thesis therefore we use the notation $\Phi_{RMS}$ to represent the amplitude or the co-efficient of the aberration modes since in the case of the Zernike modes the amplitude of the mode and the RMS error share the same value.

Though the Zernike polynomials are advantageous over other polynomials to represent wavefront aberrations in optical systems, they suffer from the limitation of being orthogonal only for a continuous variables over a unit circle and the orthogonality vanishes for discrete variables [44].

Now assuming the presence of phase aberrations only, the complex amplitude of the light beam at the entrance pupil of the optical system can be represented as,

$$E(r,\theta) = \exp[i\Phi(r,\theta)]P_f(r,\theta) = \exp\left[i\sum_{j=1}^{\infty} a_j Z_j(r,\theta)\right] P_f(r,\theta) \tag{2.29}$$

where, $P_f(r,\theta))$ is the pupil function of the entrance pupil of the focusing lens defined as,

$$P_f(r,\theta) = \begin{cases} 1, & \text{inside the pupil} \\ 0, & \text{outside the pupil} \end{cases} \tag{2.30}$$

Thus, the intensity distribution of the focused image at the image plane of the

optical system can be written as (similar to Eq. 2.10),

$$I(\rho,\alpha) = \frac{I_o}{\pi^2}\left|\int_0^1\int_0^{2\pi} P_f \exp\left[i\sum_{j=1}^{\infty} a_j Z_j\right] exp\left[i2\pi\rho rcos(\alpha-\theta)\right] r dr d\theta\right|^2 \qquad (2.31)$$

where $\rho$ and $\alpha$ are the radial and the azimuthal coordinates of the image plane and $I_o$ is a constant. Equation 2.31 can be used to calculate the image plane intensity distribution for a beam aberrated with different combination of Zernike modes. Three dimensional plots of the phase profile and the corresponding image plane intensity distributions for an aberration free wavefront (i.e. a plane wavefront) and for a beam in the presence of five different Zernike modes are shown in Fig. 2.2. Figures 2.2(i-a) and (i-b) show the phase plots and the intensity distribution at the

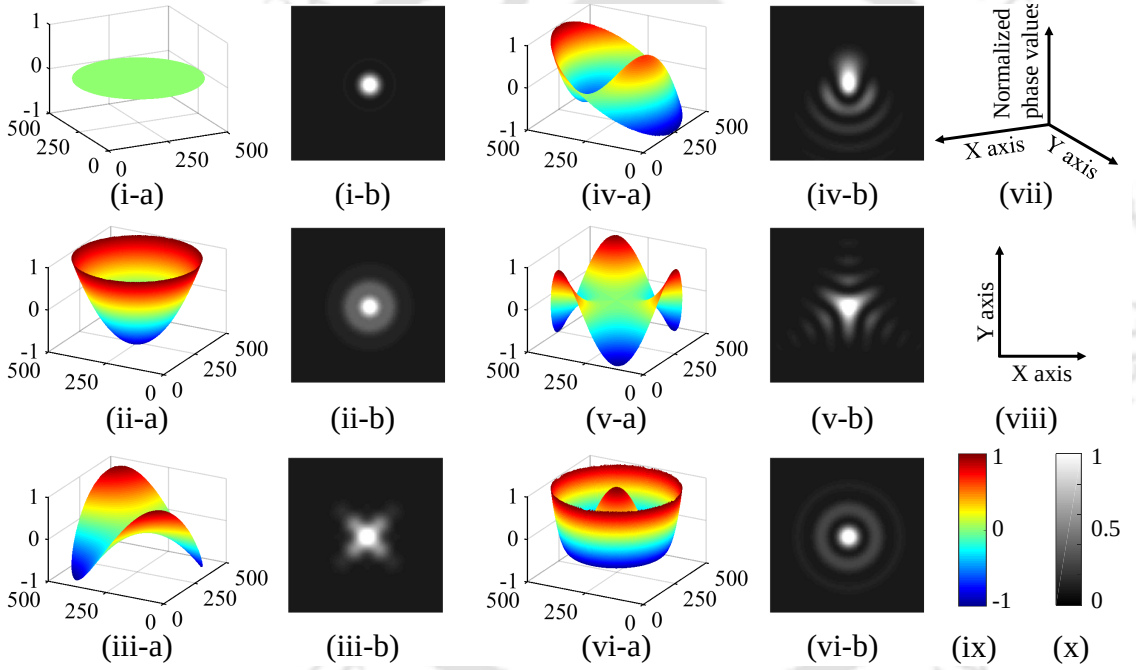


**Figure 2.2:** (a) The plot of the phase and (b) the image of the intensity distribution representing (i) aberration free case and in presence of (ii) defocus, (iii) astigmatism, (iv) coma, (v) trefoil and (vi) spherical aberrations. Representations of (vii) the axes of the phase plots, (viii) the axes of the intensity distribution images, (ix) the color bar of the phase plots and (x) the color bar of the intensity distribution images.

image plane of an unaberrated plane wavefront, whereas, Figs. 2.2(ii-a) and (ii-b) to Figs. 2.2(vi-a) and (vi-b) show the phase plots and the intensity distribution at the image plane when the wavefront comprises Zernike modes $Z_4$ (defocus), $Z_5$ (astigmatism), $Z_7$ (coma), $Z_9$ (trefoil) and $Z_{11}$ (spherical aberration), respectively. Further, Figs. 2.2(vii) and (viii) show the axes of the phase profile plots and the

intensity distribution images, respectively. Figures 2.2(ix) and (x) are the color bar representation of the phase profile plots and the intensity distribution images, respectively.

## 2.3 Wavefront sensing and wavefront sensors

Wavefront sensing is the technique of measuring the phase profile or the wavefront of the incident beam. The device used for wavefront sensing is known as wavefront sensor. However, none of the available wavefront sensing technique can give a direct measure of the wavefront, as all the available detectors are capable of measuring only the intensity of the incident light beam and not the phase. Thus, indirect approaches are developed where the phase information is obtained from the intensity information of the incident beam. As mentioned in chapter 1 the most commonly used wavefront sensing techniques are broadly classified into two groups, namely the zonal wavefront sensors (Shack-Hartmann wavefront sensor, pyramid sensor, etc.) and modal wavefront sensors (curvature sensor, bias beam based modal wavefront sensor, etc.). Below we discuss the basic principle of a zonal wavefront sensor, the Shack-Hartmann wavefront sensor, and two important modal wavefront sensors, the curvature sensor and bias beam based modal wavefront sensor. As the present research work deals with the issues and limitations of the bias beam based modal wavefront sensor, hence the principle and theory of this particular sensor are discussed in more details.

## 2.4 Zonal wavefront sensing

Zonal wavefront sensing is the technique where the wavefront is initially divided into a number of constituent zones or sub-apertures and the slope of each of the zones is measured individually. The slope information of all the zones are then combined to obtained the shape of the wavefront or the phase profile of the incident beam. Since the most popular zonal wavefront sensor is the Shack-Hartmann wavefront sensor, a brief discussion of its principle is given below.

### 2.4.1 Shack-Hartmann wavefront sensor

Shack-Hartmann wavefront sensor is the most widely used commercial wavefront sensor. It came up from the effort of Roland Shack and Ben Platt to solve a problem brought forward by the US Air Force to the Optical Science center at the University of Arizona [20]. The objective was to improve the quality of the image of the stars and satellites taken from earth. As a solution to the problem Roland Shack and Ben Platt came up with the idea of replacing the Hartmann Screen by a two dimensional array of tiny lenses. The Hartmann Screen is a screen with an array of tiny holes, used in the Hartmann Screen test carried out by Johannes Hartmann to test the optics of a refracting telescope [20]. This modification enable them to capture reasonable amount of light coming from the satellite or the star which generally appear very faint due to the atmospheric affect.

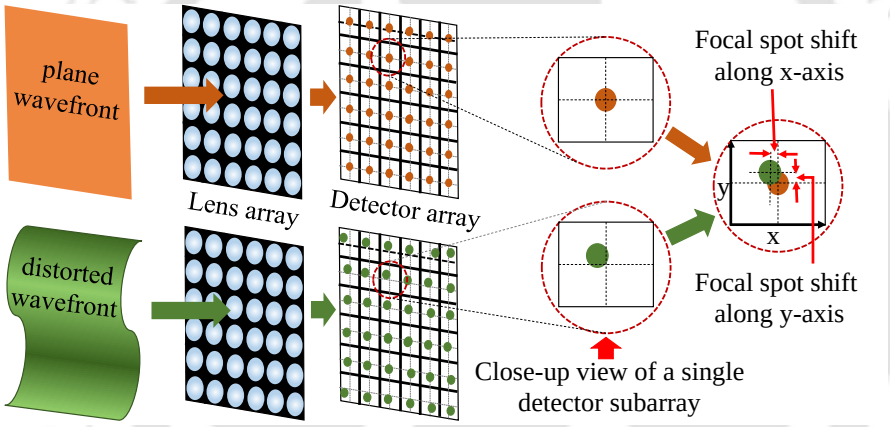


**Figure 2.3:** Principle of Shack-Hartmann wavefront sensor.

The principle of a Shack-Hartmann wavefront sensor is depicted in Fig. 2.3. The figure shows two situations, one when a beam with a plane wavefront transmits through the lens array and the other when the beam with a distorted wavefront transmits through the same. If all the lenses are identical and are arranged in a regular two dimensional array, the transmitted beam for a plane wavefront will give rise to a regular two dimensional array of focal spots at the focal plane of the array of lenses. The centroid of all the focal spots fall on the optical axes of the corresponding lenses of the lens array. However, on transmitting the beam with a distorted wavefront, the focal spots shift from their nominal position of the regular array (shown as a close-up view of a single detector subarray). A measure of the shift of the centroid of a certain focal spot along the $x$ and $y$ directions will give

the measure of the wavefront slope of the corresponding zone in the $x$ and $y$ directions, respectively. The slope information of all the zones are then combined to reconstruct the whole wavefront via an iterative process using appropriate mathematical algorithms [27, 28]. There are also algorithms based on the slope data to give a measure of the expansion co-efficients of various aberration modes present in the incident beam. Thus a zonal wavefront sensor follows an indirect approach to measure the strength of the aberration modes present in the incident wavefront. A modal wavefront sensor, in contrast, gives a direct measure of the amount of the aberration modes present in the incident beam.

## 2.5 Modal wavefront sensing

The modal wavefront sensor works on the principle that the focal plane intensity distribution has an unique behaviour for a given orthogonal aberration mode present in the beam. Such a sensor measures the strength of the various orthogonal aberration modes present in the incident beam and the incident wavefront is reconstructed by taking a linear combination of all the measured orthogonal modes. Though the idea of modal wavefront sensor started with the development of the curvature sensor by Roddier in 1988 [23], it was developed to a more useful form after Mark Neil in the year 2000 had reported the concept of obtaining the expansion co-efficient of a certain aberration mode present in the incident beam by deliberately introducing fixed amounts of the aberration mode with opposite polarity (called bias aberrations) into the incident beam [25]. The basic principle of a curvature sensor and the bias beam based modal wavefront sensor (also referred to as the Neil's modal wavefront sensor) is discussed below.

### 2.5.1 Curvature sensor

The curvature sensor is based on the measurement of the local wavefront curvature (second derivative of the wavefront surface) instead of the local wavefront slope (the first derivative of the wavefront surface) measurement done in a Shack-Hartmann wavefront sensor. The wavefront curvature can be obtained from the Laplacian of the wavefront surface, $W(x, y, z)$ [23] as,

$$\nabla^2 W(x, y, z) = \frac{\delta^2 W(x, y)}{\delta x^2} + \frac{\delta^2 W(x, y)}{\delta y^2} \tag{2.32}$$

To be note that $z$ dependency is removed from the RHS of Eq. 2.32 as the wavefront $W$ has $x$ and $y$ dependencies only as far as the derivatives are concerned. Figure 2.4 shows the basic principle of the curvature sensor. As shown in the figure, a converging lens $L_1$ of focal length $f$ focus the incident wavefront $W(x, y)$ on the focal plane $F$. The irradiance distribution is measured at two different planes $P_1$ and $P_2$ at a distance $\Delta z$ from $F$ situated before and after the focal plane, respectively. Another lens $L_2$ of focal length $f/2$ is placed at the plane $F$ to image $L_1$ at a distance $f$ behind the plane $F$, so as to make the two planes symmetric. A positive (or a negative) curvature of the wavefront increases (or decreases) the irradiance in one of the plane, whereas the irradiance in the other plane decreases (or increases). Thus, the difference between the irradiance distribution of these two planes will give a measure of the wavefront curvature or the Laplacian of the wavefront surface ($\nabla^2 W(x, y)$).

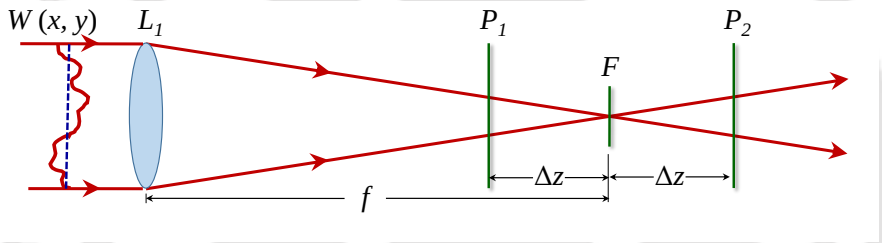


**Figure 2.4:** Principle of curvature sensor.

If $I_1$ and $I_2$ are the irradiance distributions at the defocus planes $P_1$ and $P_2$, respectively, then

$$I_1 = I_o - \frac{\delta I}{\delta z}\Delta z \tag{2.33}$$

$$I_2 = I_o + \frac{\delta I}{\delta z}\Delta z \tag{2.34}$$

where $\frac{\delta I}{\delta z} = I_o \frac{\delta W}{\delta n}\delta_c - I_o P_f \nabla^2 W$, $\delta_c$ is the linear Dirac distribution around the edge of the pupil, $\frac{\delta W}{\delta n}$ is the wavefront radial tilt at the edge, and $P_f(x, y)$ is the pupil function of the entrance pupil with an uniform illumination $I_o$ [45]. The output of the sensor is the normalized difference between the irradiance distributions at the two planes, such that

$$O = \frac{I_2 - I_1}{I_2 + I_1} = \frac{1}{I_o}\frac{\delta I}{\delta z}\Delta z = \left(\frac{\delta W}{\delta n}\delta_c - P_f \nabla^2 W\right)\Delta z \tag{2.35}$$

Equation 2.35 provides the measure of the local wavefront curvature ($\nabla^2 W$) inside the pupil and the wavefront tilt ($\frac{\delta W}{\delta n}$) at the edge. Thus the sensor provides all the required informations for the reconstruction of the wavefront. The wavefront $W$ can now be reconstructed by solving the Poisson's equation (Eq. 2.32) through an iterative process taking $\frac{\delta W}{\delta n}$ as the boundary condition.

### 2.5.2 Bias beam based modal wavefront sensor

Mark A Neil generalized the curvature sensor to come up with a more direct scheme referred to as bias based modal wavefront sensor. This wavefront sensor is capable of measuring the expansion co-efficient of each aberration mode directly. The scheme works by deliberately adding a positive and a negative amount of the aberration mode to the incident beam. It employs the orthogonal property of the aberration modes to measure the amplitudes or expansion coefficients of the various aberration modes present in the incident beam. The linear combination of all the aberration modes weighted by their corresponding measured amplitudes gives the reconstructed wavefront. Thus the wavefront reconstruction in this case is free from any iterative process, leading to instant measurement and reconstruction of the wavefront.

#### Basic principle

The basic principle of the bias beam based modal wavefront sensor or simply the modal wavefront sensor is depicted in Fig. 2.5. The sensor scheme requires the incident beam to be divided into two beams of identical wavefronts and equal intensities with the help of a 50% beam splitter. Both the beams are then allowed to pass through two separate phase plates (known as bias plates). One of the phase plates (the positive bias plate) adds a certain amount of a particular aberration mode to the beam transmitted through it, resulting in the positive bias beam, while the other (the negative phase plate) subtracts the exact amount of the same aberration mode from the reflected beam, resulting in the negative bias beam. The aberration mode added to or subtracted from the two beams can be called the bias aberration mode. Both the beams are then focused by two converging lenses to fall on two point detectors.

If the incident wavefront contains the bias aberration mode, the effective amplitude of the same aberration mode increases in one of the beam (say in the positive bias beam), while the other beam (say the negative bias beam) sees a decrease in

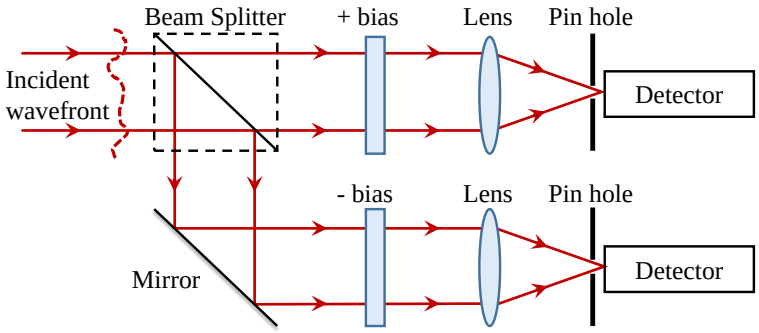


**Figure 2.5:** Principle of the bias beam based modal wavefront sensor.

amplitude of the aberration mode. This leads to decrease in central intensity ($I_1$) of the former beam at the corresponding detector and increase in intensity ($I_2$) of the later. Thus the difference in the central intensities ($\Delta I = I_2 - I_1$) of the two detectors gives us a measure of the amount of the particular aberration mode present in the incident beam. By changing the bias aberration mode it is possible to measure the various constituent aberration modes present in the incident beam.

### Theoretical considerations

We consider the incident beam to have a wave aberration $\Phi(r,\theta)$ and an uniform intensity distribution all over its cross section. Let bias aberrations $\pm\psi(r,\theta)$ are incorporated by the two phase plates to the two beams as seen in Fig. 2.5. The effective wavefront at the entrance pupil of the two lenses are

$$\begin{aligned} \Phi_+(r,\theta) &= \Phi(r,\theta) + \psi(r,\theta), \quad \text{due to a positive bias plate} \\ \Phi_-(r,\theta) &= \Phi(r,\theta) - \psi(r,\theta), \quad \text{due to a negative bias plate} \end{aligned} \tag{2.36}$$

Let the pinholes be so placed that the centers of the Gaussian reference spheres of the aberration free case, at the exit pupils of the two lenses are imaged at their corresponding detectors. The normalized intensities at the two detectors can be obtained from Eq. 2.11 as,

$$I_{1,2}(0) = \frac{1}{\pi^2}\left|\int_0^1\int_0^{2\pi} exp[i\Phi(r,\theta)\pm i\psi(r,\theta)]rdrd\theta\right|^2 \tag{2.37}$$

The sensor output thus can be expressed [25] as,

$$O = \Delta I = I_2(0) - I_1(0) \tag{2.38}$$

and the RMS wavefront error, $\Phi_{RMS}$ is given by

$$\Phi_{RMS} = \frac{O}{S} = \frac{\Delta I}{S} \tag{2.39}$$

where $S = \frac{\delta \Delta I}{\delta a}\Big|_{a=0}$ is the sensitivity of the sensor. The sensor output given by Eq. 2.38 is termed as type-A sensor output. Thus we write

$$\text{type-A sensor output} = O_A = I_2(0) - I_1(0) \tag{2.40}$$

and,

$$\Phi_{RMS}(\text{type-A}) = \frac{O_A}{S_A} = \frac{I_2(0) - I_1(0)}{S_A} \tag{2.41}$$

where $S_A$ is the sensitivity of type-A sensor. Let us now evaluate the sensitivity of the sensor for a specific aberration mode present in the incident beam. It is already discussed in section 2.2.2 that the wave aberrations can be expressed in terms of the Zernike polynomials $Z_j$. So, let us consider that the Zernike mode $Z_s$ is present in the incident wavefront and the Zernike mode $Z_b$ is used as the bias aberration. Thus, $\phi(r,\theta)$ and $\psi(r,\theta)$ can be expressed as $aZ_s(r,\theta)$ and $bZ_b(r,\theta)$, respectively, where $a$ and $b$ are their respective magnitudes. Therefore the expressions for intensities become

$$I_{1,2}(0) = \frac{1}{\pi^2}\left|\int_0^\infty \int_0^{2\pi} exp[iaZ_s \pm ibZ_b] r dr d\theta\right|^2 \tag{2.42}$$

Taking the partial derivative of $I_{1,2}(0)$ with respect to $a$ we have

$$\begin{aligned}
\frac{\delta I_{1,2}(0)}{\delta a} &= \frac{1}{\pi^2}\frac{\delta}{\delta a}\left[\int_0^\infty \int_0^{2\pi} exp[iaZ_s \pm ibZ_b] r dr d\theta \times \int_0^\infty \int_0^{2\pi} exp[-iaZ_s \mp ibZ_b] r dr d\theta\right] \\
&= \frac{i}{\pi^2}\left[\int_0^\infty \int_0^{2\pi} Z_s exp[iaZ_s \pm ibZ_b] r dr d\theta \times \int_0^\infty \int_0^{2\pi} exp[-iaZ_s \mp ibZ_b] r dr d\theta\right. \\
&- \left.\int_0^\infty \int_0^{2\pi} exp[iaZ_s \pm ibZ_b] r dr d\theta \times \int_0^\infty \int_0^{2\pi} Z_s exp[-iaZ_s \mp ibZ_b] r dr d\theta\right]
\end{aligned} \tag{2.43}$$

Thus,

$$S_A = \frac{\delta \Delta I}{\delta a}\Big|_{a=0} = \frac{\delta I_2(0)}{\delta a}\Big|_{a=0} - \frac{\delta I_1(0)}{\delta a}\Big|_{a=0} \tag{2.44}$$

$$\begin{aligned}
&= \frac{2i}{\pi^2}\left[\int_0^\infty \int_0^{2\pi} exp[ibZ_b] r dr d\theta \times \int_0^\infty \int_0^{2\pi} Z_s exp[-ibZ_b] r dr d\theta\right. \\
&- \left.\int_0^\infty \int_0^{2\pi} Z_s exp[ibZ_b] r dr d\theta \times \int_0^\infty \int_0^{2\pi} exp[-ibZ_b] r dr d\theta\right]
\end{aligned} \tag{2.45}$$

Now expanding the exponential terms using Maclaurin series considering $b$ to be very small, thereby neglecting the second and higher order terms.

$$\begin{aligned} S_A &= \frac{2i}{\pi^2}\left[\int_0^\infty\int_0^{2\pi}[1+ibZ_b]rdrd\theta \times \int_0^\infty\int_0^{2\pi}[Z_s - ibZ_sZ_b]rdrd\theta \right. \\ &- \left. \int_0^\infty\int_0^{2\pi}[Z_s + ibZ_sZ_b]rdrd\theta \times \int_0^\infty\int_0^{2\pi}[1-ibZ_b]rdrd\theta\right] \end{aligned} \tag{2.46}$$

Considering only the real part we get

$$S_A = \frac{4b}{\pi^2}\int_0^\infty\int_0^{2\pi} rdrd\theta \int_0^\infty\int_0^{2\pi} Z_sZ_brdrd\theta - \frac{4b}{\pi^2}\int_0^\infty\int_0^{2\pi} Z_brdrd\theta \int_0^\infty\int_0^{2\pi} Z_srdrd\theta \tag{2.47}$$

If $A$ is the area of the cross section of the beam at the entrance pupil of the lens, then

$$S_A = \frac{4bA}{\pi^2}\int_0^\infty\int_0^{2\pi} Z_sZ_brdrd\theta = \frac{4bA}{\pi^2}K\delta_{ab} \tag{2.48}$$

where $K$ is orthogonality constant and $\delta_{ab}$ is a Kronecker delta function. Here we assume that $Z_s$ and $Z_b$ have zero mean across A. Equation 2.48 indicates that the sensor is active only to the Zernike mode that is same as the bias aberration mode. Therefore this mode is referred to as sensor mode throughout the thesis. The above expression further indicates that for low aberration (when $a$ and $b$ are small) the sensor output for an aberration mode is not affected by the presence of other modes.

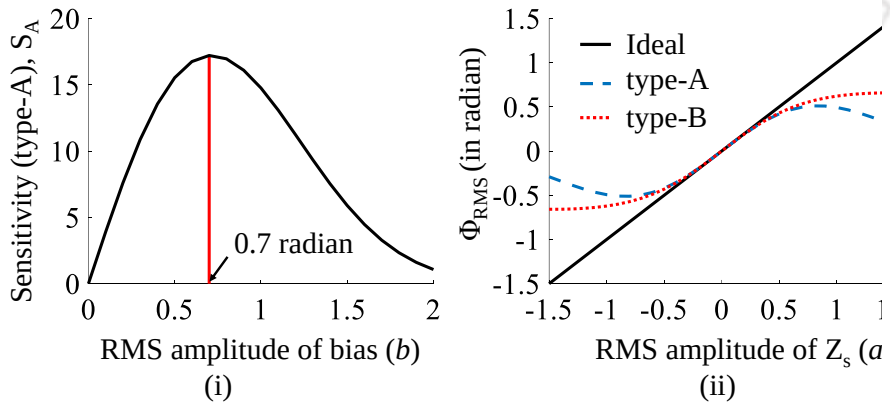


**Figure 2.6:** Plots of (i) sensitivity vs the sensor mode amplitude for the type-A sensor and (ii) $\Phi_{RMS}$ vs the sensor mode amplitude for type-A and type-B sensors using $Z_s = Z_5$ and $b = 0.7$.

The sensitivity of the type-A sensor ($S_A$) for a given sensor mode varies with the bias amplitude $b$. Figure 2.6 (i) shows the plot of $S_A$ versus $b$ for the sensor mode $Z_5$. It is noticed that the sensitivity of the sensor reaches the maximum at $b = 0.7$ radian. Therefore if the type-A sensor is to be operated with the maximum sensitivity so that it is able to sense a small change in aberration in a plane wave, the bias value is chosen as 0.7 radian.

### 2.5.3 Advantages and limitations of modal wavefront sensor

The modal wavefront sensor is advantageous for being simple in design devoid of any complicated geometry. Besides it gives a direct measure of the amplitudes of the aberration modes present in the incident beam. On the contrary the zonal wavefront sensor such as Shack-Hartmann wavefront sensor requires the implementation of a reconstruction algorithm to obtain a measure of the aberration modes present in the incident beam. The zonal wavefront sensor however can also use a pre-calculated map of the focal spot shifts to obtain the modal strengths quickly. However such mapping will not be a generic one and will require rebuilding under different conditions. The exclusion of the reconstruction algorithm in a modal wavefront sensor further increases the processing speed of the sensor which will be useful for high speed applications. The modal wavefront sensor can be a superior option in a situation when the input beam comprises a few low order aberration modes with small amplitudes. Thus relative advantage of the modal sensor with reference to a zonal sensor diminishes when the input beam has a large number of aberration modes. Further, it is found that the output of modal wavefront sensor assigned for a certain sensor mode is affected by the presence of a different mode (referred to as input mode) other than the sensor mode, thereby degrading the quality of the sensor output [35, 36, 37]. Such an affect can be called as the inter-modal cross talk. The affect of such crosstalk becomes particularly significant when the strengths of the aberration modes are large [37]. It is observed that in some cases the response of the sensor mode may even be lower than the response of the sensor for the input mode (i.e. the aberration mode other than the sensor mode present in the beam) [14]. Such a behaviour of the modal sensor is indicated by relatively large off diagonal elements of the sensitivity matrix.

Martin J Booth [29] modified the existing expression (Eq. 2.40) of sensor output to come up with two optimized expressions. The modified expressions termed as

type-B and type-C sensor outputs are expressed as,

$$\text{type-B sensor output}, O_B = \frac{I_2(0) - I_1(0)}{(I_2(0) + I_1(0))} \tag{2.49}$$

$$\text{type-C sensor output}, O_C = \frac{I_2(0) - I_1(0)}{(I_2(0) + \gamma I_o(0) + I_1(0))} \tag{2.50}$$

and RMS wavefront error, $\Phi_{RMS}$, can be represented as

$$\Phi_{RMS}(\text{type-B}) = \frac{O_B}{S_B} \text{ and } \Phi_{RMS}(\text{type-C}) = \frac{O_C}{S_C} \tag{2.51}$$

where, $S_B$ and $S_C$ are the sensitivities of the type-B and type-C sensing schemes, respectively, $\gamma$ is a constant chosen for optimum linear response and $I_o(0)$ is the central intensity of the ideal unaberrated beam. The type-B and type-C sensor output show some resilience to the effect of inter-modal cross talks.

Moreover, the sensor output of both the type-A and type-B sensors change as a linear function of the sensor mode amplitude only for a small range of values based on the value of the bias amplitude. Figure 2.6 (ii) shows the plots of $\Phi_{RMS}$ against the sensor mode amplitude for type-A and type-B sensors using $Z_s = Z_5$ and $b = 0.7$. It is noticed that the linear response range is limited to $\approx \pm 0.3$ radian only.

Booth further suggested that by increasing the amplitude of the bias aberration, the range of linear response of the type-A, type-B and type-C sensors can be increased. However, the improvement in linear response of the three type of sensors comes at the expense of sensitivity. There were also efforts to improve the linear response and inter-modal cross talk immunity of the type-B sensor further by using a weighted average intensity measurement over a certain detector aperture instead of the central intensity measurement [38], although it comes at the expense of sensitivity and speed of the sensor. The effect of inter-modal crosstalk can also be reduced significantly in another scheme [46], however, this requires the use of Karhunen-Loève mode in lieu of Zernike modes.

Thus it appears that the inter-modal cross talk and linear response are two important limitations of the modal wavefront sensor as they can have a severe impact on the accuracy of the sensor output. We will therefore present a detail discussion on both these issues in the later chapters.

## 2.6 Conclusion

In this chapter we have introduced monochromatic wavefront aberrations using the scaler diffraction theory. We have further showed that the root mean square wavefront error, in case of small ($\approx 0.3$ radian) aberration, can be expressed in terms of the normalized intensity or the Strehl ratio at the center of the Gaussian reference sphere of the image plane. We have also discussed the properties of Zernike polynomials and showed how they can be used to represent the wavefront aberrations. This is followed by the introduction of wavefront sensing and wavefront sensors. We have focused our discussion on the modal wavefront sensor which provides a direct way of measuring the strength of the constituent aberration modes in an incident beam, in contrast to the indirect way of measuring the aberration mode strengths in the zonal wavefront sensors. We have also elaborated on the important advantages and limitations of the modal wavefront sensor.

# Chapter 3

# Computer Generated Holography and Holographic Modal Wavefront Sensor

## 3.1 Introduction

After the discussion on wavefront aberrations and the principle of the modal wavefront sensor in the previous chapter, in this chapter we discuss about the implementation of the modal wavefront sensor using computer generated holograms. The chapter begins with a brief introduction to holography and computer generated holograms. It then discusses the use of computer generated holography technique to generate a beam with a user defined phase profile directed at a user defined propagation direction. The later part of the chapter then elaborates the working principle of holographic modal wavefront sensor. Numerical simulations are also carried out using the principle of the holographic modal wavefront sensor and simulation results are presented towards the end of the chapter.

## 3.2 Principle of holography

The basic idea of holography and hologram were developed by Dennis Gabor in 1948 for which he was awarded the Nobel Prize in Physics in 1971 [40]. A hologram is a record of the interference pattern of two mutually coherent beams, one of the beams called the object beam is reflected by an object while the other is called

the reference beam. The object beam has a wavefront whose shape carries the information of the object while the reference beam has a simple wavefront such as a plane wavefront. The process of recording of a hologram is depicted in Fig. 3.1. The recorded hologram can be used to reconstruct the object beam wavefront. In this process the hologram is placed in the exact position as during recording and it is illuminated by the reference beam. The hologram diffracts the reference beam into three beams including the undiffracted beam. One of the diffracted beams has the same wavefront as the object beam and the other is the complex conjugate of the object beam. When one looks through the hologram along the reconstructed object beam a virtual image of the object will be seen at the same location where the object was kept. Thus holography makes it possible to reconstruct the wavefront of an object beam which was used to construct the hologram [47].

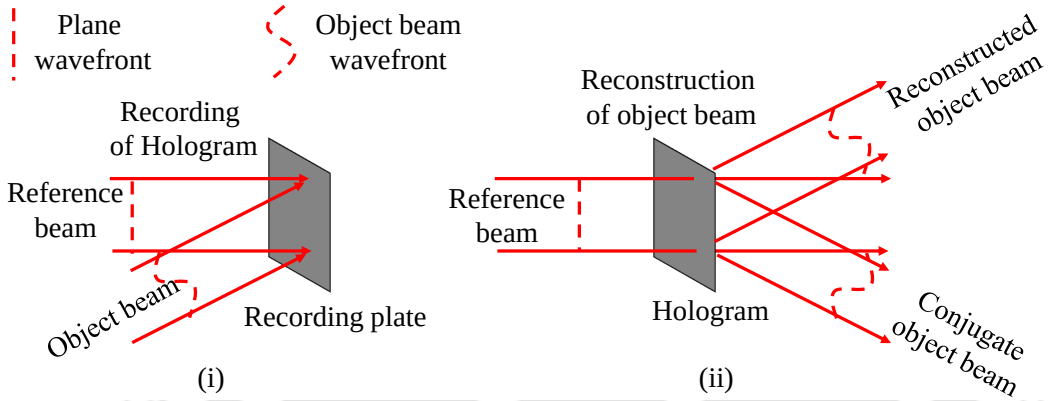


**Figure 3.1:** (i) The recording of the hologram and (ii) reconstruction of the wavefront of the object beam using the hologram.

The reconstructed image obtained by using the hologram contains the information of both intensity and depth contrary to that of the conventional photography where only the intensity information is recorded. Therefore a hologram contains the whole information of the test object, giving rise to the name 'hologram', where 'holos' and 'gramma' are Greek words meaning whole or complete and message, respectively. From the principle of holography it is clear that if a hologram due to a reference beam and an object is constructed correctly the corresponding object beam can be reconstructed even if the object is not present. Thus the primary task to generate any arbitrary wavefront is to record the appropriate interference pattern, which can often be computed for the given mathematical expressions of the object beam and the reference beam using a computer. If a hologram is fabricated

using such an interference pattern then the same is called the computer generated hologram and the whole construction and reconstruction is called the computer generated holography [40].

## 3.3 Computer generated holography and binary holograms

Let $\phi_R(x,y)$ and $\phi_O(x,y)$ be the functions representing the phase profiles of the reference beam and the object beam, respectively, in a plane described by $(x,y)$ coordinates. The complex amplitudes of the reference beam and the object beam are expressed as $A_R = A_{Ro}exp\{i\phi_R(x,y)\}$ and $A_O = A_{Oo}exp\{i\phi_O(x,y)\}$, respectively. We also assume that the object beam and the reference beam are making a certain angle with one another and tilt of the object beam with respect to the XY plane is represented by $\tau(x,y) = m_x x + m_y y$ (where $m_x$ and $m_y$ are numbers representing the amount of tilts in the $x$ and $y$ directions, respectively). Thus we can write $\phi_O(x,y) = \phi_o(x,y) + \tau(x,y)$, where $\phi_o(x,y)$ is the phase variation with respect to the plane perpendicular to the propagation direction of the object beam. Assuming the two beams to be mutually coherent, the superposition of the two beams at the plane of interference, which also is the XY plane, can be expressed as

$$A_R + A_O = A_{Ro}exp\{i\phi_R(x,y)\} + A_{Oo}exp\{i\phi_O(x,y)\} \tag{3.1}$$

Thus the intensity in the plane of interference is

$$\begin{aligned} I &= (A_{Ro}exp\{i\phi_R(x,y)\} + A_{Oo}exp\{i\phi_O(x,y)\}) \\ &\times (A_{Ro}exp\{-i\phi_R(x,y)\} + A_{Oo}exp\{-i\phi_O(x,y)\}) \\ &= A_{Ro}^2 + A_{Oo}^2 \\ &+ A_{Ro}A_{Oo}\,[exp\{i(\phi_O(x,y) - \phi_R(x,y))\} + exp\{-i(\phi_O(x,y) - \phi_R(x,y)\}] \\ &= A_{Ro}^2 + A_{Oo}^2 + 2A_{Ro}A_{Oo}\,cos[\phi_O(x,y) - \phi_R(x,y)] \\ &= I_{Ro} + I_{Oo} + 2\sqrt{I_{Ro}I_{Oo}}\,cos[\phi(x,y)] \end{aligned} \tag{3.2}$$

where $\phi(x,y) = \phi_O(x,y) - \phi_R(x,y)$. The first two terms of Eq. 3.2 contribute a fixed amount of intensity while the third term represents a co-sinusoidal intensity variation leading to formation of interference fringes. It is to be noted that the

reference beam usually has a plane wavefront. Therefore in such a case we may write $\phi_R(x, y) = 0$ and hence $\phi(x, y) = \phi_O(x, y)$. Let us now consider a plane reference wavefront as shown in Fig. 3.2 and a tilted object beam wavefront inclined along the $x$ axis. Therefore in this case there is no extra phase other than the tilt and thus $\phi_o(x, y) = 0$. The superposition of these two wavefronts gives rise to an interference

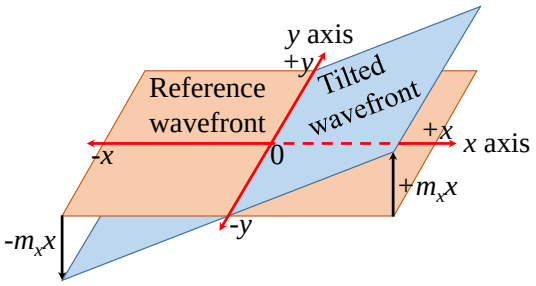


**Figure 3.2:** Representation of a plane reference wavefront and a tilted wavefront.

pattern similar to the one shown in Fig. 3.3(i) which is computed using tilt function $\tau(x, y) = m_x x + m_y y$ where $m_x$ and $m_y$ are taken as $5\pi$ and 0, respectively. The computation of interference pattern is carried out in a square area of the XY plane described by $x = -1 \rightarrow 1$ and $y = -1 \rightarrow 1$. A plot of the normalized intensity along the $x$ axis shows a co-sinusoidal variation as in Fig. 3.3(ii). The co-sinusoidal

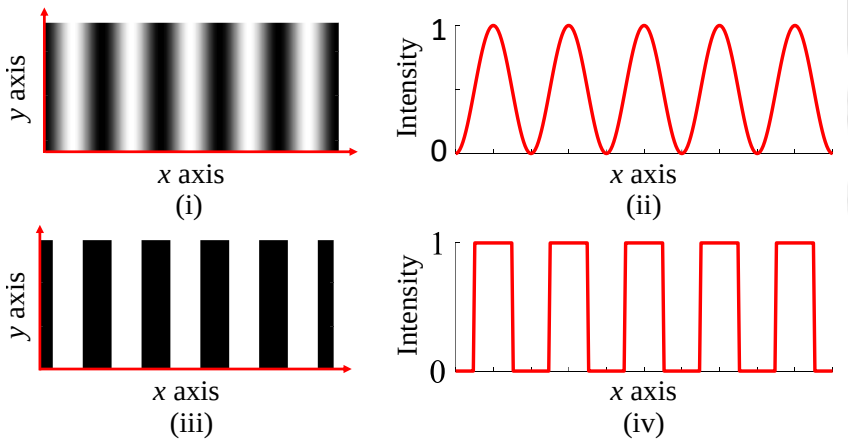


**Figure 3.3:** (i) Computed interference pattern, (ii) plot of the normalized intensity of the interference fringes along the $x$ axis, (iii) binarized interference pattern and (iv) line plot of the binarized interference pattern along the $x$ axis.

intensity variation can be binarized by putting a threshold condition such that

$$b(x,y) = \begin{cases} 1, & \text{for} \quad cos[\phi(x,y)] \geq 0 \\ 0, & \text{for} \quad cos[\phi(x,y)] < 0 \end{cases} \tag{3.3}$$

Figures 3.3(iii) and (iv) show the binarized interference pattern and a line plot along $x$.

The phase function $\phi_o(x,y)$ can also be represented by the Zernike polynomials Figure 3.4(i) shows the binarized interference pattern when the object beam has a


**Figure 3.4:** Binary interference fringes with (i) $\phi(x,y) = 0$, $m_x = 5\pi$, $m_y = 0$, (ii) $\phi(x,y) = Z_7$, $m_x = 5\pi$, $m_y = 0$, (iii) $\phi(x,y) = 0$, $m_x = 3\pi$, $m_y = 0$ and (iv) $\phi(x,y) = 0$, $m_x = 5\pi$, $m_y = 5\pi$.

plane wavefront with an $x$ tilt which is computed by taking $\phi_o(x,y) = 0$, $m_x = 5\pi$ and $m_y = 0$. Whereas Fig. 3.4(ii) shows the binarized interference pattern when $\phi_o(x,y) = Z_7$ and the same values of $m_x$ and $m_y$ as in Fig. 3.4(i). Further, Fig. 3.4(iii) shows the binarized interference pattern when the wavefront of the object beam has a smaller tilt compared to Fig 3.4(i) which is computed using $\phi_o(x,y) = 0$, $m_x = 3\pi$ and $m_y = 0$. On the other hand Fig. 3.4(iv) shows the interference fringes when $\phi(x,y) = 0$, $m_x = 5\pi$ and $m_y = 5\pi$, i.e. in the presence of a diagonal tilt. Thus it is observed that the presence of $\phi_o(x,y)$ changes the shape of the interference fringes while any change in the tilt function modifies the width and the orientation of the interference fringes.

If a hologram is fabricated using the computed interference pattern between an object beam and a reference beam, with the transmittance function proportional the computed interference pattern, such a hologram is called a computer generated hologram (CGH). A CGH can be designed using the binarized interference pattern $b(x,y)$ as the amplitude transmittance value at $(x,y)$ which is termed binary amplitude CGH. Instead of describing the amplitude transmittance, the product

$\pi \times b(x, y)$ can be used to describe the phase delay introduced by the hologram. Such a CGH is called binary phase CGH. The expression of $b(x, y)$ can also be used to define a saw tooth wave varying from 0 to $2\pi$ instead of each square wave in the case of binary phase CGH and such a hologram is called blazed grating CGH. All the holograms implemented in this thesis work are CGH however in the rest of the thesis we will call them just holograms instead of CGH.

In an experimental setup the beam forming optics usually has a circular aperture, hence, the hologram designed should also have a circular aperture. Thus we define the transmittance of the binary amplitude hologram as $H(x, y) = t(x, y) \times circ(x, y)$, where $circ(x, y)$ represents a unit circle. Figure 3.5(i) shows such a binary amplitude hologram designed using $\phi_o(x, y) = 0$, $m_x = 5\pi$ and $m_y = 0$. We then assume that the hologram is illuminated by a collimated beam, which is nothing but the reference beam used to compute the interference pattern. The hologram is kept at the front focal plane of a lens of focal length $f$. Now, following Eqs. 2.10 and 2.31 and considering the optical system to be a single lens and the image plane for the system to be the back focal plane of the lens, the amplitude distribution at the image plane can be written as [40],

$$\mathscr{F}(u, v) = \frac{A}{j\lambda f} \times \iint_{-\infty}^{\infty} H(x, y) \exp\left[-j\frac{2\pi}{\lambda f}(xu + yv)\right] dxdy \tag{3.4}$$

It is seen that $\mathscr{F}(u, v)$ is nothing but the Fourier transform of $H(x, y)$ in Cartesian coordinates, where, $(u, v)$ are the coordinates of the back focal plane, $A$ and $\lambda$ are the amplitude and the wavelength of the incident beam. The intensity distribution at the focal plane of the lens can be obtained from the modulus square of $\mathscr{F}(u, v)$ i.e. $I(u, v) = |\mathscr{F}(u, v)|^2$. Thus the intensity distribution at the back focal plane of the lens can be computed by taking Fourier transform of $H(x, y)$. Figures 3.5(ii) and (iii) show the computed intensity distribution in the focal plane due to a binary amplitude hologram and a binary phase hologram, respectively. The Fourier plane due to a binary amplitude hologram comprises 0 order and other higher orders ($\pm 1$, $\pm 3$, $\pm 5$, etc) positioned symmetrically on both sides of the zero order while the 0 order is absent in case of the Fourier plane due to the binary phase hologram. It is also observed that the intensity of the individual diffraction order decreases as the diffraction order increases.

The formation of the diffraction orders as seen above can be understood from

the Fourier series expansion of the transmittance function of the hologram.


**Figure 3.5:** (i) A binary amplitude hologram with $\phi_o = 0, m_x = 5\pi, m_y = 0$, and the computed intensity distribution in the focal plane due to (ii) a binary amplitude hologram and (iii) a binary phase hologram.

The Fourier series of a periodic function $f(x)$ can be written as,

$$f(x) = \frac{a_0}{2} + \sum_{n=1}^{\infty} a_n cos(nx) + \sum_{n=1}^{\infty} b_n sin(nx) \tag{3.5}$$

where, the Fourier coefficients $a_0$, $a_n$ and $b_n$ are given by

$$\begin{aligned} a_0 &= \frac{1}{2\pi}\int_{-\pi}^{\pi} f(x)dx, \\ a_n &= \frac{1}{\pi}\int_{-\pi}^{\pi} f(x)cos(nx)dx, \quad \text{and} \\ b_n &= \frac{1}{\pi}\int_{-\pi}^{\pi} f(x)sin(nx)dx \end{aligned} \tag{3.6}$$

Thus, the Fourier series expansion of the transmittance function $H(x, y)$ of a binary amplitude hologram can be written as [48],

$$\begin{aligned} H_B(x,y) = \frac{1}{2} + \frac{1}{\pi}\Bigg[&[\exp(i\phi) + \exp(-i\phi)] - \frac{1}{3}[\exp(i3\phi) + \exp(-i3\phi)] \\ &+ \frac{1}{5}[\exp(i5\phi) + \exp(-i5\phi)] + ...\Bigg] \end{aligned} \tag{3.7}$$

The different terms from left to right on the right hand side of Eq. 3.7 represent the 0, +1, -1, +3, -3, +5, -5, etc. diffraction orders. However, for a binary phase hologram the first term of Eq. 3.7 vanishes. The ±1, ±3, ±5, etc. diffraction orders carry phase profiles $\pm\phi$, $\pm 3\phi$, $\pm 5\phi$, and so on with relative intensities of 1, $\frac{1}{9}$, $\frac{1}{25}$, respectively. Moreover, the ±1, ±3, ±5, etc. orders have an overall tilt of $\pm\tau$, $\pm 3\tau$, $\pm 5\tau$, etc., respectively. Thus the +1 order beam has the complex amplitude $exp\{i\phi\}$

same as the object beam and the -1 order has the complex amplitude $exp\{-i\phi\}$. If the beam incident on the hologram has a phase profile say $\phi_R(x, y)$ then the complex amplitude of the +1 and -1 order will be

$$exp\{i\phi\} = exp\{i(\phi_R \pm \phi_o)\} \tag{3.8}$$

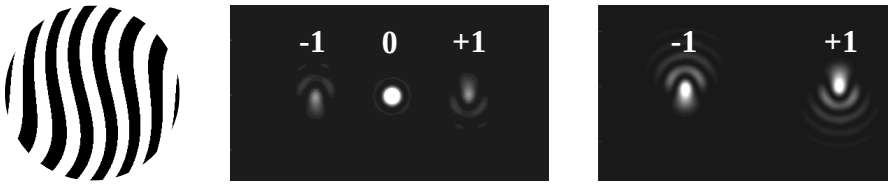


**Figure 3.6:** (i) A binary hologram with $\phi(x, y) = Z_7$, $m_x = 7\pi$, $m_y = 0$, Fourier plane representation when the binary hologram of (i) is (ii) an amplitude hologram and (iii) a phase hologram.

Figure 3.6(i) shows a binary hologram using $\phi_o(x, y) = Z_7$ and an $x$ tilt while Figs. 3.6(ii) and (iii) are the Fourier plane representations when the binary hologram shown in Fig. 3.6(i) is an amplitude hologram and a phase hologram, respectively. It is clear from the figure that the $\phi_o = Z_7$ gives rise to a comatically aberrated focal spot as already discussed in the previous chapter.

The co-efficient of $exp\,[i\phi]$ in the Eq. 3.7 represents the amplitude of the beam as a fraction of incident amplitude. Thus $|\frac{1}{\pi}|^2 \times 100\% \approx 10\%$ is theoretical or maximum diffraction efficiency into the +1 diffraction order (i.e. the percentage of optical power of the incident beam which is diffracted in to the +1 order). It is to be noted that the diffraction efficiency of a binary phase hologram can go up to a maximum of $\sim 40\%$ (theoretical) [49]. This efficiency can be further enhanced if the hologram is designed in the form of a blazed grating in which case the theoretical diffraction efficiency becomes 100% [50].

### 3.3.1 Positioning of the +1 order beam and the concept of multiplex hologram

We consider four different binary holograms constructed using $\phi_o(x, y) = 0$, $(m_x = 7\pi, m_y = 0)$, $(m_x = 3\pi, m_y = 0)$, $(m_x = 5\pi, m_y = 5\pi)$, and $(m_x = 0, m_y = 7\pi)$. We then compute the Fourier plane considering the hologram to be a phase hologram.

Figures 3.7(i-a,b) → (iv-a,b) show the binary holograms and their respective Fourier

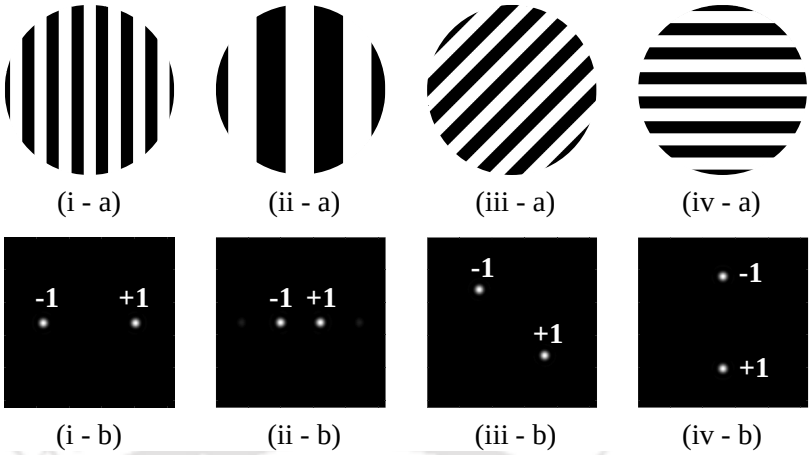


**Figure 3.7:** Representation of (a) binary phase holograms and (b) their respective Fourier plane intensity distribution for $\phi_o(x, y) = 0$ and (i) $m_x = 7\pi$, $m_y = 0$, (ii) $m_x = 3\pi$, $m_y = 0$, (iii) $m_x = 5\pi$, $m_y = 5\pi$, and (iv) $m_x = 0$, $m_y = 7\pi$.

plane intensity distributions. It is evident from the above examples that designing holograms with different combinations of $(m_x, m_y)$ values facilitate positioning of the +1 or the -1 order beams over and above defining the phase profile carried by the beam. However, it is to be noted that if the hologram is realized on a pixellated device comprising say $N \times N$ pixels (called the hologram dimension), the $m_x$ or $m_y$ can have a maximum value of $N\pi/2$ due to the Nyquist rate [51].

The position of the $\pm 1$ orders in the Fourier plane (i.e. the position co-ordinates $u$ and $v$ as in Eq. 3.4) can also be calculated for a given illumination wavelength ($\lambda$) and hologram dimension ($N$). If $k_x$ and $k_y$ are the corresponding Fourier plane coordinates then $k_x = \frac{u}{\lambda f}$ and $k_y = \frac{v}{\lambda f}$. On the other hand $k_x$ and $k_y$ are related to $m_x$ and $m_y$ as [48],

$$k_{x,y} = \frac{m_{x,y}}{\pi \times N \times \text{pixel pitch}} \tag{3.9}$$

Thus, the value of $k_{x,y}$ can be calculated from the known values of $m_{x,y}$, $N$ and pixel pitch (size of each pixel). The coordinate of the +1 order in the focal plane of the lens is thus given by, $u = k_x \lambda f$ and $v = k_y \lambda f$, with the undiffracted 0 order at the location $(u = 0, v = 0)$.

The holograms discussed so far generates just one pair of +1 and -1 order beams hence they belong two a group of singlex holograms. Instead of a single pair of +1 and -1 diffraction orders one can also generate multiple pairs of +1 and -1 diffraction orders and the hologram in such a case can be called as multiplex hologram. A

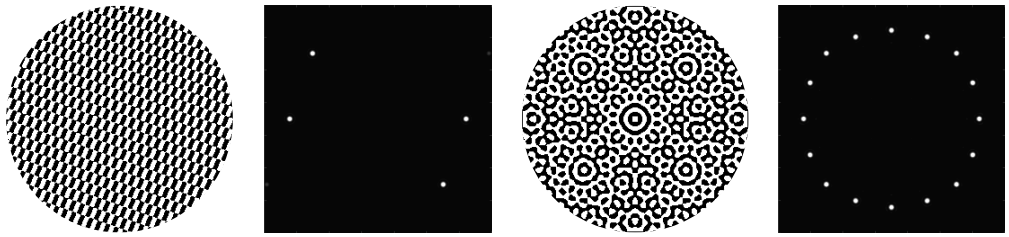

(i) (ii) (iii) (iv)

**Figure 3.8:** (i) A binary duplex phase hologram and (ii) its Fourier plane representation, (iii) a binary multiplex phase hologram and (iv) its Fourier plane representation.

multiplex hologram is constructed considering a single reference and a multiple of object beams each coming at a different angle. Let us consider that there are $n$ object beams each with a phase profile $\phi_i(x, y)$ and tilt function $\tau_i(x, y)$. Thus the net complex amplitude in the interference plane assuming unit amplitude across the beam cross section can be written as $exp\{i\phi(x, y)\} = \sum_{i=1}^{n}[exp\{i\,(\phi_i(x, y) + \tau_i(x, y))\}]$. The binary transmittance function of the multiplex hologram is constructed using the algorithm,

$$H_n(x, y) = \begin{cases} 1, & \text{for} \quad cos[\phi(x, y)] \geq 0 \\ 0, & \text{for} \quad cos[\phi(x, y)] < 0 \end{cases} \tag{3.10}$$

Figures 3.8(i) and (iii) show a multiplex binary phase hologram using two and eight object beam phase profiles, respectively, while Figs. 3.8(ii) and (iv) show the corresponding Fourier planes. A multiplex hologram using two object beam phase profiles can be termed as duplex hologram. The tilt function of each of the object beams in the case of the multiplex hologram shown in Fig. 3.8(iii), is so defined that the $+1$ and $-1$ orders at the Fourier plane are arranged in a circle.

Thus, the use of singlex hologram facilitates the generation of a user defined phase profile and that can be sent to a user defined location of the Fourier plane. Further, the use of multiplex hologram enables the generation of multiple diffracted beams, where each beam can have a desired phase profile and can be sent to a desired location of the Fourier plane.

## 3.4 Holographic modal wavefront sensor

Equation 3.8 expresses the phase profile of the +1 and -1 order beams diffracted by a binary hologram designed by using a plane reference wavefront and an object

beam phase function $\phi_o$. Thus if the incident beam has a phase profile $\phi_R$ then the resultant phases of the +1 and -1 orders are given as $\phi_R+\phi_o$ and $\phi_R-\phi_o$, respectively. Hence for an incident beam carrying a phase function $\phi_R$, the +1 and -1 order beams act as the positive and negative bias beams of a modal wavefront sensor as introduced in the previous chapter. In this case we need to describe $\phi_o = bZ_s$, where $Z_s$ is the sensor mode to be measured and $b$ is the bias amplitude. A modal wavefront sensor thus implemented using this property of computer generated holograms is termed as holographic modal wavefront sensor (HMWS). Figure 3.9(i) illustrates the principle

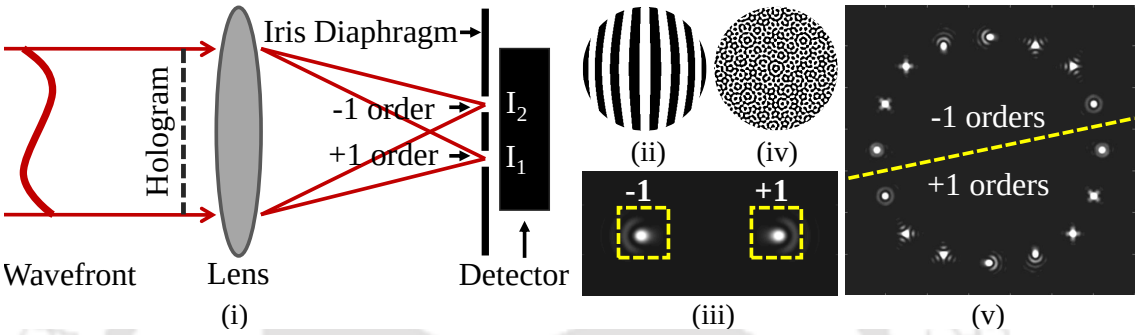


**Figure 3.9:** (i) Principle of a holographic modal wavefront sensor, (ii) a binary phase hologram using $\phi_o = 0.7Z_7$, (iii) its Fourier plane, (iv) a binary multiplex phase hologram with different Zernike modes as $\phi_o$ and (v) its Fourier plane.

of a holographic modal wavefront sensor. The incident wavefront falls on the binary hologram. The binary hologram can be fabricated as a phase plate, a photographic film, a print on a polyester film or can be a spatial light modulating device. The light diffracted by the hologram is collected by a lens and is focused onto two pinhole detectors. The $m_x$ and $m_y$ values of the tilt function $\tau(x, y)$ of the binary hologram are chosen in such a way that the +1 and -1 order beams are focused with the focal spots centered on the two pinholes. The central intensities of the +1 and the -1 diffraction orders are the intensities $I_1$ and $I_2$ appeared in the expression (Eq. 2.38) of the sensor output. Thus the amplitude of the sensor mode $Z_s$ can be measured from the intensities of the +1 and the -1 diffraction orders using Eq. 2.38. Figure 3.9(ii) shows a binary hologram using $\phi_o = 0.7Z_7$ while the computed intensity distribution in the focal plane with the two bias orders are seen in Fig. 3.9(iii).

A realistic incident beam may comprise not just one aberration modes but several aberration modes. The scheme described above allows the measurement of just one aberration mode. In order to measure multiple aberration modes present in a beam the following two schemes can be employed.

### 3.4.1 Sequential measurement scheme

In the case of sequential measurement, each of the aberration modes is measured in a sequence using a singlex binary hologram that is modified for each sensor mode. Thus in this scheme only one aberration mode is measured at a time. The measurement can be carried out in three ways

1. Using a singlex hologram and a single point detector. Here only one among the +1 and -1 orders, say the +1 order, is chosen to fall on the detector and the positive and the negative bias are applied one after the other by updating the phase function $\phi_o(x, y)$ of the binary hologram keeping $m_x$ and $m_y$ same. The process is repeated sequentially for the measurement of each aberration mode.

2. Using a singlex hologram and two point detectors. Here both the +1 and -1 order beams are chosen to fall on the two detectors and the +1 and -1 order beams act as the positive and negative bias beams, respectively, as in the case of the scheme in Fig. 3.9. The process is repeated sequentially for the measurement of all other modes.

3. Using a duplex hologram and two point detectors. A duplex hologram gives rise to two pairs of +1 and -1 orders. Here either the two +1 or the two -1 orders are allowed to fall on the two detectors. The two object beams are so chosen such that one +1 order beam acts as the positive bias beam and the other acts as the negative bias beam. The process is also repeated sequentially for the measurement of all the aberration modes present.

### 3.4.2 Simultaneous measurement scheme

In the case of simultaneous measurement, the measurements of all the modes under consideration are carried out simultaneously. This can be achieved with the help of a multiplex hologram (shown in Fig. 3.9(iv)). The measurement can be carried out in two ways

1. Using a multiplex hologram and an array of detectors. Here each of the object beam corresponding to the multiplex hologram is given a tilt so that all the pairs of +1 and -1 orders fall at different locations on the focal plane. The object beam phases are so chosen that a pair of the +1 and -1 order beams

associated with a particular object beam will act as the positive and the negative bias beams for the measurement of a certain aberration mode. There will be $k$ number of such pairs if $k$ number of aberration modes are to be measured.

2. Using a multiplex hologram and an array of detectors. However in this case in order to measure the presence of $k$ number of aberration modes $2k$ number of +1 order beams are generated. For each aberration mode there are two +1 order beams whose phase profiles are described to act as the positive and negative bias orders. Therefore compared to the previous one, this scheme requires twice the number of object beams to construct the multiplex hologram.

Thus, the sequential measurement scheme involves a singlex or a duplex holograms, whereas the simultaneous measurement scheme requires multiplex holograms to measure multiple aberration modes. In the following section both the HMWS schemes are validated through numerical simulations.

## 3.5 Simulation results and discussion

The numerical simulations are carried out employing the second scheme for sequential measurement and the first scheme for the simultaneous measurement. Binary holograms are constructed considering eight aberration modes (Zernike modes) namely $Z_4$, $Z_5$, $Z_6$, $Z_7$, $Z_8$, $Z_9$, $Z_{10}$, and $Z_{11}$ to be present in the incident beam. In the sequential measurement scheme a singlex hologram is constructed for each aberration mode where the +1 order beam is used as the positive bias beam and the -1 order beam is used as the negative bias beam. On the other hand in case of the simultaneous measurement scheme, a multiplex hologram is constructed to generate eight pairs of $+1$ and $-1$ orders to act as eight pairs of positive and negative bias beams. Thus, each pair of positive and negative bias beams gives the measure of a specific Zernike mode. The simulation results are obtained for two sets of arbitrarily chosen Zernike mode combinations representing the incident phase $\phi_1(x, y) = -0.5Z_5$ and $\phi_2(x, y) = 0.2Z_4 + 0.5Z_5 - 0.4Z_6 - 0.3Z_9 + 0.2Z_{10})$, where the co-efficients of the Zernike modes are in radians.

Complex amplitude in the focal plane is computed by taking the Fourier transform of the product of the hologram transmittance function and the complex amplitude of the incident beam. The RMS wavefront error, $\Phi_{RMS}$, is calculated using Eqs. 2.49 and 2.39, i.e. using the type-B sensing scheme. Figures 3.10(i) $\rightarrow$ (iii)

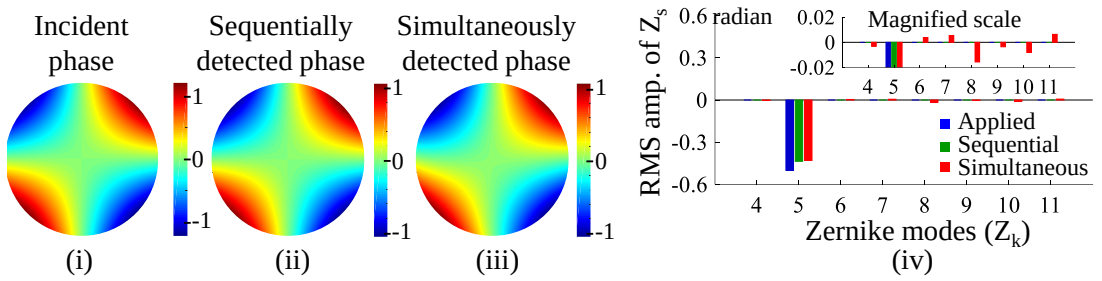


**Figure 3.10:** False color representation of the (i) incident phase profile, (ii) sequentially detected phase, (iii) simultaneously detected phase and (iv) bar plots of the RMS amplitudes of the sensor modes present in the incident phase, sequentially detected phase and simultaneously detected phase for the Zernike mode combination $\phi_1(x, y)$.

show the false color representations of the phase profile of the incident beam, estimated phase profile through sequential measurement and estimated phase profile through simultaneous measurement, respectively, for the incident phase $\phi_1(x, y)$. While Fig. 3.10(iv) shows the bar plot representation of the applied and estimated RMS amplitudes of the sensor modes for the Zernike mode combination corresponding to $\phi_1(x, y)$. Since $\phi_1(x, y)$ contains only the Zernike mode $Z_5$, it is seen that the measured phase, through both the sequential and the simultaneous measurement schemes, is predominately due to $Z_5$. Similarly, Figs. 3.11(i) $\rightarrow$ (iii) show

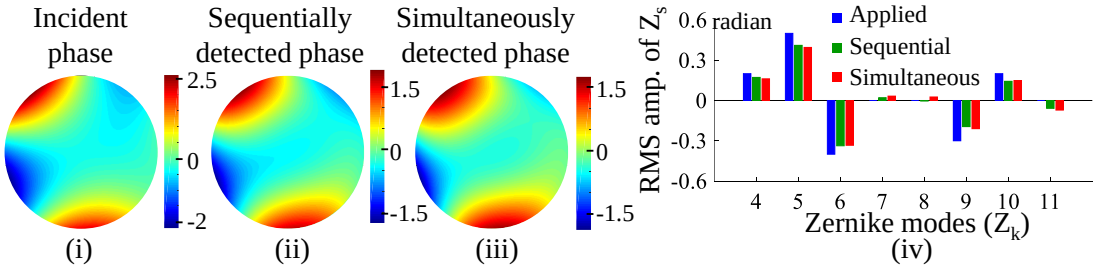


**Figure 3.11:** False color representation of the (i) incident phase, (ii) sequentially detected phase, (iii) simultaneously detected phase and (iv) bar plots of RMS amplitudes of the sensor modes present in the incident phase, sequentially detected phase and simultaneously detected phase for the Zernike mode combination $\phi_2(x, y)$.

the false color representations of the incident phase, sequentially estimated phase and simultaneously estimated phase, respectively, for the incident phase $\phi_2$. While Fig 3.11(iv) shows the bar plot representation of the RMS amplitudes of the sensor modes present in the incident beam, sequentially estimated and simultaneously estimated for the incident phase $\phi_2(x, y)$. In both the figures (Figs. 3.10 and 3.11),

the blue, green and red color bars represent the RMS amplitudes of the applied Zernike modes, sequentially and simultaneously measured RMS amplitudes of the Zernike modes, respectively. The figures indicate a close resemblance of the measured phase and the measured RMS amplitudes of the sensor modes relative to those that are applied to the incident beam phase. The disagreement between the two can be attributed to the low linear response, inter-modal cross talk and improper multiplexing due to limited number of pixels used in the simulation.

The modal wavefront sensor implemented above using a dynamic computer generated hologram has all the benefits of the conventional modal wavefront sensor, besides being highy flexible [34]. The high flexibility facilitates modal estimation over several aberration modes in a sequential manner without any modification of the set up. Also in comparison to a conventional sensor, such a holographic modal wavefront sensor can be optimized to work under different light conditions. The sensor also can be used to implement a closed loop adaptive optics system which is not possible with a conventional sensor.

## 3.6 Conclusion

In this chapter we have carried out a detail discussion on the computer generated holography technique. We have elaborated the computation of interference patterns from the prior knowledge of the reference beam and the object beam phase profiles, which further leads to the development of the computer generated hologram. The formation of a beam with a user defined phase profile and how that can be sent to a user defined location with the help of a computer generated holograms have also been discussed. Towards the later part of the chapter we have discussed about the implementation of a modal wavefront sensor using the diffraction properties of the computer generated holograms in which case the sensor is called the holographic modal wavefront sensor. We have also discussed about two schemes of measurements using the holographic modal wavefront sensor and presented a few simulation results using the two schemes.

# Chapter 4

# Experimental Implementation of the Holographic Modal Wavefront Sensor

## 4.1 Introduction

In this thesis work, we employ different experimental arrangements. In the present chapter we start with a discussion on the various important devices used in the experimental implementations. This is followed by a discussion on an inherent issue of liquid crystal spatial light modulators, a crucial device of all the experimental arrangements, that leads to fluctuation of the light beam reflected from the device. We conclude the chapter by describing the experimental implementation of the holographic modal wavefront sensor along with an illustration of the preliminary experimental results.

## 4.2 Important devices used in the experimental arrangements

The different experimental arrangements used in this thesis work comprise some important or specialized devices. Here we first provide a brief description of some such important devices employed.

### 4.2.1 Liquid crystal spatial light modulator

Spatial light modulator (SLM) is the most crucial component in the experimental implementation of the holographic modal wavefront sensor. As the name suggests, SLMs are devices that have the ability to spatially modulate the amplitude and phase of a light beam. Though there are a number of SLMs such as Liquid crystal SLMs, Digital micromirror devices, Acoustic-optic SLMs, Magneto-optic SLMs, Deformable mirror, etc., the chapter includes discussions only on Liquid crystal SLMs (LCSLM) and Digital micromirror devices (DMD), as these two types of SLMs are used in our experiments.

We begin with LCSLM that comprises liquid crystal cells or pixels arranged in two a dimensional array. The application of a suitable electrical or optical signal over the pixels can modulate the transmittance property of each pixel of such LC-SLMs. Thus, depending on the type of the control signal the LCSLMs can be called as electrically addressed LCSLM or optically addressed LCSLM. The electrically addressed LCSLM being easy to integrate with a computer interface and easy to operate, are used in our experimental arrangements.

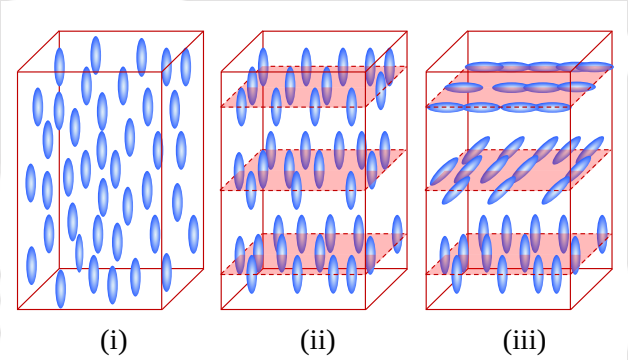


**Figure 4.1:** Molecular distribution of (i) nematic, (ii) Smectic and (iii) cholestric LC molecules.

The liquid crystals (LC), the main constituent of the LCSLM pixels exist in an intermediate phase between isotropic liquids and crystalline solids. They behave like a liquid but have a positional or orientational order or both, i.e. showing crystalline behaviour. The LC molecules are of oval shape with a long axis called director. The direction of the director define the orientational state of the LC molecules. The LCs are primarily classified as thermotropic, lyotropic and polymeric, among which the thermotropic LCs are of our interest as they are used in light modulators [52]. Further the thermotropic liquid crystal exists in three major phases - nematic, smectic

and cholestric, as depicted in Fig. 4.1. The nematic phase has no positional ordering but has an orientational ordering of the molecules (shown in Fig. 4.1(i)), the smectic phase has both positional as well as orientational ordering of the molecules (shown in Fig. 4.1(ii)) whereas the cholestric phase apart from having both positional and orientational ordering, has a layer to layer rotation of the molecules (shown in Fig. 4.1(iii)). A special type of the smectic phase of liquid crystal called ferroelectric phase can also be prepared [40]. The commercially available LCSLMs mostly use the nematic or the ferroelectric phase. Below we discuss about LCSLMs using nematic or ferroelectric phases of liquid crystals.

**Nematic liquid crystal spatial light modulator**

The nematic LCSLM (NLCSLM) comprises an array of pixels containing nematic LC molecules [40, 52]. The nematic LC molecules are randomly distributed throughout the volume of the liquid crystal cell, but their long axes align along a particular direction as stated above. An important characteristic of the nematic LC molecules is their tendency to remain aligned with their nearby molecules. This tendency of the molecules leads to the design of twisted nematic LC cells used in NLCSLMs. This is made possible by placing the nematic LC molecules in a volume between two alignment layers comprising small scratches coated on the glass plates of the opposite boundary walls of the cell. If the alignment layers are so oriented that the direction of the scratches are orthogonal to each other, the molecules at the close proximity of the alignment layers will align themselves along the direction of the scratches and those in between will have intermediate orientations thereby forming a twist (Fig. 4.2(i)). If a linearly polarized light with its polarization parallel to the scratches of the front surface propagates through the twisted nematic LC cell, for a certain cell width it can experience a polarization rotation by $90^o$, i.e. it will follow the molecular twist to result in a polarization rotation of $90^o$. On the application of an AC electric field of sufficient strength through the LC cell with the help of two transparent electrodes superposed with the alignment layers, electric dipole is induced in the LC molecules along the molecular axes. The induced dipole moment is along a direction opposite to that of the electric field. Due to the induced dipole moment, apart from the molecules that are close to the alignment layers, the molecules align themselves with their long axes parallel to the direction of the applied electric field (Fig. 4.2(ii)). Here AC electric field is applied to avoid any permanent polarization

of the molecules. In the presence of an applied electric field, the propagating linearly polarized light will not face any polarization rotation. On placing a polarizer and an analyzer, with their polarization axes along the direction of the scratches on the two alignment layers of the LC cell, light can be made to transmit through the cell only when there is no applied electric field. Thus the transmittance property of each pixel of a nematic LCSLM can be controlled with the help of an alternating electric field. The electrical control of the transmittance property of an LC cell can be generalized for the entire 2D array of LC cells. The computer interface facilitates using a binary image pattern comprising the same number of image pixels as the size if the LC pixels of the LCLSM to control the LCSLM transmittance. Thus binary hologram as described in previous chapter which for a computer is nothing but a binary image can be implemented using the LCSLM.

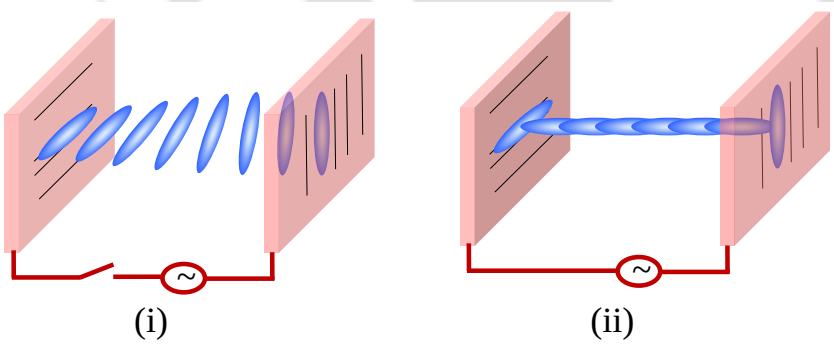


**Figure 4.2:** Representation of the molecular reorientation in a twisted nematic LC cell (i) in the absence and (ii) presence of an AC electric field.

In our experiments we used two types of NLCSLMs, namely, LC-R 720 and LC-R- 1080, both from Holoeye, Germany [53]. However, the NLCSLMs used in the experiments may not necessarily have the exact alignment as shown in the figure above. The LC-R 720 NLCSLM has a display resolution of 1280×768 pixels with a fill factor of 92% and a pixel pitch of $20\mu m$. It has an achievable image frame rate of 180 Hz and can display 8 bit gray levels. On the other hand the LC-R- 1080 NLCSLM has a screen resolution of 1920×1200 pixels with a fill factor of 90% and a pixel pitch of $8.1\mu m$. It has an image frame rate of 60 Hz and can display 8 bit gray levels. Both the NLCSLMs drivers operate at a DC voltage of 24 volt and can be plugged directly to a computer graphics card via a DVI interface.

### Ferroelectric liquid crystal spatial light modulator

The ferroelectric liquid crystal spatial light modulators (FLCSLM) comprise cells filled with liquid crystal molecules that are in chiral smectic phase commonly known as smectic C* phase [40, 52]. The LC molecules of smectic phase, as stated already, are arranged in parallel layers with their long axes aligned in a direction normal to the layer plane when its called smectic A phase or tilt at some angle with the normal when it is called smectic C phase. The LC molecules of smectic C* phase are chiral (i.e. they do not have mirror symmetry) and their tilt angle form a helical structure from layer to layer. The ferroelectric LC cells have a permanent dipole moment and the long axis of the molecules tilt at an angle (say $\theta$) with the layer normal (shown in Fig. 4.3). As shown in the figure the direction of the molecular tilt switch to the other direction (i.e. tilt angle of $-\theta$) on the application of a DC electric field. Thus the molecules are bistable with two stable orientations having tilt angle $\theta$ and $-\theta$ which can be termed as on and off state. The molecules retain the current state after the removal of the electric field and can be changed on application of an appropriate electric field. A properly designed ferroelectric LC cell can be made to behave like a half wave plate for an incident beam of light. The optic axis of such a retarder is dependent on the long molecular axis which can be switched between two stable orientations by applying the DC electric field. Therefore likewise the NLCSLM, the FLCSLM in conjunction with a polarizer and an analyzer can modulate the transmittance properties of a light beam and thus can display a binary hologram.

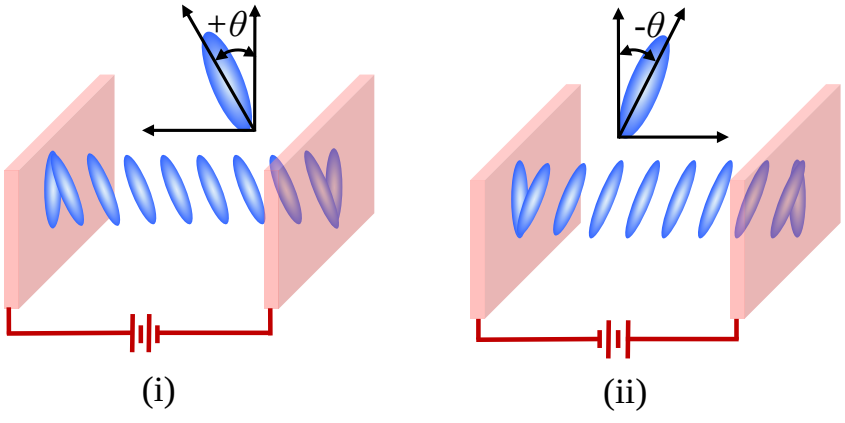


**Figure 4.3:** Representation of the molecular reorientation in a ferroelectric LC cell in the presence of DC electric field from (i) left to right and (ii) right to left.

To perform our experiments we used a FLCSLM, SXGA-R3, from Forth Dimen-

sion Display, UK [54]. This particular FLCSLM has a screen resolution of 1280×1024 pixels with a pixel pitch of 13.62 $\mu$m. It has a panel area of 20.68 mm×18.87 mm with an active area of 17.43 mm×13.95 mm. The SXGA-R3 can display 24 bit native color depth with 8 bits each for red, green and blue color. It has a maximum refresh rate of 85 Hz for 24 bit color images and a frame rate of 2040 Hz (84×24) for binary images.

### 4.2.2 Digital micromirror device

Digital micromirror device (DMD) is another type of spatial light modulator that is used during the experimental implementation of the holographic modal wavefront sensor. The DMD is an optical micro-electro-mechanical-system that comprises a highly reflective two dimensional array of aluminium micromirrors [55]. All individual micromirrors constituting the DMD are mounted on an individual electro-mechanical stage imparting two stable states to the micromirrors. In most of the DMDs the two states of the micromirrors are a tilt of $+12^o$ and $-12^o$ with respect to the diagonal direction of the micromirrors. The electro-mechanical stage and the micromirror mounted on it form a pixel of the DMD. The two stable positions of the micromirrors determine the deflection direction of the light incident on it. By convention the positive ($+12^o$) state is considered to deflect the light in the desired direction and is referred to as the on state while the negative ($-12^o$) state is considered to deflect the light away from the desired direction and is referred to as the off state. Therefore the beam is least affected by the interior of the DMD pixel, unlike the LCSLM pixels which will be taken up later in the chapter. We used a DMD of DLP9000 family from Texas Instruments [56]. The complete system comes in the form of a DLP LightCrafter 9000 Module that comprises two subsystems - the DLPC900 Board and the DMD Board. The DLP9000 has a resolution of 2560×1600 (WQXGA) pixels with a micromirror pitch of 7.56 $\mu m$ and a diagonal length of the display equal to 0.9 inch. The diffraction efficiency and the fill factor of the micromirror array of the DMD are 86% and 92%, respectively, while the reflectivity of the mirror surface is 88%. The present DMD offers four mode of operation - video mode, video pattern mode, pre-stored pattern mode and pattern on-the-fly mode. The video rate in case of video mode operation depends on the video cable, i.e. an HDMI cable allows a video rate of 30 Hz while a display port allows a video rate of 60 Hz. The pattern rate in case of the video pattern mode operation can rise

from 247 Hz for a bit depth of 8 to 2880 Hz for a bit depth of 1, whereas in case of the pre-stored pattern mode and pattern on-the-fly mode operation the pattern rate can rise from 247 Hz for a bit depth of 8 to 9523 Hz for a bit depth of 1. Thus the DMD facilitates implementation of binary amplitude hologram at a refresh rate up to about 9.5 kHz. The response time of the micro mirror is of the order of few tens of micro seconds enabling high speed full frame display.

### 4.2.3 Cameras

The charge coupled device (CCD) sensors and complementary metal oxide semiconductor (CMOS) sensors are two important sensors used in the cameras for a majority of the imaging applications. Both the CCD and CMOS are semiconductor devices that use photodiodes to covert light to electrical signal but differ in terms of manufacturing and signal readout process. The CCD sensor comprises an array of capacitors attached to the photodiodes that collect charges (proportional to the intensity of the light incident on it) in the form of electrons [57]. The charges from each column of capacitors are transferred to their nearby column of capacitors and the process is repeated to finally dump the charges into an amplifier. This scheme of charge transfer is called the bucket-brigade style of data transfer. A CMOS sensor comprises an array of photodiodes each attached to a CMOS transistor [58]. Here the array of CMOS transistors also act as a switch to access the signal from each pixel directly as well as sequentially with a speed higher than that of the CCD sensor. The CMOS sensors are available at low cost and they consume less power for its operation. Moreover, their logical circuitry can be superposed during the manufacturing process itself. On the other hand CCD sensors provide images of better quality and are more light sensitive that of the CMOS sensors.

During our experiments we used a USB 3.0 CMOS camera from Thorlab bearing the model number DCC3420M [59]. The camera has a resolution of 1280×1024 pixels with a pixel pitch of 5.3 $\mu$m. It runs through a USB 3.0 cable communication interface and provide a maximum frame rate of 60 Hz. The camera also has the facility of selecting the area of interest (AOI) which enables high speed operation. The camera can be synchronized with an external device using a trigger signal or can operate in the free-run mode.

A high speed camera link CMOS camera (model number: A504K) [60] from Basler was also used in our experimental arrangements. The resolution of the camera

is 1280×1024 pixels and has a pixel pitch of 12 $\mu$m. The camera can operate with a maximum frame rate of 500 fps (frames per second) using its full frame and the frame rate can be increased further by decreasing the number of active rows. This camera can also run in trigger mode and free run mode. The Basler A504K CMOS camera was interfaced with a PC (personal computer) using a cameralink frame grabber card. The frame grabber card (model number PCIe-1429) used is from National Instruments. The frame grabber card facilitates direct access to the data and camera features using the National Instruments Driver Software (NI-IMAQ) running in the PC.

### 4.2.4 Lasers

One of the other important components used in our experiments is the Laser. We obtain a monochromatic, spatially coherent and collimated light beam acting as the incident beam for the binary hologram from the laser source. In our work we have used two different lasers mentioned below

We used a diode-pumped solid-state (DPSS) laser from Spectra-Physics bearing part number Excelsior-532-200-CDRH [61]. It is a single mode ($TEM_{00}$) green laser with a wavelength of 532 nm, an output power of 200 mW and shock tolerance up to 25 G. The laser has a beam diameter (1/e) of 0.32±0.02 mm, beam divergence of less than 2.5 milliradian and a beam quality of $M^2 < 1.1$. It operates at a voltage of 5 volt DC and takes less than 5 minutes to warm up to reach the specified power stability. It has an operating temperature range from $10^o$ to $40^o$C for a proper operation.

We also used a Helium-Neon (He-Ne) laser from Melles Griot bearing part number 05-LHR-991 [62]. It is also a single mode laser ($TEM_{00}$) with an output power of 10 mW, emitting a beam with a wavelength of 632.8 nm. The laser with a beam quality of $M^2 < 1.05$, operates at an input voltage of 2.640 volt DC and a current of 6.5 mA. The laser has a beam diameter (1/e) of 0.65 mm, a beam divergence of 1.64 miliradian and a shock tolerance up to 25 G. It operates properly within the temperature range of $-20^o$ to $40^o$C.

The modal wavefront sensors discussed in chapter 2 and chapter 3 are based on detecting the intensity of the focused light beam by a point detector placed at the center of the focal spot. In the case of the holographic modal wavefront sensor the biased orders are in fact beams which are diffracted by the hologram. In this

work we intend to use LCSLM based binary holograms to implement such modal wavefront sensor. Thus for proper detection of central intensity of the biased orders the diffracted beams should maintain a stable deflection angle. However, we noticed that angle made by the diffracted beams is affected by a thermal effect inherent to the LCSLM device [63, 64]. Below we provide a discussion on our investigation.

## 4.3 Thermally induced beam deflection by a liquid crystal spatial light modulator

It has been observed by various researchers that liquid crystal molecules or LCSLMs have temperature dependent properties. The thermotropic liquid crystals, the key component of an LCSLM, are observed to be highly sensitive to any change in temperature[52]. In fact the property of the liquid crystal molecules of being highly sensitive towards any temperature changes can be used to develop temperature sensors [65]. The dependence of the refractive index of the liquid crystals on the temperature gradient imparted by the intensity of an incident Gaussian laser beam, is a direct consequence of self focusing effect observed when the beam propagates through a nematic liquid crystal [66]. This leads to the generation of thermal lenses in nematic liquid crystals through suitable orientational adjustment of the polarization plane of the probe laser beam [67]. Even thermal optical nonlinearities were also observed in surface stabilized ferroelectric liquid crystal cell [68].

Our investigation on the beam deflection is based on a number of experiments performed using both a nematic and a ferroelectric LCSLM based setup.

### 4.3.1 Beam deflection due to both the nematic and ferroelectric Liquid Crystal Spatial Light Modulators

The experimental setup to investigate the beam deflection caused by the NLCSLM and the FLCLM is shown in Fig. 4.4(i). The setup enables to record the beam deflection due to each of the NLCSLM and FLCSLM without the need to disturb the setup. This is made possible since an LCSLM in a prolonged power off mode acts as a simple plane mirror for a given incident beam. During the investigation one of the LCSLMs is kept active, displaying a binary amplitude hologram while the other is kept in the power off state. However, it is to be noted that the later

LCSLM should already be in the power off state for a sufficiently long duration. In order to hold the LCSLM panel firmly on the vibration isolation table or the optical bench used, it requires a rigid mount as seen in Fig. 4.4 (ii). The mount could be made of a nonconducting or a conducting material. A conducting mount can quickly dissipate the heat that may accumulate in the LCSLM panel whereas in the case of the nonconducting mount the heat dissipation will be slow.

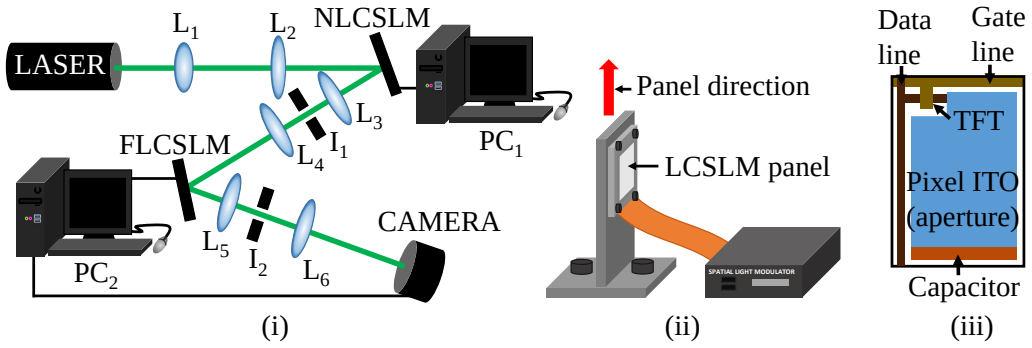


**Figure 4.4:** Schematic of (i) the experimental arrangement to study the beam movement due to the NLCSLM and the FLCSLM, (ii) a rigid mount holding the LCSLM panel and (iii) the arrangement of the electronic parts inside an LC cell.

As shown in Fig. 4.4(i), a laser beam (wavelength = 532 nm) after being expanded and collimated by the lens combination $L_1$ and $L_2$ (power of the beam is $\approx 0.2\mu W$), is allowed to fall on a reflective NLCSLM. The reflected beam from the NLCSLM is then allowed to pass through a 4-f relay lens system $L_3$ and $L_4$ to fall on a reflective FLCSLM. An iris diaphragm $I_1$, located at the focus of $L_3$, is used to isolate either the zero order beam or the +1 order beam from the unwanted orders generated due to the binary hologram displayed on the NLCSLM panel. The beam reflected by the FLCSLM is then focused on a USB CMOS camera with the help of the lens combination $L_5$ and $L_6$. Another iris diaphragm $I_2$ is placed at the focus of $L_5$ to isolate the zero order or the required diffraction order from the other unwanted orders due to the binary hologram displayed on the FLCSLM. The beam position is recorded by the USB CMOS camera with the help of a computer interface. The entire experimental arrangement is placed on a vibration isolation stage so as to minimize the effect of mechanical vibrations on the experimental data.

### Experiment

The observations are carried out with each of the LCSLMs mounted once on a nonconducting slab and then on a conducting slab. The X and Y coordinates of the beams in the camera plane of both the zero order beam and the +1 order beam are recorded. A computer program enables recording of the beam positions at an interval of one minute for a net duration of 8 hours. First both the NLCSLM and the FLCSLM are mounted on a nonconducting slab and are kept in prolonged power off state. Then the NLCSLM is powered on with a binary hologram in the form of a grating pattern written on its display panel and the computer program is operated for 180 minutes. The NLCSLM is then powered off and the programme is continued for another 5 hours to record the position of the zero order beam only. To be noted that throughout the investigation the FLCSLM is kept in the power off state. The same procedure is then carried out for the FLCSLM with the NLCSLM in the power off state. The two LCSLMs are then mounted on conducting slabs and both the two procedures are repeated.

The X and Y coordinate data as recorded by the camera are converted to beam deflection angle in the respective LCSLM plane.

### Observations

Figure 4.5 shows the plots of the angular positions of the zero order beam along the (i) X axis and (ii) the Y axis, due to the NLCSLM when the FLCSLM is kept in the power off state. The plots AC and CE correspond to the power on and power

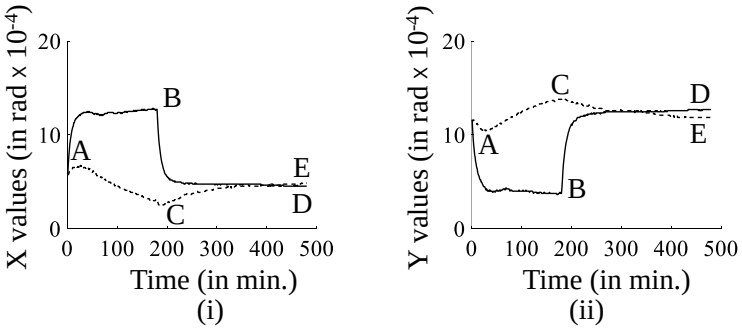


**Figure 4.5:** Plots of orientation of the zero order beam due to the NLCSLM in the respective LCSLM plane when the two LCSLMs are mounted on conducting and nonconducting slabs with the angles along (i) the X axis and (ii) the Y axis.

off state, respectively, of the NLCSLM mounted on a nonconducting slab while the

plots AB and BD correspond to the power on and power off state, respectively, of the NLCSLM mounted on a conducting slab. It is observed that as a result of the combined effect during power on and off state of the NLCSLM in each of two cases of mounting, the locus of the zero order beam nearly constitutes a close loop. The beam moves in a particular direction when the NLCSLM is in the power on state and then it tends to return to its initial position when the LCSLM is powered off. It is further observed that the movement of the beam is much slower during the power off state than that during the power on state. It is noticed in Figs. 4.5 (i) and (ii) that overall movement of the zero order beam is more when the NLCSLM is mounted on conducting slab relative to when it is mounted on a nonconducting slab. However, in the case of the nonconducting slab the beam keeps moving for the entire duration of the power on period, while in the case of the conducting slab the beam quickly settles down to a certain angular position and remains steady for the rest of the period. Similar behaviour is also observed for the two cases of mounting, during the power off state of the NLCSLM.

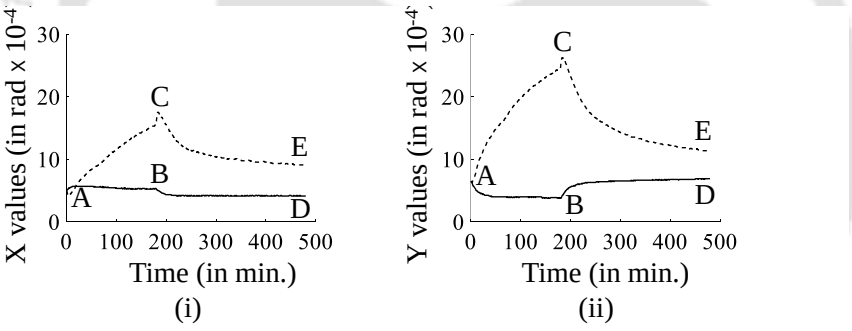


**Figure 4.6:** Plots of orientation of the zero order beam due to the FLCSLM in the respective LCSLM plane when the two LCSLMs are mounted on conducting and nonconducting slabs with the angles along (i) the X axis and (ii) the Y axis.

Similarly, Fig. 4.6 shows the angular positions of the zero order beam along (i) the X axis and (ii) Y axis, caused due to the FLCSLM, when both the LCSLMs are mounted on nonconducting and conducting slabs. In this case also the beam positions are recorded at regular intervals of time. The plots indicate that during the power on state of the FLCSLM while both the LCSLMs are mounted on a nonconducting slab, the beam moves quickly away from the initial position while during the power off state it appears to come back slowly to the initial position. However, when both the LCSLMs are mounted on conducting slabs, the beam movement during both the power on and power off states is significantly less.

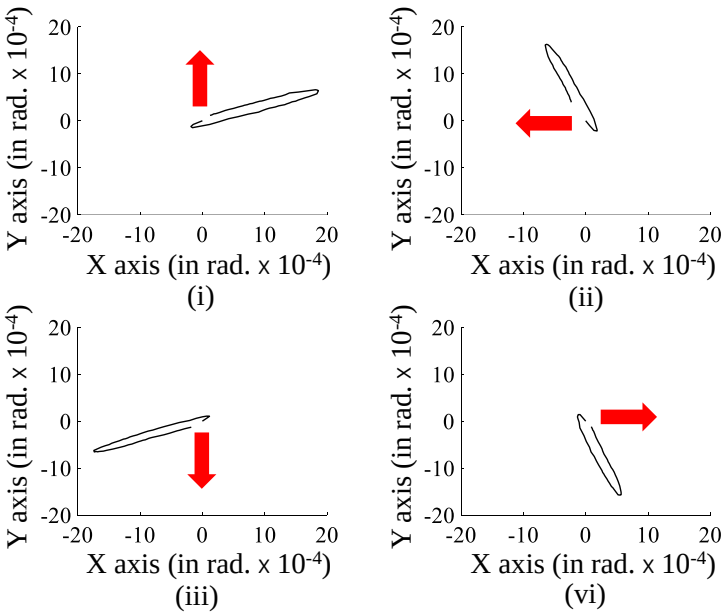


**Figure 4.7:** Angular positions of the zero order beam during the power on and power off state of the FLCSLM forming close loops corresponding to different orientations of the LCSLM panel (i→iv) as indicated by the arrow head.

The beam positions are also recorded during the power on/off states of the LCSLM by keeping the mounting slabs at four different orientations. Figures 4.7 (i→iv) show the near close loops formed by the locus of the zero order beam for four different orientations of the FLCSLM mounted on a nonconducting slab with the panel orientations indicated by the arrow head. It is noticed that the pattern of the beam movement rotates with the rotation of the mounting slab. Similar effect on the beam movement due to different orientations of the panel is also observed in case of NLCSLM.

The results shown so far only correspond to the zero order beam, although during power on state of the LCSLM one may also record the +1 order beam movement. Figures 4.8 (i) and (ii) show the +1 order beam movements during the power on state of (i) the NLCSLM and (ii) the FLCSLM along with the plots of the respective zero order beam positions. It can be noticed that the +1 order beam follows a trajectory very similar to the zero order beam trajectory. Hence, the cause of the +1 order beam movement will be same as that of the zero order beam movement and there appears no reason to investigate the cause of the +1 order beam movement separately. Further, we have also investigated on any possible broadening of the beam along with the beam movement. However, we could not find any noticeable

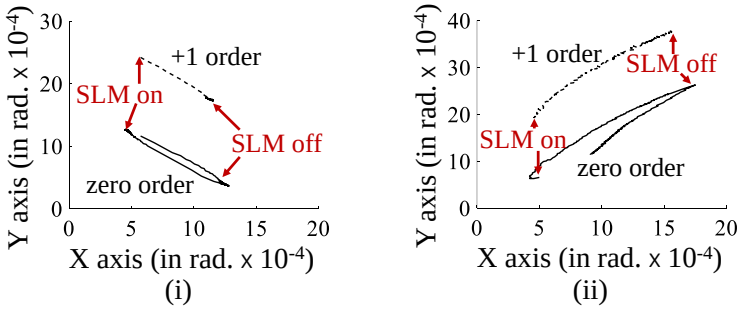


**Figure 4.8:** Angular positions of the zero order beam during power on/off states and +1 order beam during power on state due to (i) an NLCSLM mounted on a conducting slab and (ii) an FLCSLM mounted on a nonconducting slab.

change in the beam diameter.

### 4.3.2 Causal inference

The experiment above shows that the beam movement has a direct relation with the power on/off instants of the respective LCSLM. Further, the locus of the beam in the camera plane rotates with the rotation of the LCSLM panel. This establishes that the beam movement has some positional dependence on certain physical component inside the LCSLM panel. It is also seen that the beam movement gets reduced when the LCSLM is mounted on a conducting slab relative to that when it is mounted on a nonconducting slab. Thus the rise in temperature due to reduced heat dissipation from the panel (which is when the panel is mounted on a nonconducting slab) is a possible cause of the beam movement. A typical arrangement of electronic parts inside an LC cell, as indicated in Fig. 4.4 (iii), shows that current flow inside a cell is not symmetric with respect to the center of the LC cell and it predominantly flows through one side of the LC cell cross section (orientated perpendicular to the beam propagation direction). To be noted that the LCSLM panel shown in Fig. 4.4 (ii) comprises of a two dimensional matrix of such LC cells shown in Fig. 4.4 (iii). Therefore the beam movement can be due to uneven heating of the material inside the LC cell resulting in the maximum temperature near the current flow and gradually decreasing temperature towards the other side of the LC cell cross section. Moreover, the presence of a thin film transistor (TFT) at one corner of the LC cell (as shown in Fig. 4.4 (iii)) further contributes to the unevenness in the temperature distribution due to its inherent self heating process [69, 70]. It has been observed

that an electric field across a nematic liquid crystal lead to change in temperature due to electric heating within the liquid crystal[71]. This change in temperature is given by,

$$\Delta T(t) = \Delta\overline{T}\left[1 - exp\left(-\frac{t}{\tau_1}\right)\right] \tag{4.1}$$

where, $\Delta\overline{T}$ is the total rise in temperature of the nematic liquid crystal slab, $t$ is the time and $\tau_1$ is the characteristic time constant determining the transition of the stationary regime. This change in temperature, in turn changes the average refractive index of the liquid crystals. There are experimental evidences of decrease in the average refractive index (n) of both the nematic and the ferroelectric liquid crystals with a rise in temperature within them [72, 73] in a linear fashion.

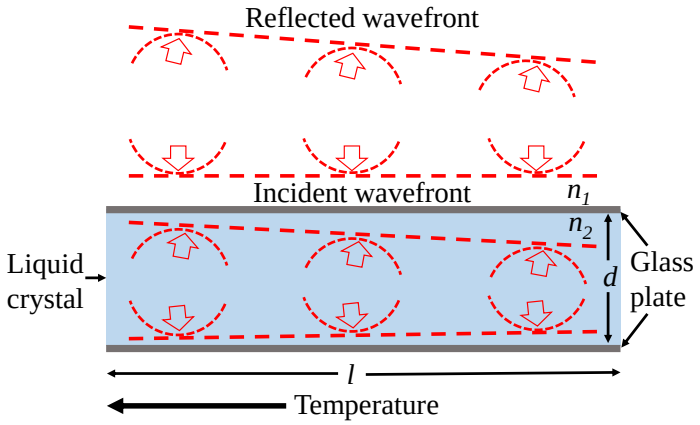


**Figure 4.9:** Change in the direction of the reflected beam due to the temperature gradient inside the LC cell along the direction shown.

$$n(T) = n_0 - BT \tag{4.2}$$

where $n_0$ and B are constants. Thus it may be expected that the temperature gradient inside the LC cell due to the current flow on one side leads to a refractive index gradient along the cell cross section. While the LCSLM is in power on state and especially mounted on a nonconducting slab the gradient increases rapidly with time. If the LCSLM is mounted on a conducting slab, due to heat dissipation the temperature gradient quickly stabilizes at a certain value. When the LCSLM is powered off, the temperature gradient disappears more rapidly for the conducting slab and less rapidly for the nonconducting slab till it attains the initial configuration.

**Table 4.1:** Table of the fitting constants.

| **Region** | **Fitting constants** | | | | | | | |
|---|---|---|---|---|---|---|---|---|
| | **NLCSLM** | | | | **FLCSLM** | | | |
| | $\alpha$ | $\beta$ | $\gamma$ | $\delta$ | $\alpha$ | $\beta$ | $\gamma$ | $\delta$ |
| (I) | 10.3 | 5.2 | 1 | 130 | 5.8 | 22 | 1 | 95 |
| (II) | 9 | 2.5 | -1 | 130 | -6 | 17 | -1 | 83 |
| (III) | -6.2 | 10 | -1 | 10 | 0.8 | 2.9 | -1 | 17 |
| (IV) | -2.5 | 15 | 1 | 13 | 2.5 | 4.3 | 1 | 24 |

To be noted that the temperature dynamics of a nematic LC cell subjected to an applied electric field for different surrounding medium have also been demonstrated experimentally [71].

Let us consider the liquid crystal volume inside an LC cell of thickness $d$ and length $l$ as shown in Fig. 4.9. The refractive indices of air and the LC material are taken as $n_1$ and $n_2$, respectively. We also consider that the electric heating produces a positive temperature gradient along the direction shown by the arrow head such that the net temperature change on one end is $\Delta T$ while there is no temperature change on the other end. For a beam incident normally on the LC cell, we can draw the wavefronts along the beam path using Huygen's principle of secondary wavelets. As indicated by Eq. 4.2, the change in temperature $\Delta T$ leads to a change in refractive index of the LC material by $\Delta n_2 = -B\Delta T$. Consequently, the wavefront gets tilted when it travels inside the LC cell as different parts of it travel with different phase velocities. It can be shown that the reflected wavefront undergoes a change in direction by

$$\Delta\theta_{LC} \approx \frac{-2dB\Delta T}{n_1 l} \tag{4.3}$$

Thus the orientation of the beam reflected by the LC cell changes as the temperature gradient increases. The experimental data corresponding to Figs. 4.5 and 4.6 can be fitted by a slight modification of the Eq. 4.1. The modified equation is written as,

$$\Delta T(t) = \alpha + \beta\left[1 - \gamma exp\left(-\frac{t}{\delta}\right)\right] \tag{4.4}$$

where $\alpha, \beta, \gamma, \delta$ are fitting constants whose values are represented in Table 4.1. Thus, we use Eqs. 4.4 and 4.3 to do the curve fitting of the experimental data

corresponding to Figs. 4.5 and 4.6. The data is divided into two halves, one half corresponding to the power on state and the other half corresponding to the power off state. The fitted curves along with the experimental data in case of NLCSLM and FLCSLM are seen in Figs. 4.10 (i) and (ii), respectively. A reasonably good fitting of the curve provides further evidence regarding the correctness of the cause behind the beam movement.

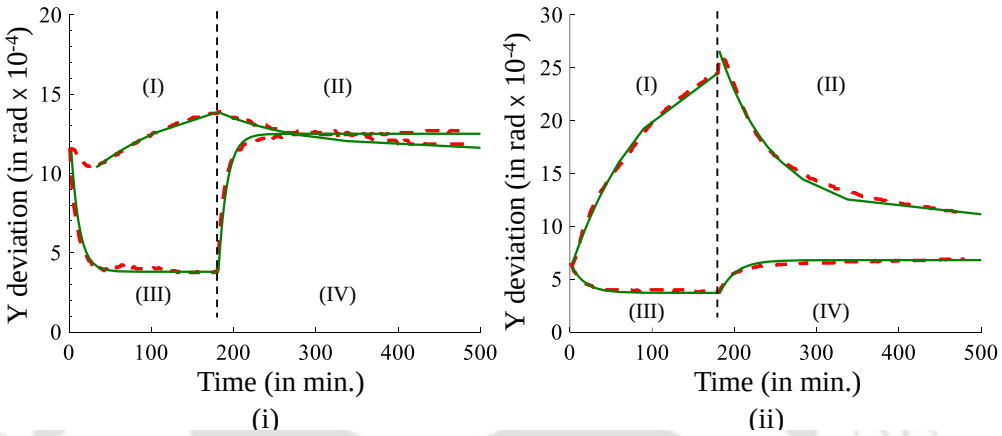


**Figure 4.10:** Experimental plot and the curve fitting of the angular positions along the Y axis of the zero order beam during the power on/off modes of (i) the NLCSLM, and (ii) the FLCSLM.

Figures. 4.5 and 4.6 show that immediately after the LCSLM, mounted on a nonconducting slab, is powered on, the beam traces a "U" turn before proceeding further away from the initial position of the beam. The possible cause for this behavior can be the temperature gradient inside the glass layer above the LC volume. In obtaining the expression for the beam angle in Eq. 4.3 we have taken only the influence of the LC materials on the beam direction into account ignoring the influence of the glass layer. It is known that for glass the change in refractive index for a given increase in temperature has a positive gradient [74] in contrast to LC material which has a negative gradient. Thus the corresponding beam movement will also be in the opposite direction as well, as the temperature gradient increases. The combined effect of the temperature gradients inside the LC cell and the glass layer therefore leads to a "U" turn of the beam trajectory just after the LCSLM is powered on.

We however, do not completely nullify the effect of the common electrode of the LCSLM made of indium tin oxide (ITO) as yet another probable cause of the beam deflection. Current flow in the ITO sheet and ITO being thermally active

would result in micro-ohm resistance down the front electrode, thus a change in temperature ($\Delta T$) might also contribute to beam deflections.

### 4.3.3 Role of the LCSLM mounting material

It is observed that both the diffracted and undiffracted beams emerging from an LCSLM exhibit a certain movement of the beam cross section. Experimental results show that the trajectory of the beam depends on the power on/off status of the LCSLM as the path during power on state is somewhat opposite to the path during power off state. The path followed by the +1 order beam is very similar to the corresponding zero order beam. Thus it can be concluded that the cause behind the movement of both the beams is the same. Further, if the beam trajectories are recorded with different orientation of the LCSLM panel, the near close loop formed by the trajectory of the zero order beam also changes its orientation accordingly. The above observations suggest that the beam movement is non-mechanical in nature or is not caused by the mechanical movement of the experimental arrangement. Rather the beam movement is associated with the current flow status and the location of a certain physical component inside the LC cell. However, the beam movement is more prominent for the entire power on/off duration if the LCSLM is mounted on a nonconducting slab and the same gets reduced if the device is mounted on a conducting slab. Thus the beam movement is associated with the rate of heat dissipation from the LCSLM panel such that an appreciable movement is observed when the heat dissipation from the LCSLM panel is at its lowest. These observations lead us to believe that the flow of current inside the LC cell during the power on state of the device creates a temperature gradient whose relative magnitude depends on whether the LCSLM panel is mounted on a conducting or a nonconducting slab. The arrangement of electrical connection inside a typical LC cell reveals that the flow of current inside an LC cell is not symmetric with respect to the center of the LC cell. The temperature gradient in the LC cell leads to a change in refractive index of the LC material resulting in a change in the orientation of the reflected beam. As the light beam also has to pass through the glass layer sitting at the top of the volume of LC molecules, the beam movement is also influenced by the temperature gradient formed inside the glass layer. A reasonably good agreement between experimental data and the fitted curves indicate the correctness of our model to explain the beam movement. From the analysis of the experimental results, it can be concluded that in

order to minimize the movement of the beam diffracted by an LCSLM, the LCSLM panel has to be mounted on a slab with the best heat dissipating capability or the heat conductivity. Thus, the conducting slab acts as a heatsink which should be such that it covers the entire back side of the LCSLM panel in a uniform manner. Therefore in all the experimental implementations throughout the thesis aluminium plates are used as a mount for the LCSLM panel since aluminium has a relatively good thermal conductivity.

## 4.4 Implementation of the holographic modal wavefront sensor

In this section we demonstrate the experimental implementation of the holographic modal wavefront sensor through a proof of principle setup. We use two LCSLMs to act as two separate binary holograms. The first binary hologram facilitates generation of a beam with user defined phase profile which is incident on the other binary hologram which in turn generates the bias orders. The experimental arrangement for this implementation is shown in Fig. 4.11.

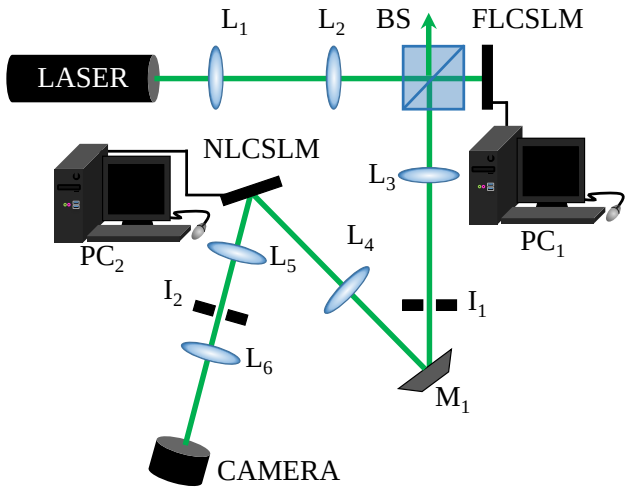


**Figure 4.11:** Experimental arrangement for the implementation of the holographic modal wavefront sensor.

As shown in the figure the laser beam from a He-Ne laser ($\lambda = 632nm$) is first expanded and then collimated by a lens system $L_1$ and $L_2$. The collimated beam (with a plane wavefront) then falls on a 50% beam splitter (BS). The beam transmitted through the BS falls on a reflective FLCSLM panel placed normal to the

incident beam. A binary amplitude hologram is written on the FLCSLM panel with the help of a computer ($PC_1$) interface. The beam reflected from the FLCSLM panel is then reflected by the BS to pass through a $4f$ relay lens system, $L_3$ and $L_4$ and an iris diaphragm $I_1$. The binary hologram written on the FLCSLM panel gives rise to diffraction orders which constitute the reflected beam. Among the various diffraction orders the +1 order is of our interest which carries a user defined phase profile as per the property of the hologram. Hence all other orders are blocked by $I_1$ and only the +1 order beam falls on an NLCSLM panel after being reflected by mirror $M_1$ and transmitted through $L_4$. $M_1$ is used to confine the experimental arrangement within the optical table. A binary multiplex amplitude hologram is written on the reflective NLCSLM panel which give rise to multiple +1 diffraction orders acting as the bias orders. The reflected beam from the NLCSLM panel is focused by lens $L_5$ on another iris diaphragm $I_2$ that allows only the +1 orders to pass through it. The +1 orders are then focused by lens $L_6$ on a CMOS camera. The NLCSLM in combination with the CMOS camera forms the Holographic modal wavefront sensor, HMWFS, unit. The focal spots arrangement detected by the CMOS camera is shown in Fig. 4.12 (i).

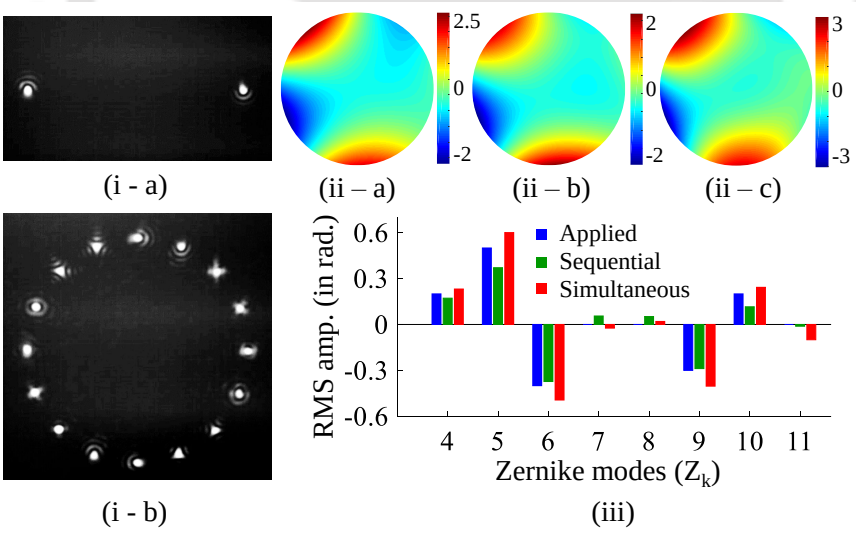


**Figure 4.12:** (i) The focal spot arrangement in the camera frame for (a) sequential and (b) simultaneous measurement; (ii) false color representation of the (a) input phase, (b) sequentially detected phase and (c) simultaneously detected phase and (iii) bar plot representation of the RMS amplitude of the applied and detected Zernike modes.

A phase profile $\phi_2(x, y) = 0.2Z_4 + 0.5Z_5 - 0.4Z_6 - 0.3Z_9 + 0.2Z_{10}$ (same as chapter 3) comprising a random combination of eight different Zernike modes is generated us-

ing the FLCSLM. The magnitude of all the eight Zernike modes are measured using the HMWS employing both a sequential and a simultaneous measurement scheme. For sequential measurement a binary duplex amplitude hologram (interferogram due to one reference beam and two object beams) is displayed on the NLCSLM and the hologram is updated for different sensor mode each time we measure a particular Zernike mode. For simultaneous measurement a binary multiplex amplitude hologram (interferogram due to one reference beam and 16 object beams) is displayed on the NLCSLM. Both the sequential and simultaneous measurement techniques are explained is details in Chapter 2 and Chapter 3. The focal spot arrangements using both the sequential and simultaneous measurement schemes captured by the camera is shown in Figs. 4.12 (i-a) and 4.12 (i-b), respectively. Figure 4.12 (ii-a) is the false color representation of the input phase (i.e. phase comprising a random combination of eight Zernike modes). Figures 4.12 (ii-b) and 4.12 (ii-c) are the false color representation of the detected phase by sequential and simultaneous measurement schemes, respectively. While Fig. 4.12 (iii) is a bar diagram representation of the RMS amplitude of the Zernike modes in the input phase profile, and the corresponding RMS amplitudes as detected through sequential and simultaneous measurements. The blue bars represent the applied RMS amplitudes, the green bars represents the sequentially detected RMS amplitudes while the red bars represent the simultaneously detected RMS amplitudes of the Zernike modes. It is observed that the RMS amplitude of the Zernike modes present in the incident beam could be measured by the holographic modal wavefront sensor to a reasonable accuracy both through sequential and simultaneous measurements. Small amount of disagreements are attributed to the presence of inter-modal cross talk and low linearity range in conjunction with experimental imperfections.

## 4.5 Conclusion

In this chapter we have discussed about a few essential devices to be used in different experimental setups throughout this thesis. We have discussed about two types of liquid crystal spatial light modulators (nematic and ferroelectric type), the Digital micromirror device, two types of CMOS cameras (Thorlab USB camera and Basler cameralink camera) and two types of laser (He-Ne-laser abd DPSS laser) used in our experiments. We then discussed about an intrinsic issue of a liquid crystal spatial light modulator that arise due to the electric heating of the liquid crystal cells

comprising the liquid crystal spatial light modulator. We have discussed how this heating effect gives rise to beam deflection from the ideal orientation of the beam, which could add inaccuracy or inconsistency in the result of a holographic modal wavefront sensor. We have put forward a way to minimize such beam fluctuations. At the end of the chapter we have discussed the implementation of the holographic modal wavefront sensor using a proof of principle setup, where we could measure the RMS amplitude of the Zernike modes present in an incident beam upto a reasonable accuracy.

# Chapter 5

# Estimation of Inter-modal Cross Talk in a Modal Wavefront Sensor

## 5.1 Introduction

In chapter 2 we discuss about the issue of the inter-modal cross talk in a modal wavefront sensor and the importance of an elaborate study of the issue. In this chapter we take up the issue of inter-modal cross talk and perform both, a theoretical and an experimental investigation. After the successful implementation of the holographic modal wavefront sensor, it is now possible to perform elaborate experiments necessary to understand the cross talk behavior of the sensor. The chapter begins with a theoretical investigation to come up with an expression that gives a quantitative measure of the inter-modal cross talk. We then demonstrate the effect of the presence of few lower order aberration modes on the output of the sensor assigned to detect a few primary aberration modes. The chapter ends with the experimental results on the inter-modal cross talk using the holographic modal wavefront sensor setup.

## 5.2 Theoretical consideration

As described by Eq. 2.29 of chapter 2, the complex amplitude of the light beam at the entrance pupil plane of a focusing lens $E(r, \theta)$ can be represented in terms of Zernike polynomials as

$$E(r,\theta) = \exp\left[i\sum_{j=1}^{\infty} a_j Z_j(r,\theta)\right] P_f(r,\theta) \tag{5.1}$$

where, $(r,\theta)$ are the pupil plane coordinates and the other parameters have their usual meanings. The intensity distribution, $I(\rho,\alpha)$, in the focal plane of the lens can thus be written according to Eq. 2.31 as,

$$I(\rho,\alpha) = \frac{I_o}{\pi^2}\left|\int_0^{\infty}\int^{2\pi} exp\left[i\sum_{j=1}^{\infty} a_j Z_j(r,\theta)\right] exp\{i2\pi\rho r\cos(\alpha-\theta)\} r dr d\theta\right|^2 \tag{5.2}$$

where ($\rho$,$\alpha$) are the focal plane coordinates and $I_o$ is a constant. Now considering the principle of a basic modal wavefront sensor (discussed in Chapter 2), the laser beam is assumed to contain $a$ amount of Zernike mode $Z_s$ to be detected, the sensor mode, and $c$ amount of another Zernike mode $Z_i$, the input mode, where $a$ and $c$, respectively, are the root mean square (RMS) amplitudes, respectively. If a point detector is positioned at the center of the focal spot. then the intensity detected by the point detector can be written by using Eq. 5.2, considering $I_o = 1$, as

$$I_{a,c}(0) = \frac{1}{\pi^2}\left|\int_0^{\infty}\int_0^{2\pi} exp\{iaZ_s(r,\theta) + icZ_i(r,\theta)\} r dr d\theta\right|^2 \tag{5.3}$$

If we take $b$ as the RMS amplitude of the bias mode, the sensor output for the Type B sensor described by Eq. 2.49 can be written as,

$$O_{a,b,c} = \frac{I_{a-b,c}(0) - I_{a+b,c}(0)}{I_{a-b,c}(0) + I_{a+b,c}(0)} = \frac{\delta I_{a,b,c}}{\sigma I_{a,b,c}} \tag{5.4}$$

and the RMS wavefront error,

$$\Phi_{RMS} = \frac{O_{a,b,c}}{S_B} = \frac{1}{S_B} \times \frac{\delta I_{a,b,c}}{\sigma I_{a,b,c}} \tag{5.5}$$

where, $S_B = \frac{O_{\delta a,b,c} - O_{-\delta a,b,c}}{2\delta a}$ is the sensitivity of the Type B sensor. Here $\delta a$ is a small increase in the RMS amplitude from the zero value. In the coming sections we will exclusively use the expression of Type B sensor output only. Thus in this chapter, by sensor output we mean the Type B sensor output. The sensor output is calculated by evaluating the integrations on the right hand side (RHS) of Eq. 5.4. We consider the sensor modes $Z_4, Z_5, Z_7$ and $Z_{11}$ in presence of different amplitudes $c$ of input

modes $Z_4, Z_5, Z_7, Z_9$ and $Z_{11}$. Figure 5.1(i-iv) show the plots of $\Phi_{RMS}$ calculated using Eq. 5.5 for sensor mode $Z_s$ where $s$=4, 5, 7 and 11, respectively verses $c$ varying from 0 to 1 radian, where $a$ and $b$ are 0.5 and 0.7 radians, respectively. $S_B$ for a particular sensor mode is calculated taking $\delta a$ as 0.1 radian. The black, blue, red, violet and green color curves represent the effect of the presence of $Z_4$, $Z_5$, $Z_7$, $Z_9$ and $Z_{11}$ modes, respectively, on the sensor output for the sensor mode $Z_s$. It is observed that the presence of some of the input modes in the incident beam apart from the sensor mode itself affect the sensor output to a significant amount, leading to what is known as inter-modal cross talk. The effect of the inter-modal cross talk is observed to increase as the RMS amplitude $c$ of the input mode increases [75]. However, the presence of inter-modal cross talk calculated in this manner involves evaluation of several integrals for each combination of sensor mode and input mode. For high speed applications of the modal wavefront sensor one may need a quick way of knowing the effect of inter-modal cross talk for a given amount of a specific input mode and sensor mode combination. Below we develop the theoretical expressions to propose a quick way of calculating the effect of inter-modal cross talk.

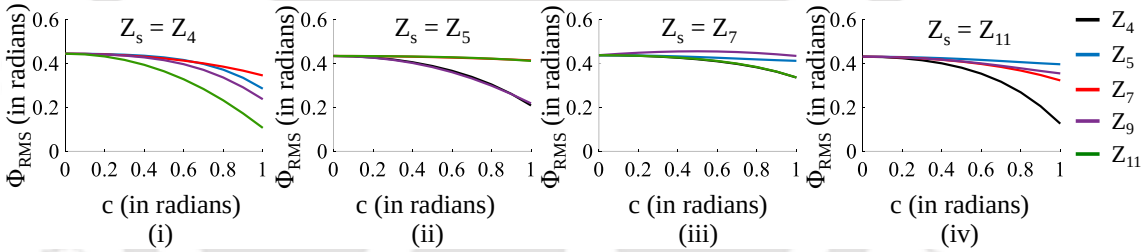


**Figure 5.1:** Plot of $\Phi_{RMS}$ of sensor mode $Z_s$ where (i) $s = 4$, (ii) $s = 5$, (iii) $s = 7$ and (iv) $s = 11$, obtained from Eqs. 5.4 and 5.5 versus RMS amplitude (in radians) of input modes $Z_i$ where $i = 4, 5, 7, 9, 11$ and $i \neq s$.

We start with the use of Taylor series expansion to expand the exponential term on the RHS of Eq. 5.3. Equation 5.3 after the expansion takes the form,

$$I_{a,c}(0) = \left| \int_0^{\infty} \int_0^{2\pi} \sum_{p=0}^{\infty} \frac{[iaZ_s]^p}{p!} \sum_{q=0}^{\infty} \frac{[icZ_i]^q}{q!} r dr d\theta \right|^2 \tag{5.6}$$

$$= \left| \int_0^{\infty} \int_0^{2\pi} \sum_{p,q=0}^{\infty} \frac{i^{(p+q)} a^p {Z_s}^p c^q {Z_i}^q}{p!q!} r dr d\theta \right|^2 \tag{5.7}$$

It is to be noted that $\frac{1}{\pi^2}$ is a constant that finally gets canceled out while calculating the type-B sensor output. Thus for simplicity, $\frac{1}{\pi^2}$ is neglected during our analysis.

After separating the real and imaginary parts on the R.H.S of Eq. 5.7 we get

$$\begin{aligned} I_{a,c}(0) &= \left| \int_0^{\infty} \int_0^{2\pi} \sum_{p+q=even} \frac{(-1)^{\frac{p+q}{2}} a^p {Z_s}^p c^q {Z_i}^q}{p!q!} r dr d\theta \right. \\ &+ \left. i \int_0^{\infty} \int_0^{2\pi} \sum_{p+q=odd} \frac{(-1)^{\frac{p+q-1}{2}} a^p {Z_s}^p c^q {Z_i}^q}{p!q!} r dr d\theta \right|^2 \qquad (5.8) \\ &= \left[ \int_0^{\infty} \int_0^{2\pi} \sum_{p+q=even} \frac{(-1)^{\frac{p+q}{2}} a^p {Z_s}^p c^q {Z_i}^q}{p!q!} r dr d\theta \right]^2 \\ &+ \left[ \int_0^{\infty} \int_0^{2\pi} \sum_{p+q=odd} \frac{(-1)^{\frac{p+q-1}{2}} a^p {Z_s}^p c^q {Z_i}^q}{p!q!} r dr d\theta \right]^2 \qquad (5.9) \end{aligned}$$

However,

$$p+q = \text{even if} \begin{cases} p \text{ and } q \text{ both are even} \\ p \text{ and } q \text{ both are odd} \end{cases}$$

$$p+q = \text{odd if} \begin{cases} p \text{ is even and } q \text{ is odd} \\ p \text{ is odd and } q \text{ is even} \end{cases}$$

Therefore, Eq. 5.9 can be written as,

$$\begin{aligned} I_{a,c}(0) &= \left[ \int_0^{\infty} \int_0^{2\pi} \sum_{p=even} \sum_{q=even} \frac{(-1)^{\frac{p+q}{2}} a^p {Z_s}^p c^q {Z_i}^q}{p!q!} r dr d\theta \right. \\ &+ \left. \int_0^{\infty} \int_0^{2\pi} \sum_{p=odd} \sum_{q=odd} \frac{(-1)^{\frac{p+q}{2}} a^p {Z_s}^p c^q {Z_i}^q}{p!q!} r dr d\theta \right]^2 \\ &+ \left[ \int_0^{\infty} \int_0^{2\pi} \sum_{p=even} \sum_{q=odd} \frac{(-1)^{\frac{p+q-1}{2}} a^p {Z_s}^p c^q {Z_i}^q}{p!q!} r dr d\theta \right. \\ &+ \left. \int_0^{\infty} \int_0^{2\pi} \sum_{p=odd} \sum_{q=even} \frac{(-1)^{\frac{p+q-1}{2}} a^p {Z_s}^p c^q {Z_i}^q}{p!q!} r dr d\theta \right]^2 \qquad (5.10) \end{aligned}$$

Now, we define two functions

$$\begin{aligned} f_e(u,v) &= \int_0^{\infty} \int_0^{2\pi} \frac{(-1)^{\frac{2u+2v}{2}} a^{2u} {Z_s}^{2u} c^{2v} {Z_i}^{2v}}{(2u)!(2v)!} r dr d\theta \\ f_o(u,v) &= \int_0^{\infty} \int_0^{2\pi} \frac{(-1)^{\frac{2u+2v-1}{2}} a^{2u} {Z_s}^{2u} c^{2v} {Z_i}^{2v}}{(2u)!(2v)!} r dr d\theta \end{aligned} \qquad (5.11)$$

Using the two functions $f_e(u,v)$ and $f_o(u,v)$ in Eq. 5.10 we get

$$I_{a,c}(0) = \left[\sum_{u,v=0}^{\infty} f_e(u,v) + \sum_{u,v=0}^{\infty} f_e(u+\frac{1}{2}, v+\frac{1}{2})\right]^2 + \left[\sum_{u,v=0}^{\infty} f_o(u, v+\frac{1}{2}) + \sum_{u,v=0}^{\infty} f_o(u+\frac{1}{2}, v)\right]^2 \tag{5.12}$$

Expanding the RHS of Eq. 5.12 we have

$$\begin{aligned} I_{a,c}(0) &= \left[\sum_{u,v=0}^{\infty} f_e(u,v)\right]^2 + \left[\sum_{u,v=0}^{\infty} f_e(u+\frac{1}{2}, v+\frac{1}{2})\right]^2 \\ &+ 2\sum_{u,v=0}^{\infty} f_e(u,v) \sum_{u,v=0}^{\infty} f_e(u+\frac{1}{2}, v+\frac{1}{2}) + \left[\sum_{u,v=0}^{\infty} f_o(u, v+\frac{1}{2})\right]^2 \\ &+ \left[\sum_{u,v=0}^{\infty} f_o(u+\frac{1}{2}, v)\right]^2 + 2\sum_{u,v=0}^{\infty} f_o(u, v+\frac{1}{2}) \sum_{u,v=0}^{\infty} f_o(u+\frac{1}{2}, v) \end{aligned} \tag{5.13}$$

Separating the $c$ dependent and $c$ independent terms we can write

$$\begin{aligned} I_{a,c}(0) &= \left[\sum_{u=0}^{\infty} f_e(u,0) + \sum_{u=0,v=1}^{\infty} f_e(u,v)\right]^2 + \left[\sum_{u,v=0}^{\infty} f_e(u+\frac{1}{2}, v+\frac{1}{2})\right]^2 \\ &+ 2\sum_{u,v=0}^{\infty} f_e(u,v) \sum_{u,v=0}^{\infty} f_e(u+\frac{1}{2}, v+\frac{1}{2}) + \left[\sum_{u,v=0}^{\infty} f_o(u, v+\frac{1}{2})\right]^2 \\ &+ \left[\sum_{u=0}^{\infty} f_o(u+\frac{1}{2}, 0) + \sum_{u=0,v=1}^{\infty} f_o(u+\frac{1}{2}, v)\right]^2 \\ &+ 2\sum_{u,v=0}^{\infty} f_o(u, v+\frac{1}{2}) \sum_{u,v=0}^{\infty} f_o(u+\frac{1}{2}, v) \end{aligned} \tag{5.14}$$

After expanding and rearranging the RHS of the above equation

$$
\begin{aligned}
I_{a,c}(0) &= \left[\sum_{u=0}^{\infty} f_e(u,0)\right]^2 + \left[\sum_{u=0}^{\infty} f_o(u+\frac{1}{2},0)\right]^2 + \left[\sum_{u,v=0}^{\infty} f_e(u+\frac{1}{2},v+\frac{1}{2})\right]^2 \\
&+ \left[\sum_{u,v=0}^{\infty} f_o(u,v+\frac{1}{2})\right]^2 + \left[\sum_{u=0,v=1}^{\infty} f_o(u+\frac{1}{2},v)\right]^2 + \left[\sum_{u=0,v=1}^{\infty} f_e(u,v)\right]^2 \\
&+ 2\left[\sum_{u=0}^{\infty} f_e(u,0) \sum_{u=0,v=1}^{\infty} f_e(u,v) + \sum_{u,v=0}^{\infty} f_e(u,v) \sum_{u,v=0}^{\infty} f_e(u+\frac{1}{2},v+\frac{1}{2})\right. \\
&+ \sum_{u=0}^{\infty} f_o(u+\frac{1}{2},0) \sum_{u=0,v=1}^{\infty} f_o(u+\frac{1}{2},v) \\
&+ \left.\sum_{u,v=0}^{\infty} f_o(u,v+\frac{1}{2}) \sum_{u,v=0}^{\infty} f_o(u+\frac{1}{2},v)\right] \qquad (5.15)
\end{aligned}
$$

Thus, the intensity at the point detector can be written in terms of $c$ dependent and $c$ independent terms as,

$$I_{a,c}(0) = I_a^{NC}(0) + I_{a,c}^{C}(0) \qquad (5.16)$$

where,

$$I_a^{NC}(0) = \left[\sum_{u=0}^{\infty} f_e(u,0)\right]^2 + \left[\sum_{u=0}^{\infty} f_o(u+\frac{1}{2},0)\right]^2 \qquad (5.17)$$

and

$$
\begin{aligned}
I_{a,c}^{C}(0) &= \left[\sum_{u,v=0}^{\infty} f_e(u+\frac{1}{2},v+\frac{1}{2})\right]^2 + \left[\sum_{u,v=0}^{\infty} f_o(u,v+\frac{1}{2})\right]^2 \\
&+ \left[\sum_{u=0,v=1}^{\infty} f_o(u+\frac{1}{2},v)\right]^2 + \left[\sum_{u=0,v=1}^{\infty} f_e(u,v)\right]^2 \\
&+ 2\left[\sum_{u=0}^{\infty} f_e(u,0) \sum_{u=0,v=1}^{\infty} f_e(u,v)\right. \\
&+ \sum_{u,v=0}^{\infty} f_e(u,v) \sum_{u,v=0}^{\infty} f_e(u+\frac{1}{2},v+\frac{1}{2}) \\
&+ \sum_{u=0}^{\infty} f_o(u+\frac{1}{2},0) \sum_{u=0,v=1}^{\infty} f_o(u+\frac{1}{2},v) \\
&+ \left.\sum_{u,v=0}^{\infty} f_o(u,v+\frac{1}{2}) \sum_{u,v=0}^{\infty} f_o(u+\frac{1}{2},v)\right] \qquad (5.18)
\end{aligned}
$$

The output of the sensor can be written as,

$$O_{a,b,c} = \frac{\delta I^{NC}_{a,b} + \delta I^{C}_{a,b,c}}{\sigma I^{NC}_{a,b} + \sigma I^{C}_{a,b,c}} \tag{5.19}$$

where,

$$\begin{aligned}
\delta I^{NC}_{a,b} &= I^{NC}_{a-b}(0) - I^{NC}_{a+b}(0) \\
\delta I^{C}_{a,b,c} &= I^{C}_{a-b,c}(0) - I^{C}_{a+b,c}(0) \\
\sigma I^{NC}_{a,b} &= I^{NC}_{a-b}(0) + I^{NC}_{a+b}(0) \\
\sigma I^{C}_{a,b,c} &= I^{C}_{a-b,c}(0) + I^{C}_{a+b,c}(0)
\end{aligned}$$

The expression of sensor output can be further expressed as the product of two terms as

$$O_{a,b,c} = O^{NC}_{a,b} \times F_{a,c} \tag{5.20}$$

where,

$$O^{NC}_{a,b} = \frac{\delta I^{NC}_{a,b}}{\sigma I^{NC}_{a,b}} = \text{Ideal sensor output} \tag{5.21}$$

and

$$F_{a,c} = \frac{1 + \frac{\delta I^{C}_{a,b,c}}{\delta I^{NC}_{a,b}}}{1 + \frac{\sigma I^{C}_{a,b,c}}{\sigma I^{NC}_{a,b}}} = \left(1 + \frac{\delta I^{C}_{a,b,c}}{\delta I^{NC}_{a,b}}\right)\left(1 + \frac{\sigma I^{C}_{a,b,c}}{\sigma I^{NC}_{a,b}}\right)^{-1} \tag{5.22}$$

$F_{a,c}$ represent the deviation of the actual sensor output from the ideal sensor output (when only the sensor mode is present). $F_{a,c}$ is a factor that is to be multiplied with the ideal sensor output to obtain the actual sensor output and is referred to as the inter-modal cross talk co-efficient [76]. In the ideal case (i.e. no cross talk) the value of $F_{a,c}$ is unity and any deviation from unity indicates the presence of inter-modal cross talk with its strength indicating the magnitude of the inter-modal cross talk. The RMS wavefront error, $\Phi_{RMS}$ also has a direct link with the co-efficient $F_{a,c}$ as

$$\Phi_{RMS} = \frac{\lambda}{\frac{2\pi}{a(1-F_{a,c})}} \tag{5.23}$$

where, $\lambda$ is the wavelength of the incident beam. The expression of $F_{a,c}$ can also be expanded binomially as,

$$F_{a,c} = \sum_{n=0}^{\infty} (-1)^n \left(\frac{\sigma I^C_{a,b,c}}{\sigma I^{NC}_{a,b}}\right)^n + \frac{\delta I^C_{a,b,c}}{\delta I^{NC}_{a,b}} \sum_{n=0}^{\infty} (-1)^n \left(\frac{\sigma I^C_{a,b,c}}{\sigma I^{NC}_{a,b}}\right)^n \tag{5.24}$$

The RHS of the above expression is expanded and rearranged to separate the terms with same power of $c$, to get a polynomial form of the expression as,

$$F_{a,c} = 1 + cA_1 + c^2A_2 + c^3A_3 + c^4A_4 + c^5A_5 \tag{5.25}$$

where, the polynomial expression is retained up to the fifth power of $c$ and

$$\begin{aligned}
A_1 &= \delta C_1 - \sigma C_1 \\
A_2 &= \delta C_2 - \sigma C_2 + \sigma C_1^2 - \delta C_1 \sigma C_1 \\
A_3 &= \delta C_3 - \sigma C_3 + 2\sigma C_1 \sigma C_2 - \sigma C_1^3 - \delta C_2 \sigma C_1 \\
&\quad -\delta C_1 \sigma C_2 + \delta C_1 \sigma C_1^2 \\
A_4 &= \delta C_4 - \sigma C_4 + \sigma C_2^2 + 2\sigma C_1 \sigma C_3 - 3\sigma C_1^2 \sigma C_2 \\
&\quad +\sigma C_1^4 - \delta C_3 \sigma C_1 + \delta C_2 \sigma C_1^2 + 2\delta C_1 \sigma C_1 \sigma C_2 \\
&\quad -\delta C_2 \sigma C_2 - \delta C_1 \sigma C_3 - \delta C_1 \sigma C_1^3 \\
A_5 &= \delta C_5 - \sigma C_5 + 2\sigma C_1 \sigma C_4 + 2\sigma C_2 \sigma C_3 - 3\sigma C_1^2 \sigma C_3 \\
&\quad -3\sigma C_2^2 \sigma C_1 + 4\sigma C_1^3 \sigma C_2 - \sigma C_1^5 - \delta C_4 \sigma C_1 \\
&\quad -\delta C_3 \sigma C_2 - \delta C_2 \sigma C_3 - \delta C_1 \sigma C_4 + \delta C_3 \sigma C_1^2 \\
&\quad +2\delta C_2 \sigma C_1 \sigma C_2 + \delta C_1 \sigma C_2^2 + 2\delta C_1 \sigma C_1 \sigma C_3 \\
&\quad -\delta C_2 \sigma C_1^3 - 3\delta C_1 \sigma C_1^2 \sigma C_2 + \delta C_1 \sigma C_1^4
\end{aligned} \tag{5.26}$$

Further,

$$\begin{aligned}
\sigma C_{1,2,3,4,5} &= \left(\frac{1}{\sigma I^{NC}_{a,b}}\right)\{C_{1,2,3,4,5}(a-b) + C_{1,2,3,4,5}(a+b)\} \\
\delta C_{1,2,3,4,5} &= \left(\frac{1}{\delta I^{NC}_{a,b}}\right)\{C_{1,2,3,4,5}(a-b) - C_{1,2,3,4,5}(a+b)\}
\end{aligned} \tag{5.27}$$

where,

$$
\begin{aligned}
C_1(a) &= \frac{1}{c}\{2\sum_{u=0}^{\infty} f_o(u,\frac{1}{2})\sum_{u=0}^{\infty} f_o(u+\frac{1}{2},0) \\
&\quad +2\sum_{u=0}^{\infty} f_e(u,0)\sum_{u=0}^{\infty} f_e(u+\frac{1}{2},\frac{1}{2})\} \\
C_2(a) &= \frac{1}{c^2}\{|\sum_{u=0}^{\infty} f_e(u+\frac{1}{2},\frac{1}{2})|^2+|\sum_{u=0}^{\infty} f_o(u,\frac{1}{2})|^2 \\
&\quad +2\sum_{u=0}^{\infty} f_e(u,0)\sum_{u=0}^{\infty} f_e(u,1) \\
&\quad +2\sum_{u=0}^{\infty} f_o(u+\frac{1}{2},0)\sum_{u=0}^{\infty} f_o(u+\frac{1}{2},1)\} \\
C_3(a) &= \frac{1}{c^3}\{2\sum_{u=0}^{\infty} f_e(u,0)\sum_{u=0}^{\infty} f_e(u+\frac{1}{2},\frac{3}{2}) \\
&\quad +2\sum_{u=0}^{\infty} f_e(u,1)\sum_{u=0}^{\infty} f_e(u+\frac{1}{2},\frac{1}{2}) \\
&\quad +2\sum_{u=0}^{\infty} f_o(u,\frac{1}{2})\sum_{u=0}^{\infty} f_o(u+\frac{1}{2},1) \\
&\quad +2\sum_{u=0}^{\infty} f_o(u,\frac{3}{2})\sum_{u=0}^{\infty} f_o(u+\frac{1}{2},0)\}
\end{aligned}
\tag{5.28}
$$

$$
\begin{aligned}
C_4(a) &= \frac{1}{c^4}\{|\sum_{u=0}^{\infty} f_o(u+\frac{1}{2},1)|^2+|\sum_{u=0}^{\infty} f_e(u,1)|^2 \\
&\quad +2\sum_{u=0}^{\infty} f_e(u+\frac{1}{2},\frac{1}{2})\sum_{u=0}^{\infty} f_e(u+\frac{1}{2},\frac{3}{2}) \\
&\quad +2\sum_{u=0}^{\infty} f_o(u,\frac{1}{2})\sum_{u=0}^{\infty} f_o(u,\frac{3}{2}) \\
&\quad +2\sum_{u=0}^{\infty} f_e(u,0)\sum_{u=0}^{\infty} f_e(u,2) \\
&\quad +2\sum_{u=0}^{\infty} f_o(u+\frac{1}{2},0)\sum_{u=0}^{\infty} f_o(u+\frac{1}{2},2)\}
\end{aligned}
$$

$$
\begin{aligned}
C_5(a) \;=\; & \frac{1}{c^5}\{2\sum_{u=0}^{\infty} f_e(u,0)\sum_{u=0}^{\infty} f_e(u+\frac{1}{2},\frac{5}{2}) \\
& +2\sum_{u=0}^{\infty} f_e(u,1)\sum_{u=0}^{\infty} f_e(u+\frac{1}{2},\frac{3}{2}) \\
& +2\sum_{u=0}^{\infty} f_e(u,2)\sum_{u=0}^{\infty} f_e(u+\frac{1}{2},\frac{1}{2}) \\
& +2\sum_{u=0}^{\infty} f_o(u,\frac{1}{2})\sum_{u=0}^{\infty} f_o(u+\frac{1}{2},2) \\
& +2\sum_{u=0}^{\infty} f_o(u,\frac{3}{2})\sum_{u=0}^{\infty} f_o(u+\frac{1}{2},1) \\
& +2\sum_{u=0}^{\infty} f_o(u,\frac{5}{2})\sum_{u=0}^{\infty} f_o(u+\frac{1}{2},0)\}
\end{aligned}
$$

Equation 5.25 representing the polynomial form of $F_{a,c}$, enables an easy and fast way of estimating the amount of inter-modal cross talk for a range of $c$ values. Here $a$ and $b$ are taken as constants whose values are set as per the requirement of the application. We employ Eqs. 5.11, 5.26, 5.27 and 5.28, to calculate the co-efficients ($A_i$) of the polynomial form of $F_{a,c}$ (in Eq. 5.25). We consider the sensor modes $Z_s$, $s = 4 \rightarrow 11$, in the presence of input modes $Z_i$, $i = 4 \rightarrow 11$. The co-efficients are obtained taking $a$ and $b$ as 0.5 and 0.7 radians, respectively and $u$ ranging from 0 to 4.

The calculated values of the co-efficients $A_i$ are shown in Table 5.1. We limit the polynomial to the fifth power of $c$ and thus the table includes the numerical values of the co-efficients $A_1$, $A_2$, $A_3$, $A_4$ and $A_5$. It is observed that apart from a few pairs of input mode and sensor mode combinations, the polynomial form of $F_{a,c}$ (up to the fifth power of $c$) has a maximum of only two non zero values of $A_i$.

## 5.3 Computation of cross talk influence using inter-modal cross talk co-efficient

The cross talk co-efficient $F_{a,c}$ can also be computed from the integral form ( Eqs. 5.4 and 5.3) of the sensor output. $F_{a,c}$ can be defined as the ratio of the actual

**Table 5.1:** Table of co-efficients in the $F_{a,c}$ polynomial.

| $\mathbf{Z_s}$ | $\mathbf{A_i}$ | **Input mode ($\mathbf{Z_i}$)** | | | | | | | |
|---|---|---|---|---|---|---|---|---|---|
| | | $Z_4$ | $Z_5$ | $Z_6$ | $Z_7$ | $Z_8$ | $Z_9$ | $Z_{10}$ | $Z_{11}$ |
| $Z_4$ | $A_1$ | – | 0 | 0 | 0 | 0 | 0 | 0 | 0 |
| | $A_2$ | – | -0.0932 | -0.0932 | -0.1864 | -0.1864 | -0.18638 | -0.1864 | -0.6995 |
| | $A_3$ | – | 0 | 0 | 0 | 0 | 0 | 0 | 0 |
| | $A_4$ | – | -0.2166 | -0.2166 | -0.0292 | -0.0292 | -0.3085 | -0.3085 | -0.0920 |
| | $A_5$ | – | 0 | 0 | 0 | 0 | 0 | 0 | 0 |
| $Z_5$ | $A_1$ | 0 | – | 0 | 0 | 0 | 0 | 0 | 0 |
| | $A_2$ | -0.3932 | – | 0.0199 | -0.0466 | -0.0466 | -0.4467 | -0.4467 | -0.0316 |
| | $A_3$ | 0 | – | 0 | 0 | 0 | 0 | 0 | 0 |
| | $A_4$ | -0.0998 | – | -0.0142 | 0.0003 | 0.0003 | -0.0813 | -0.0813 | -0.0139 |
| | $A_5$ | 0 | – | 0 | 0 | 0 | 0 | 0 | 0 |
| $Z_6$ | $A_1$ | 0 | 0 | – | 0 | 0 | 0 | 0 | 0 |
| | $A_2$ | -0.3932 | 0.0199 | – | -0.0466 | -0.0466 | -0.4467 | -0.4467 | -0.0316 |
| | $A_3$ | 0 | 0 | – | 0 | 0 | 0 | 0 | 0 |
| | $A_4$ | -0.0998 | -0.0142 | – | -0.0339 | -0.0339 | -0.1013 | -0.1013 | -0.0139 |
| | $A_5$ | 0 | 0 | – | 0 | 0 | 0 | 0 | 0 |
| $Z_7$ | $A_1$ | 0 | 0 | 0 | – | 0 | 0.1522 | 0 | 0 |
| | $A_2$ | -0.1556 | -0.0802 | -0.1794 | – | 0.0680 | -0.1083 | -0.0980 | -0.1373 |
| | $A_3$ | 0 | 0 | 0 | – | 0 | -0.07818 | 0 | 0 |
| | $A_4$ | -0.0497 | 0.0139 | 0.0096 | – | 0.0082 | 0.0361 | 0.0301 | -0.0691 |
| | $A_5$ | 0 | 0 | 0 | – | 0 | -0.0210 | 0 | 0 |
| $Z_8$ | $A_1$ | 0 | 0 | 0 | 0 | – | 0 | -0.1522 | 0 |
| | $A_2$ | -0.1556 | -0.0802 | -0.1794 | 0.0680 | – | -0.0980 | -0.1083 | -0.1373 |
| | $A_3$ | 0 | 0 | 0 | 0 | – | 0 | 0.0782 | 0 |
| | $A_4$ | -0.0497 | 0.0139 | 0.0096 | 0.0082 | – | 0.0301 | 0.0361 | -0.0691 |
| | $A_5$ | 0 | 0 | 0 | 0 | – | 0 | 0.0210 | 0 |
| $Z_9$ | $A_1$ | 0 | 0 | 0 | 0 | 0 | – | 0 | 0 |
| | $A_2$ | -0.5595 | -0.4684 | -0.4684 | -0.0881 | -0.0881 | – | -0.1278 | -0.0901 |
| | $A_3$ | 0 | 0 | 0 | 0.0290 | 0 | – | 0 | 0 |
| | $A_4$ | -0.1096 | -0.0922 | -0.0922 | 0.0225 | 0.0225 | – | -0.0539 | -0.0413 |
| | $A_5$ | 0 | 0 | 0 | 0.0004 | 0 | – | 0 | 0 |
| $Z_{10}$ | $A_1$ | 0 | 0 | 0 | 0 | 0 | 0 | – | 0 |
| | $A_2$ | -0.5595 | -0.4684 | -0.4684 | -0.0881 | -0.0881 | -0.1278 | – | -0.0901 |
| | $A_3$ | 0 | 0 | 0 | 0 | -0.0290 | 0 | – | 0 |
| | $A_4$ | -0.1096 | -0.0922 | -0.0922 | 0.0225 | 0.0225 | -0.0539 | – | -0.0413 |
| | $A_5$ | 0 | 0 | 0 | 0 | -0.0004 | 0 | – | 0 |
| $Z_{11}$ | $A_1$ | 0 | 0 | 0 | 0 | 0 | 0 | 0 | – |
| | $A_2$ | -0.3933 | -0.0983 | -0.0983 | -0.1967 | -0.1967 | -0.1967 | -0.1967 | – |
| | $A_3$ | 0 | 0 | 0 | 0 | 0 | 0 | 0 | – |
| | $A_4$ | -0.2705 | 0.0047 | 0.0047 | -0.0465 | -0.0465 | -0.0131 | -0.0131 | – |
| | $A_5$ | 0 | 0 | 0 | 0 | 0 | 0 | 0 | – |

sensor output to the ideal sensor output, such that

$$F_{a,c} = \left(\frac{\delta I_{a,b,c}}{\sigma I_{a,b,c}}\right)\left(\frac{\delta I_{a,b,c=0}}{\sigma I_{a,b,c=0}}\right)^{-1} \tag{5.29}$$

Taking the RMS amplitudes $a$ and $b$ of sensor mode $Z_s$, as 0.5 and 0.7 radians, respectively and varying the RMS amplitude $c$ of input mode $Z_i$, from 0 to 1 radian, $F_{a,c}$ is calculated using Eq. 5.29 for the sensor mode $Z_4$, $Z_5$, $Z_7$ and $Z_{11}$ in the presence of input modes $Z_4$, $Z_5$, $Z_7$, $Z_9$ and $Z_{11}$. Further, using Eq. 5.25 (i.e. the polynomial form of $F_{a,c}$) and Table 5.1, $F_{a,c}$ is again calculated for the same combination of sensor mode and input mode.

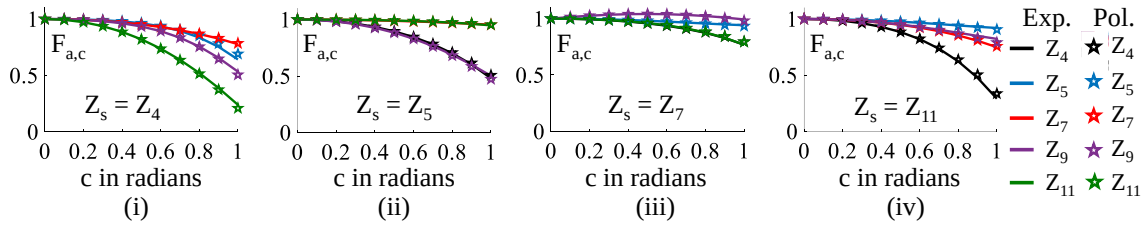


**Figure 5.2:** The plots of $F_{a,c}$ for the sensor mode $Z_s$ where (i) $s = 4$, (ii) $s = 5$ (iii) $s = 7$ and (iv) $s = 11$ in the presence of input mode $Z_i$ where $i = 4, 5, 7, 9, 11$ and $i \neq s$. The solid curves represent the data obtained using the integral form of the sensor output while the star marks represent the data obtained using the polynomial form of $F_{a,c}$.

Figure 5.2 shows the plots of $F_{a,c}$ for the sensor modes $Z_s$, $s = 4, 5, 7, 11$, in the presence of input modes $Z_i$, $i = 4, 5, 7, 9, 11$ and $i \neq s$, verses the RMS amplitude of input mode $c$, calculated using both the integral form and the polynomial form. The plots of Figs. 5.2(i $\rightarrow$ iv) are for $Z_4$, $Z_5$, $Z_7$ and $Z_{11}$ sensor modes, respectively. The solid curves are the plots of the data obtained from the integral expression of $F_{a,c}$ while the star ($\star$) marked plots are from the data obtained from the polynomial expression of $F_{a,c}$. The color black, blue, red, violet and green represent the plots in presence of input modes $Z_4$, $Z_5$, $Z_7$, $Z_9$ and $Z_{11}$, respectively. The figures indicate that the polynomial form of the inter-modal cross talk co-efficient provides a quantitatively good approximate of the co-efficients obtained using the integral form of the sensor output. Increasing the upper limit of the powers of $c$ (i.e. greater than 5), the agreement can be further improved.

Now, employing the polynomial form i.e. Eq. 5.25 and Table 5.1, $F_{a,c}$ is calculated for sensor modes $Z_s$ with $s = 4 \rightarrow 11$ using $a = 0.5$ and $b = 0.7$ in presence of

**Table 5.2:** Table of $F_{a,c}$ for some low order Zernike modes.

| **c** | $\mathbf{Z_s}$ | **input mode** ($\mathbf{Z_i}$) | | | | | | | |
|---|---|---|---|---|---|---|---|---|---|
| | | $Z_4$ | $Z_5$ | $Z_6$ | $Z_7$ | $Z_8$ | $Z_9$ | $Z_{10}$ | $Z_{11}$ |
| c=0.5 | $Z_4$ | – | 0.9632 | 0.9632 | 0.9516 | 0.9516 | 0.9341 | 0.9341 | 0.8193 |
| | $Z_5$ | 0.8955 | – | 1.0041 | 0.9884 | 0.9884 | 0.8832 | 0.8832 | 0.9912 |
| | $Z_6$ | 0.8955 | 1.0041 | – | 0.9862 | 0.9862 | 0.8820 | 0.8820 | 0.9912 |
| | $Z_7$ | 0.9580 | 0.9808 | 0.9557 | – | 1.0175 | 1.0409 | 0.9774 | 0.9613 |
| | $Z_8$ | 0.9580 | 0.9808 | 0.9555 | 1.0175 | – | 0.9774 | 0.9095 | 0.9613 |
| | $Z_9$ | 0.8533 | 0.8771 | 0.8771 | 0.9830 | 0.9794 | – | 0.9647 | 0.9749 |
| | $Z_{10}$ | 0.8533 | 0.8771 | 0.8771 | 0.9794 | 0.9757 | 0.9647 | – | 0.9749 |
| | $Z_{11}$ | 0.8848 | 0.9757 | 0.9757 | 0.9479 | 0.9479 | 0.9500 | 0.9500 | – |
| c=1.0 | $Z_4$ | – | 0.6902 | 0.6902 | 0.7844 | 0.7844 | 0.5051 | 0.5051 | 0.2084 |
| | $Z_5$ | 0.5070 | – | 1.0058 | 0.9536 | 0.9536 | 0.4720 | 0.4720 | 0.9545 |
| | $Z_6$ | 0.5070 | 1.0058 | – | 0.9194 | 0.9194 | 0.4521 | 0.4521 | 0.9545 |
| | $Z_7$ | 0.7947 | 0.9337 | 0.8302 | – | 1.0762 | 0.9808 | 0.9321 | 0.7935 |
| | $Z_8$ | 0.7947 | 0.9337 | 0.8302 | 1.0762 | – | 0.9321 | 0.8746 | 0.7935 |
| | $Z_9$ | 0.3309 | 0.4394 | 0.4394 | 0.9637 | 0.9343 | – | 0.8183 | 0.8685 |
| | $Z_{10}$ | 0.3309 | 0.4394 | 0.4394 | 0.9343 | 0.9050 | 0.8183 | – | 0.8685 |
| | $Z_{11}$ | 0.3362 | 0.9064 | 0.9064 | 0.7568 | 0.7568 | 0.7902 | 0.7902 | – |

input modes $Z_i$ with $i = 4 \rightarrow 11$ and $i \neq s$. The numerical values of $F_{a,c}$ for $c = 0.5$ and $c = 1.0$ are arranged in Table 5.2.

The Table indicates a significant effect of the presence of a certain input mode on the sensor output for most of the sensor modes. The well known effect of the input mode $Z_{11}$ on the sensor mode $Z_4$ and vice versa is clearly observed. The effect of the input mode $Z_{11}$ on the sensor mode $Z_4$ is found to be larger compared to the effect of the input mode $Z_4$ on the sensor mode $Z_{11}$ at $c = 0.5$ radian, while the condition is reversed at $c = 1$ radian. It is also noticed that even a moderate amount ($\approx 0.5$ radian) of the input modes show considerable effect on the sensor output for most of the sensor modes. For instance, the effect of the presence of $Z_{4,9,10}$ modes on $Z_{5,6}$ sensors ($\phi_{RMS} \approx \frac{\lambda}{105}$), effect of $Z_{10}$ mode on $Z_8$ sensor ($\phi_{RMS} \approx \frac{\lambda}{126}$) and effect of $Z_{4,5,6}$ modes on $Z_{9,10}$ sensors ($\phi_{RMS} \approx \frac{\lambda}{84}$). Further, it is seen that at $c = 0.5$ radian, the $Z_5$ and $Z_6$ modes show less effect than the effect of $Z_7$ and $Z_8$ modes on the $Z_4$ sensor, while the condition is reversed at $c = 1$ radian. Moreover, the presence of $Z_4$ mode imparts a nearly equal effect on $Z_{9,10,11}$ sensors at both moderate and large values of $c$.

## 5.4 Experimental verification of the polynomial form of $F_{a,c}$

The polynomial form of the inter-modal cross talk co-efficient $F_{a,c}$ is then examined experimentally using a holographic modal wavefront sensor. The experimental arrangement as shown in Fig. 5.3(i) is almost similar to the one in the previous chapter. A laser beam from a He-Ne laser having wavelength ($\lambda$) of 632.8 nm is first expanded and then collimated using lens system $L_1$ and $L_2$ to incident on a 50% beam splitter, BS. The beam that transmit through the BS is incident on a DMD panel. The DMD displays an appropriate binary hologram with the help of a computer ($PC_1$) interface giving rise to diffraction orders. The PC interface with the DMD enables display of binary hologram facilitating dynamic phase control of the +1 diffraction order up to a refresh rate of 9.5 KHz. The +1 order from the DMD is reflected by the BS to pass through a $4f$ relay lens system $L_3$ and $L_4$ to fall on a FLCSLM panel. The iris diaphragm $I_1$ allows only the +1 order beam from the DMD to pass through it while blocking the others. A binary duplex hologram is written on to the FLCSLM through the $PC_2$ interface to obtain obtain two +1 order beams acting as bias orders (one beam with a positive bias phase while the other with a negative bias phase). The diffracted beams from the FLCSLM are focused onto an iris diaphragm $I_2$ by lens $L_5$. $I_2$ allows the passage of only the biased beams that are again focused onto a CMOS digital camera by the lens $L_6$. The image captured by the camera is transferred to the $PC_2$ where a program processes the information to get the central intensity of each biased spot from which the output of the sensor can be obtained. Equation 5.29 is then used to calculate the cross talk co-efficient $F_{a,c}$ from the experimental data. To be noted that, here the FLCSLM in conjunction with the camera constitutes the holographic modal wavefront sensor, HMWFS and the DMD facilitates the modulation of the phase profile of the beam incident on the HMWFS. One may also replace the DMD with an LCSLM at the cost of the refresh rate of the display.

The beam incident on the FLCSLM is first corrected from all the residual aberrations with the help of the binary hologram written on the DMD, so that a near perfect Airy pattern corresponding to the unaberrated beam is formed at the camera. The duplex hologram on the FLCSLM is so constructed that the bias order beams are generated for sensor mode $Z_s$, where $s = 4$ or 5 using $b = 0.7$ radian. The binary

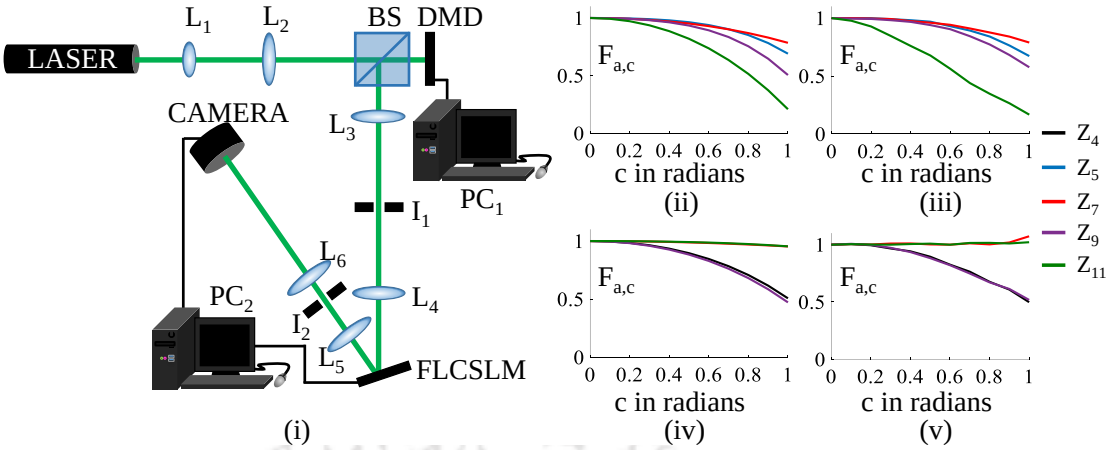


**Figure 5.3:** (i) Experimental arrangement and plots of $F_{a,c}$ verses $c$ for the $Z_4$ sensor in presence of $Z_5$, $Z_7$, $Z_9$ and $Z_{11}$ modes, obtained (i) using the polynomial expression and (iii) from the experimental data and plots of $F_{a,c}$ verses $c$ for the $Z_5$ sensor in presence of $Z_4$, $Z_7$, $Z_9$ and $Z_{11}$ modes, obtained (iv) using the polynomial expression and (v) from the experimental data.

hologram in the DMD is constructed to incorporate $a = 0.5$ radian of the sensor mode $Z_s$ and $c$ amount of input mode $Z_i$, where $i = 4, 5, 7, 9$ or 11, into the incident beam . The value of $c$ is changed from 0 to 1 radian in a step of 0.1 by updating the hologram at the DMD for each $c$ value. The data in the form of $F_{a,c}$ for the sensor mode $Z_4$ and $Z_5$ at $PC_2$ are plotted against $c$. Figures 5.3 (ii $\rightarrow$ v) show the plots of $F_{a,c}$ which is calculated using the polynomial form and obtained experimentally against $c$ for the sensor mode $Z_s$, $s = 4, 5$, in the presence of $Z_i$, $i = 4, 5, 7, 9, 11$ and $i \neq s$. Figures 5.3 (ii) and (iii) show the plots of $F_{a,c}$ verses $c$ for the $Z_4$ sensor in presence of $Z_5$, $Z_7$, $Z_9$ and $Z_{11}$ as input modes, obtained using the polynomial expression (Eq. 5.25) and experimental data, respectively. Similarly Figs. 5.3 (iv) and (v) show the plots of $F_{a,c}$ verses $c$ for the $Z_5$ sensor in presence of $Z_4$, $Z_7$, $Z_9$ and $Z_{11}$ as input modes, obtained using the polynomial expression and experimental data, respectively. The figures indicate that the experimental results agree well with the theoretical values of the inter-modal cross talk co-efficient $F_{a,c}$. Thus, the polynomial form of $F_{a,c}$ predicts the experimentally measured cross talk co-efficient to a reasonable accuracy, except for a small disagreement mainly in the case of $Z_4$ sensor in the presence of $Z_{11}$ mode. The difference in the theoretical and the experimental values of $F_{a,c}$ (represented as $\Delta[F_{a,c}] = [F_{a,c}]_{theoretical} - [F_{a,c}]_{experimental}$) of $Z_4$ and $Z_5$ sensors shown in Fig 5.3 (ii $\rightarrow$ v) is presented in Fig. 5.4. A maximum difference of $\approx 0.2$ radian is seen in case of $Z_4$ sensor in presence of $Z_{11}$ mode. Also the

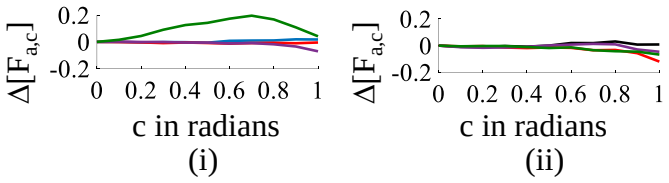


**Figure 5.4:** (i) Plots of $\Delta[F_{a,c}]$ verses $c$ for the $Z_4$ sensor in presence of $Z_5$, $Z_7$, $Z_9$ and $Z_{11}$ modes and (ii) plots of $\Delta[F_{a,c}]$ verses $c$ for the $Z_5$ sensor in presence of $Z_4$, $Z_7$, $Z_9$ and $Z_{11}$ modes.

value of the experimental $F_{a,c}$ reduces to 0.12 at $c = 1$ which is 0.2 while using its polynomial form. This disagreement can be attributed to a small mismatch between the hologram positions corresponding to the two conjugate planes at the DMD and the LCSLM. To be noted here that a mismatch in the pupil sizes may affect the sensitivity of the sensor.

## 5.5 Conclusion

In this chapter we have provided a detail investigation on the presence of the inter-modal cross talk in a modal wavefront sensor. A theoretical treatment to obtain an expression of inter-modal cross talk co-efficient, which determines the deviation of the actual sensor output from the ideal sensor output has also been provided. Such a cross talk co-efficient can be computed by evaluating several integral expressions which may differ for different combination of sensor mode and input mode descriptions. The cross talk co-efficient has been expressed as a polynomial that enables fast calculation of the extent of effect imparted by the sensor mode and input mode combinations present in the incident beam. The cross talk co-efficients obtained using the polynomial form have been compared with those obtained using the integral form. Some important observations on the inter-modal cross talk for various input modes and sensor modes have also been presented. The chapter ends with the experimental verification of the presence of inter-modal cross talk in a modal wavefront sensor as predicted by the theoretical results.

# Chapter 6

# Development of an Improved Modal Wavefront Sensor

## 6.1 Introduction

Apart from the presence of inter-modal cross talk discussed in chapter 5, the modal wavefront sensor also suffers from a low linear response (chapter 2). In this chapter, we describe a new modal wavefront sensing scheme that shows enhancement in the linear response range as well as improvement in the immunity to the presence of inter-modal cross talk. The chapter begins with the principle behind the proposed scheme and then provides a theoretical analysis that clearly indicates an improvement in the linear response range and reduction in inter-modal cross talk. The chapter ends with results of numerical simulation and experimental investigation to validate the proposed scheme.

## 6.2 Principle behind the proposed sensor

To understand the principle of the proposed sensor we start by rewriting Eq. 5.3 from chapter 5 as,

$$I(a_s, c_i) = \frac{I_o}{\pi^2} \left| \int_0^{\infty} \int_0^{2\pi} exp\{ia_s Z_s(r,\theta) + ic_i Z_i(r,\theta)\} r dr d\theta \right|^2 \tag{6.1}$$

where, $Ia_s, c_i(0)$ is the intensity as measured by a point detector at the focal pane of a lens when a beam of complex amplitude $E(r,\theta) = exp\{ia_s Z_s(r,\theta) + ic_i Z_i(r,\theta)\}$,

at the entrance pupil of the lens, is focused by it. Here, $Z_s$ and $Z_i$ are two Zernike modes taken as the sensor mode and the input mode with RMS amplitudes of $a_s$ and $c_i$, respectively.

Now following the principle of a modal wavefront sensor, where $b$ is taken as the RMS amplitude of the bias aberration ($Z_s$), the intensities at the point detectors placed at the center of the focal spots of the two bias beams can be represented as $I(a_s + b, c_i)$ and $I(a_s - b, c_i)$. Thus, the output of type-A sensor ($O_A$) and type-B sensor ($O_B$) can be written as,

$$O_A = I(a_s + b, c_i) - I(a_s - b, c_i) \tag{6.2}$$

$$O_B = \frac{I(a_s + b, c_i) - I(a_s - b, c_i)}{I(a_s + b, c_i) + I(a_s - b, c_i)} \tag{6.3}$$

The RMS wavefront errors $\Phi_{RMS}$ of the sensor mode estimated by the type-A and type-B sensors as expressed by Eqs. 2.41 and 2.51 are

$$\Phi_{RMS}(\text{type-A}) = \frac{O_A}{S_A} \tag{6.4}$$

$$\Phi_{RMS}(\text{type-B}) = \frac{O_B}{S_A} \tag{6.5}$$

where, $S_{A,B} = \frac{\delta O_{A,B}}{\delta a_s}\Big|_{a_s=0}$ represent the sensitivities of type-A and type-B sensors. As already discussed in chapter 2 the type-B sensor gives an optimized sensor output in terms of inter-modal cross talk. Hence we use the expression of the sensor output ($O_B$) of the type-B sensor as the basic expression of sensor output of the modal wavefront sensor rather than type-A sensor output. Now we consider that by some means we incorporate a variable RMS amplitude $a_v$ of the sensor mode $Z_s$, apart from the already existing RMS amplitude $a_s$ of $Z_s$, into the incident beam. The variable RMS amplitude $a_v$ can be incorporated using phase plates or any other phase modulating device. The phase profile of the incident beam thus becomes $\Phi = (a_s + a_v)Z_s + c_i Z_i$. The output of type-B sensor, $O_B$, can now be calculated for a given value of $a_s$, $b$ and $c_i$ and a range of $a_v$ values using Eq. 6.3. Figure 6.1(i) shows two plots of $O_B$ versus the RMS amplitude $a_v$ (in radian) for $Z_s = Z_5$. For both the plots $c_i$ is taken as 0 while $a_s$ is taken as 0 in case of one of the plots (black solid curve) and $-0.9$ radian in case of the other (red dotted curve). It is observed that the plot with $a_s = 0$ passes through the $a_v = 0$ point of the $a_v$

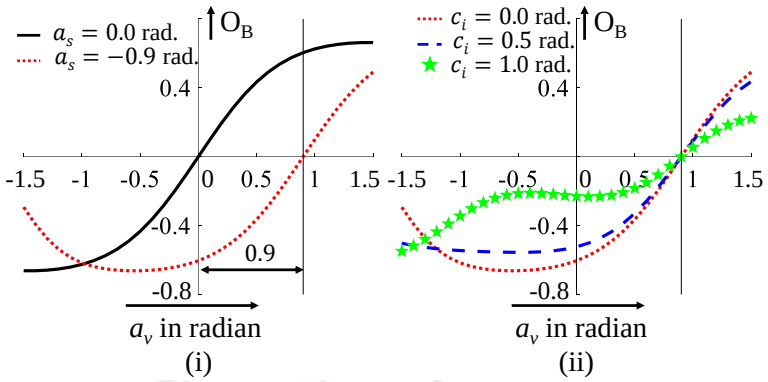


**Figure 6.1:** Plots of $O_B$ versus $a_v$ for the sensor mode $Z_s = Z_5$ when (i) $a_v Z_5$ (black solid curve) and $(a_v - 0.9)Z_5$ (red dotted curve) are present in the incident beam, (ii) $(a_v - 0.9)Z_5 + c_i Z_4$ is present in the incident beam.

axis while that with $a_s = -0.9$ radian passes approximately through the $a_v = 0.9$ point of the $a_v$ axis. Further, Fig. 6.1(ii) shows the plots of $O_B$ versus $a_v$ for $Z_s = Z_5$ and $a_s = -0.9$ radian in the presence of different RMS amplitude $c_i$ of the Zernike mode $Z_i = Z_4$ in the incident beam. $O_B$ versus $a_v$ plots of Fig. 6.1(ii) consists of three curves corresponding to three values of $c_i$ where the red dotted curve corresponds to $c_i = 0$ radian, the blue dashed curve corresponds to $c_i = 0.5$ radian and the green star marked curve corresponds to $c_i = 1$ radian, of $Z_i$ present in the incident beam. It is to be noted that for all the plots, the point of intersection of $O_B$ versus $a_v$ curves with the $O_B$ axis ($a_v = 0$ line) gives the value of $O_B$ of the type-B sensor in the presence of the RMS amplitude $a_s$ of the sensor mode $Z_s$ in the incident beam. From Fig. 6.1(ii) it is observed that $O_B$ at $a_v = 0$ for the Zernike mode $Z_5$ present in the incident beam, decreases when the RMS amplitude $c_i$ of the Zernike mode $Z_4$ present in the beam increases. This indicates a clear effect of the presence of inter-modal cross talk in the output of the type-B modal wavefront sensor. However, it is also observed that all the curves intersect the $a_v$ axis at the same point even though the amplitude of the input mode $Z_i$ for all the curves are different. Thus the point of intersection of $O_B$ versus $a_v$ plot with the $a_v$ axis remains same even in the presence of different amount of input modes in the incident beam. Therefore by considering the value of $a_v$ at the point of intersection to be the sensor output, we can develop an alternate way of measuring the sensor output which is immune to the presence of inter-modal cross talk [77]. To be noted that the corresponding type-B sensor output for $a_s = -0.9$ is much smaller than $a_s$ compared to the value of $a_v$ at the intersection point. Thus such an wavefront sensing scheme

will also provide superior linear response. In this chapter, with this motivation we propose a new modal wavefront sensing scheme that shows improvement in terms of inter-modal cross talk reduction and linearity enhancement. We name the proposed sensor as type-K sensor. In the next section, we develop the theoretical expressions to investigate the advantages of the type-K sensor.

## 6.3 Theoretical considerations

The improvement in terms of immunity to the presence of inter-modal cross talk and enhancement in the linear response range of the proposed type-K sensor can be established theoretically [78]. For this purpose, we first expand the exponential term on the RHS of Eq. 6.1 using Taylor series. Taking $I_o = 1$ we can thus write

$$\begin{aligned} Ia, c &= \left[\frac{1}{\pi^2}\iint\left(1 + iaZ_s + icZ_i - \frac{a^2}{2}Z_s^2 - \frac{c^2}{2}Z_i - acZ_sZ_i^2\right)rdrd\theta\right] \\ &\times \left[\frac{1}{\pi^2}\iint\left(1 - iaZ_s - icZ_i - \frac{a^2}{2}Z_s^2 - \frac{c^2}{2}Z_i - acZ_sZ_i^2\right)rdrd\theta\right] \end{aligned} \quad (6.6)$$

The above equation is valid under the assumption that, for most of $Z_s$, $Z_i$ or combinations of $Z_s$ and $Z_i$, the integrations $\iint Z_s^n rdrd\theta$, $\iint Z_i^m rdrd\theta$ and $\iint Z_s^n Z_i^m rdrd\theta$ are negligible for $n$, $m$ and $(n+m)$ greater than 2, respectively. Also, if the integrations for certain $Z_s$, $Z_i$ or their combinations are not negligible, they are subject to the condition that the values of $|a|$ and $|c|$ are small, so that their higher powers are negligible. Now under these assumptions and utilizing the properties of the Zernike polynomials given in Chapter 2 we can write

$$I(a, c) = 1 - a^2 - c^2 \quad (6.7)$$

Now, the central intensity at the focal point of the positive bias beam after the introduction of the variable amplitude ($a_v$) of the sensor mode can be expressed as $I(a_s + a_v + b, c_i)$. $I(a_s + a_v + b, c_i)$ can be further expanded by using the Taylor series expansion. The Taylor series expansion of a function $f(x_1 + a_1, ..., x_n + a_n)$ can be written as,

$$f(x_1 + a_1, ..., x_n + a_n) = \sum_{j=0}^{\infty}\left[\frac{1}{j!}\left(\sum_{k=1}^{n} a_k\frac{\delta}{\delta x_k'}\right)^j f(x_1', ..., x_n')\right]_{x_1'=a_1,...,x_n'=a_n} \quad (6.8)$$

Expanding $I(a_s + a_v + b, c_i)$ by using Eq. 6.8 we get

$$\begin{aligned} I(a_s + a_v + b, c_i) &= I(b,0) + (a_s + a_v)\frac{\delta I}{\delta a}\Big|_{a=b,c=0} + (c_i)\frac{\delta I}{\delta c}\Big|_{a=b,c=0} \\ &+ \frac{1}{2}(a_s + a_v)^2\frac{\delta^2 I}{\delta a^2}\Big|_{a=b,c=0} + \frac{1}{2}(c_i)^2\frac{\delta^2 I}{\delta c^2}\Big|_{a=b,c=0} \\ &+ \frac{1}{2}(a_s + a_v)c_i\frac{\delta^2 I}{\delta a \delta c}\Big|_{a=b,c=0} + \frac{1}{2}(a_s + a_v)c_i\frac{\delta^2 I}{\delta c \delta a}\Big|_{a=b,c=0} \\ &+ \ldots \end{aligned} \tag{6.9}$$

where $a$ and $c$ are independent variables that represent the coefficients of $Z_s$ and $Z_i$, respectively, whereas $a_s$, $a_v$ and $b$ are specific values of $a$ and $c_i$ is a specific value of $c$. Similarly, the central intensity at the focal point of the negative bias beam can be expressed as,

$$\begin{aligned} I(a_s + a_v - b, c_i) &= I(-b,0) + (a_s + a_v)\frac{\delta I}{\delta a}\Big|_{a=-b,c=0} + (c_i)\frac{\delta I}{\delta c}\Big|_{a=-b,c=0} \\ &+ \frac{1}{2}(a_s + a_v)^2\frac{\delta^2 I}{\delta a^2}\Big|_{a=-b,c=0} + \frac{1}{2}(c_i)^2\frac{\delta^2 I}{\delta c^2}\Big|_{a=-b,c=0} \\ &+ \frac{1}{2}(a_s + a_v)c_i\frac{\delta^2 I}{\delta a \delta c}\Big|_{a=-b,c=0} + \frac{1}{2}(a_s + a_v)c_i\frac{\delta^2 I}{\delta c \delta a}\Big|_{a=-b,c=0} \\ &+ \ldots \end{aligned} \tag{6.10}$$

Now, evaluating the partial derivatives on the RHS of Eqs. 6.9 and 6.10 by substituting $Ia, c$ of Eq. 6.7 we get

$$I(a_s + a_v + b, c_i) = I(b,0) + (a_s + a_v)(-2b) - (a_s + a_v)^2 - c_i^2 \tag{6.11}$$

and

$$I(a_s + a_v - b, c_i) = I(b,0) + (a_s + a_v)(2b) - (a_s + a_v)^2 - c_i^2 \tag{6.12}$$

Considering that an external agency changes the value of $a_v$ until the output of the type-B sensor vanishes ($O_B = 0$). Taking the value of $a_v$ for which $O_B = 0$ as $a_{v0}$, we can write

$$I(a_s + a_{v0} + b, c_i) - I(a_s + a_{v0} - b, c_i) = 0 \tag{6.13}$$

Solving Eq. 6.13 by substituting Eqs. 6.11 and 6.12 we get

$$(a_s + a_{v0})(4b) = 0 \tag{6.14}$$

Since the bias amplitude $b \neq 0$, the only solution of the above equation is

$$a_s = -a_{v0} \tag{6.15}$$

Equation 6.15 indicates a linear dependence of $a_s$ on $a_{v0}$, which is the point of intersection of the $a_v$ axis with the $O_B$ versus $a_v$ plot. Thus, the sensor output which is also the $\Phi_{RMS}$ estimated by the proposed type-K modal wavefront sensor can be expressed as,

$$O_K = -a_{v0} = \Phi_{RMS}(\text{type-K}) \tag{6.16}$$

It is to be noted that the value of $(a_s + a_{v0})$ is small near the point of intersection. Hence, the assumptions considered for obtaining the expression of $Ia, c$ described by Eq. 6.6 holds even for Eqs.6.9 and 6.10 and also for any values of $a_s$. This indicates that the linear dependence shown in Eq. 6.15 holds for any values of $a_s$.

From Fig. 6.1(i) it is seen that near the point of intersection $a_{v0}$, the $O_B$ versus $a_v$ plot appears to be a straight line. Therefore the value of $a_{v0}$ can also be estimated through linear interpolation between two nearby values of $a_v$ corresponding to the type-B sensor outputs $O_B$ with opposite signs. Thus, in order to execute the type-K sensor for measuring the strength of the sensor mode $(a_s = -a_{v0})$ present in the incident beam one requires a means to add two different $a_v$ values of the sensor mode, say $a_{v1}$ and $a_{v2}$, such that $O_K(a_v = a_{v1}) \times O_K(a_v = a_{v2})<0$. The present chapter includes two different schemes of obtaining $a_{v0} = a_s$.

The Taylor series expansion in Eqs. 6.6, 6.9 and 6.10 is restricted up to the second order terms, resulting in the absence of any $c_i$ dependent terms in Eq. 6.14. But when Eqs. 6.6, 6.9 and 6.10 are extended up to the third order terms, $c_i$ dependent terms are present in Eq. 6.14. Now, retaining up to the third order terms of the taylor series expansion, Eq. 6.6 can be expressed as,

$$\begin{aligned} I(a,c) &= \left[1 - \frac{a^2}{2} - \frac{c^2}{2} - \frac{i}{6}\left(a^3\left\langle Z_s^3\right\rangle + 3a^2c\left\langle Z_s^2 Z_i\right\rangle + 3ac^2\left\langle Z_s Z_i^2\right\rangle + c^3\left\langle Z_i^3\right\rangle\right)\right] \\ &\times \left[1 - \frac{a^2}{2} - \frac{c^2}{2} + \frac{i}{6}\left(a^3\left\langle Z_s^3\right\rangle + 3a^2c\left\langle Z_s^2 Z_i\right\rangle + 3ac^2\left\langle Z_s Z_i^2\right\rangle + c^3\left\langle Z_i^3\right\rangle\right)\right] \end{aligned} \tag{6.17}$$

Substituting Eq. 6.17 in Eqs. 6.9 and 6.10 again taking up to the third order terms, Eq. 6.14 takes the form

$$\begin{aligned}
&( \quad a_s + a_{v0})(4b) + \frac{1}{3}b^5 c_i \left\langle Z_s^3 \right\rangle \left\langle Z_s^2 Z_i \right\rangle + \frac{1}{9}b^3 c_i^3 \left\langle Z_s^3 \right\rangle \left\langle Z_i^3 \right\rangle + b^3 c_i^3 \left\langle Z_s^2 Z_i \right\rangle \left\langle Z_s Z_i^2 \right\rangle \\
&+ \quad \frac{10}{3}(a_s + a_{v0})^2 b^3 \left\langle Z_s^3 \right\rangle \left\langle Z_s^2 Z_i \right\rangle + 2(a_s + a_{v0}) b^3 c_i^2 \left\langle Z_s^2 Z_i \right\rangle^2 \\
&+ \quad \frac{4}{3}(a_+ a_{v0}) b^3 c_i^2 \left\langle Z_s^3 \right\rangle \left\langle Z_s Z_i^2 \right\rangle + (\text{terms independent of } c_i) = 0 \qquad (6.18)
\end{aligned}$$

The output of type-A and type-B sensor is proportional to $I(a_s + b, c_i) - I(a_s - b, c_i)$, which is similar to the left hand side (LHS) of Eq. 6.18 at $a_{v0} = 0$. Therefore, the output of the type-A and type-B sensors are affected by six $c_i$ dependent terms when the Taylor series expansion retains up to the third order terms. However, $(a_s + a_{v0})$, in case of the type-K sensor, near the point of intersection of the $O_B$ versus $a_v$ plot with the $a_v$ axis vanishes or is very small . Therefore the output of type-K sensor is effectively influenced by only three $c_i$ dependent terms when the type-A or type-B sensors are affected by six $c_i$ dependent terms. This indicates a reduction in the effect of inter-modal cross talk in a type-K sensor compared to the type-A and type-B sensor.

## 6.4 Type-K sensor output using bisection method

As stated already by using Eq. 6.1, one can calculate the central intensities $I(a_s + b, c_i)$ and $I(a_s - b, c_i)$ of the two bias beams at the focal plane of a basic modal wavefront sensor setup. The calculated intensities for a certain combination of $a_s$ and $c_i$ are then used to obtain the outputs of a type-A $(O_A)$ and a type-B $(O_B)$ sensor for a known bias value $b$ using Eqs. 6.2 and 6.3, respectively. We calculate $O_A$ and $O_B$ keeping the bias value $b = 0.7$ radian (chosen for maximum sensitivity of the basic sensor) and considering the incident beam to contain only $a_s$ amount of the sensor mode $Z_s$ $(c_i = 0)$. The calculated value of $O_A$ and $O_B$ are then used to estimate $\Phi_{RMS}$ for both the type-A and type-B sensors using Eqs. 6.4 and 6.5, respectively. The calculations are carried out for $Z_s = Z_4 \rightarrow Z_{11}$ with $a_s$ varying from -1.5 radians to +1.5 radians at a step of 0.1 radian.

We have discussed in the previous section that the type-K sensor output corresponds to the negative of the root $a_{v0}$ of the equation $O_B(a_v) = 0$. The root of the equation on the other hand can be estimated using a root finding algorithm such as

bisection method [79]. In the bisection method we first assume two guess values of $a_v$, say $a_{v1}$ and $a_{v2}$ such that $O_B$ at $a_v = a_{v1}$ and $a_v = a_{v2}$ has opposite signs. $O_B$ is then estimated at $a_{v3} = \frac{a_{v1}+a_{v2}}{2}$ and based on the sign of $O_B$ $a_{v3}$ replaces the guess root with equivalent sign. The process is repeated till we reach a $a_v = a_{v0}$ at which $O_B$ approaches zero and we consider $O_K = -a_{v0}$.

We perform numerical simulation of the type-A, type-B and type-K sensors. Type-K sensor output is obtained using the bisection method for each value of $a_s$ as it varies from -1.5 radians to +1.5 radians. We take $-1.5$ radian and 1.5 radian as the initial guess roots and the bisection method is operated for 10 iterations. $\Phi_{RMS}$ is then estimated for all the three sensors. Figures 6.2(i $\rightarrow$ iii) show the plot of $\Phi_{RMS}$ versus RMS amplitude of the sensor mode $a_s$ of type-A, type-B and type-K sensors, respectively. The red, black, blue, cyan, magenta and green curves represent the $\Phi_{RMS}$ versus $a_s$ plots when only the sensor mode is present. We use $Z_s$=$Z_4$, $Z_{5,6}$, $Z_{7,8}$, $Z_{9,10}$ and $Z_{11}$. It is observed that the plots of the type-A sensor (Fig. 6.2(i)), show linear response between $a_s$=$-0.3$ radian to 0.3 radian, while a type-B sensor (Fig. 6.2(ii)) shows linear response between $a_s$=$-0.4$ radian to 0.4 radian. However, Fig. 6.2(iii) indicates that the linear range for the various sensor modes in the case of the type-K sensor extends for the entire range of the RMS amplitude $a_s$ of the sensor modes considered in the simulation. Thus, the proposed type-K sensor shows improvement in linear response without compromising the sensitivity.

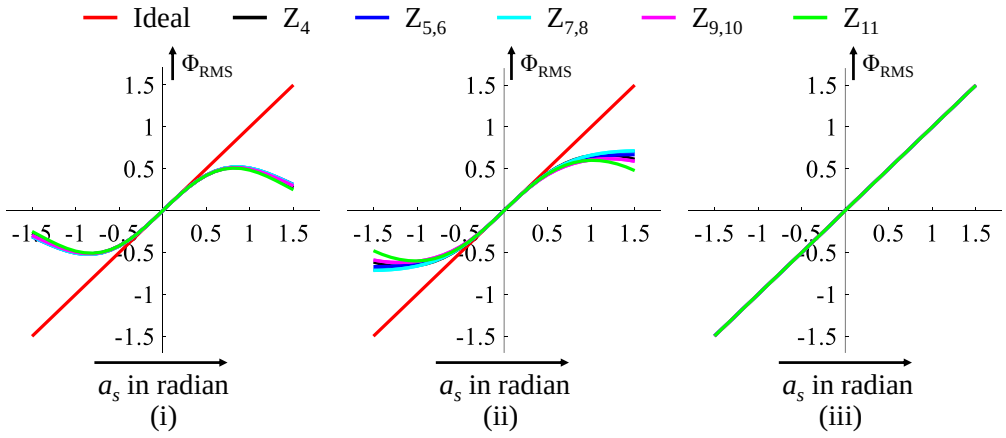


**Figure 6.2:** Simulated plots of $\Phi_{RMS}$ versus $a_s$ of the ideal output (red) and the sensor modes $Z_4$ (black), $Z_5, Z_6$ (blue), $Z_7, Z_8$ (cyan), $Z_9, Z_{10}$ (magenta) and $Z_{11}$ (green) for (i) type-A, (ii) type-B and (iii) type-K sensors.

We further investigate the effect of inter-modal cross talk on the type-K sensor in the presence of various input modes $Z_i$ in addition to the sensor modes $Z_s$. For

this purpose, we consider that the incident beam contains $a_s = 0.3$ radian of $Z_s$, where $s = 4, 5, 7, 9, 11$, and a variable $c_i$ amount of $Z_i$, where $i = 11, 12, 16, 18, 4$, corresponding to $s = 4, 5, 7, 9, 11$ of $Z_s$, respectively. The pairs of sensor mode and input mode combinations are so chosen that the presence of the particular input mode leads to a maximum inter-modal cross talk effect on the type-A and type-B sensor for the associated sensor mode [25]. $\Phi_{RMS}$ for the three types of sensors are computed for a range of $c_i$ values varying from 0 radian to 0.3 radian in the step of 0.03 radian. Here the value of $a_s$ is so chosen that the output of both the type-A and type-B sensors lie within the linear range. The output of the type-K sensor is calculated by running the bisection method for 10 iterations and taking $+0.5$ radian and $-0.5$ radian as the initial guess root. Figures 6.3(i $\rightarrow$ v) show

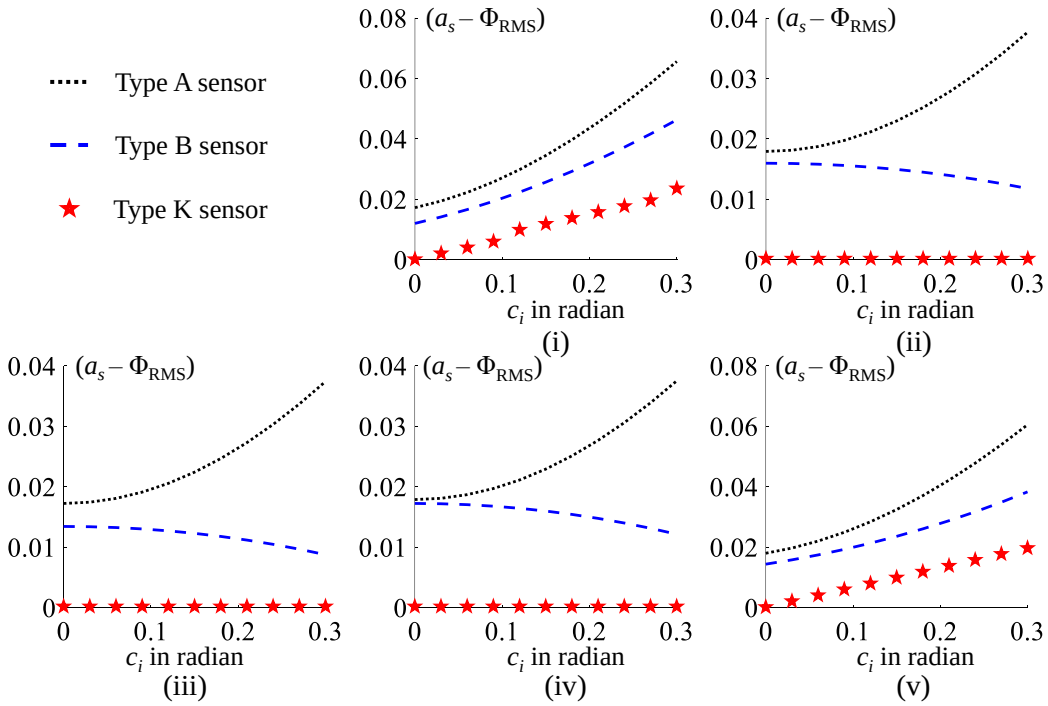


**Figure 6.3:** Simulated plots of $a_s - \Phi_{RMS}$ versus $c_i$ of type-A (black dotted curve), type-B (blue dashed curve) and type-K (red star marked curve) sensors for $(Z_s, Z_i)$ combinations: (i) $(Z_4, Z_{11})$, (ii) $(Z_5, Z_{12})$, (iii) $(Z_7, Z_{16})$, (iv) $(Z_9, Z_{18})$ and (v) $(Z_{11}, Z_4)$. Here, $a_s = 0.3$ radian and $b = 0.7$ radian.

the plot of $(a_s - \Phi_{RMS})$ versus $c_i$ for $(Z_s, Z_i)$ pairs $(Z_4, Z_{11})$, $(Z_5, Z_{12})$, $(Z_7, Z_{16})$, $(Z_9, Z_{18})$ and $(Z_{11}, Z_4)$, respectively. The black dotted, the blue dashed and the red star marked curves represent the $a_s - \Phi_{RMS}$ versus $a_s$ plots of type-A, type-B and type-K sensors. In the ideal case where the sensor output is perfectly immune to the inter-modal cross talk and the sensor detects the exact amount $(a_s)$ of the sensor

mode, the value of $a_s - \Phi_{RMS}$ is zero for any value of $c_i$. It is observed that, for the pairs $(Z_4, Z_{11})$ and $(Z_{11}, Z_4)$, the output of all the three types of sensors (type-A, type-B and type-K) show the effect of inter-modal cross talk. However, the type-K sensor is observed to be highly immune to the inter-modal cross talk for the rest of the pairs $((Z_5, Z_{12})$, $(Z_7, Z_{16})$ and $(Z_9, Z_{18}))$ compared to type-A and type-B sensors.

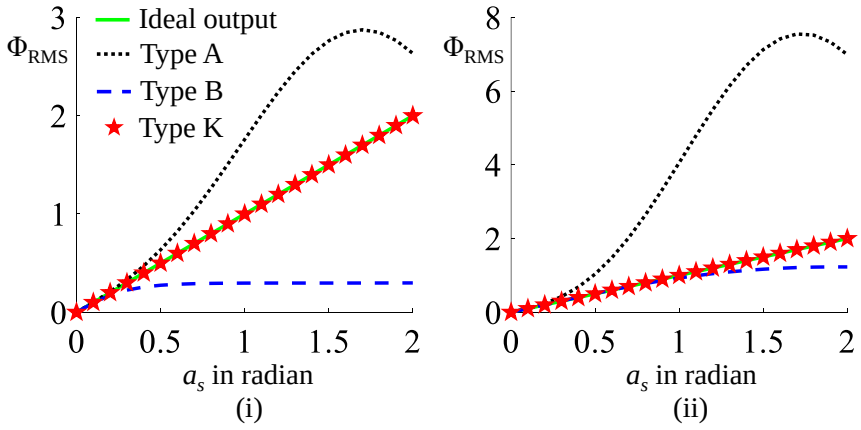


**Figure 6.4:** Simulated plots of $\Phi_{RMS}$ versus $a_s$ of the ideal value of $\Phi_{RMS}$ (green solid curve), type-A (black dotted curve), type-B (blue dashed curve) and type-K (red star marked curve) sensors for (i) $Z_s = Z_5$ and (ii) $Z_s = Z_{11}$. For type-A and type-B sensor $b = 1.7$ radian while for type-K sensor $b = 0.7$ radian.

In the above investigations, the output of all the three types of sensors are calculated for a fixed bias value $b = 0.7$ radian that is optimized for maximum sensitivity. Investigations are also carried out to check if the performance of type-A and type-B sensors can be improved by using a higher bias value. We investigate the linear response of the type-A and type-B sensor for the bias value $b = 0.7 + a_v$. Thus the output of type-A and type-B sensors are calculated using $b = 1.7$ radian ($a_v = 1$) while the output of the type-K sensor is computed using $b = 0.7$ radian. Figures 6.4(i) and (ii) show the plot of $\Phi_{RMS}$ versus $a_s$ of the three type of sensors for the sensor modes $Z_5$ and $Z_{11}$, respectively, when no input mode ($c_i = 0$) is present in the incident beam. In both the figures, $\Phi_{RMS}$ correspond to $a_s$ ranging from 0 radian to 2 radians and the bisection method to calculate the output of the type-K sensor is operated for 10 iterations taking $-2.5$ radian and 2.5 radian as the initial guess roots. In Fig. 6.4 the green solid, black dotted, blue dashed and red star marked curves represent the ideal value of $\Phi_{RMS}$ and $\Phi_{RMS}$ calculated for type-A, type-B and type-K sensors. It is observed that an increase in the bias value ($b = 1.7$ radian) does not improve the linear response range of the type-A and type-

B sensors assigned for the sensor mode $Z_5$. However, the type-B sensor assigned for the sensor mode $Z_{11}$ shows some improvement (although less than that of the type-K sensor) in the linear response range and no improvement is seen in the case of type-A sensor assigned for the same mode. Thus, a mere increase in the bias value does not increase the linear response range of type-A and type-B sensor. The enhancement of the linear response of the type-K sensor comes from its inherent characteristic indicated in Eq. 6.15.

## 6.5 Estimation of type-K sensor output from a minimal set of fixed $a_v$ values

The bisection method used above to find the point of intersection of $O_B$ versus $a_v$ plot with the $a_v$ axis requires the introduction of a variable RMS amplitude $a_v$ of the sensor mode. Further, in the case of the measurement of an unknown phase, the required value of $a_v$ for each iteration cannot be known in advance. Thus the experimental implementation of the type-K sensor requires a dynamic phase manipulating device that can incorporate the required RMS amplitude $a_v$ of the sensor mode into the incident beam. Moreover, the iterative operation of the phase modulating device slows down the process of estimation of the aberration. However, it is observed that near the point of intersection $a_{v0}$ the plot of $O_B$ versus $a_v$ approximates a straight line (Fig. 6.1(i)). This opens a possibility of finding $a_{v0}$, up to a reasonable accuracy, with the help of few fixed values of $a_v$ and performing a linear interpolation between two adjacent values that correspond to $O_B$ values with opposite signs. The steps to be followed for obtaining the unknown strength $a_s$ of the sensor mode $Z_s$ present in the incident beam by using a few fixed values of $a_v$ is described below.

1. The $a_v$ values are first chosen, say five values of $a_v$ [-2, -1, 0, 1, 2].

2. Corresponding to the five $a_v$ values, the phase profile $\Phi$ of the incident beam is modified as $\Phi \rightarrow \Phi' = \Phi - 2Z_s, \Phi - Z_s, \Phi, \Phi + Z_s, \Phi + 2Z_s$.

3. The output of the type-B sensor $O_B$ is estimated for all the five modified phase profiles present in the beam incident on the sensor.

4. If $O_B$ at $a_v = 0$ is zero ($O_B|_{a_v=0} = 0$) then $a_{v0} = 0$.

5. If $O_B|_{a_v=0} > 0$, $a_{v0}$ lies towards the negative $a_v$ values ($a_{v0} < 0$), within the interval $[a_v = 0, a_v = -1]$ or $[a_v = -1, a_v = -2]$

   (a) If $(O_B|_{a_v=0} \times O_B|_{a_v=-1}) < 0$, $a_{v0}$ lies in the interval $[a_v = 0, a_v = -1]$. Thus $a_{v0}$ is calculated through a linear interpolation between $O_B|_{a_v=0}$ and $O_B|_{a_v=-1}$.

   (b) or if $(O_B|_{a_v=-1} \times O_B|_{a_v=-2}) < 0$, $a_{v0}$ lies in the interval $[a_v = -1, a_v = -2]$. Thus $a_{v0}$ is calculated through a linear interpolation between $O_B|_{a_v=-1}$ and $O_B|_{a_v=-2}$.

6. If $O_B|_{a_v=0} < 0$, $a_{v0}$ lies towards the positive $a_v$ values ($a_{v0} > 0$), within the interval $[a_v = 0, a_v = 1]$ or $[a_v = 1, a_v = 2]$

   (c) If $(O_B|_{a_v=0} \times O_B|_{a_v=1}) < 0$, $a_{v0}$ lies in the interval $[a_v = 0, a_v = 1]$. Thus $a_{v0}$ is calculated through a linear interpolation between $O_B|_{a_v=0}$ and $O_B|_{a_v=1}$.

   (d) or if $(O_B|_{a_v=1} \times O_B|_{a_v=2}) < 0$, $a_{v0}$ lies in the interval $[a_v = 1, a_v = 2]$. Thus $a_{v0}$ is calculated through a linear interpolation between $O_B|_{a_v=1}$ and $O_B|_{a_v=2}$.

The process of finding the value of $a_{v0}$ described above requires a minimum of two values of $a_v$ such that $a_{v0}$ lies between them. The accuracy of the sensor output of such a sensor depends on the proximity of the nearest guess root to the RMS amplitude $a_s$ of the sensor mode. However, if the intersection of $O_B$ versus $a_v$ plot with the $a_v$ axis occurs at multiple locations, say $a_{v0}$ and $a_{v0'}$, and $|a_{v0}| > |a_{v0'}|$, the type-K sensor gives wrong result.

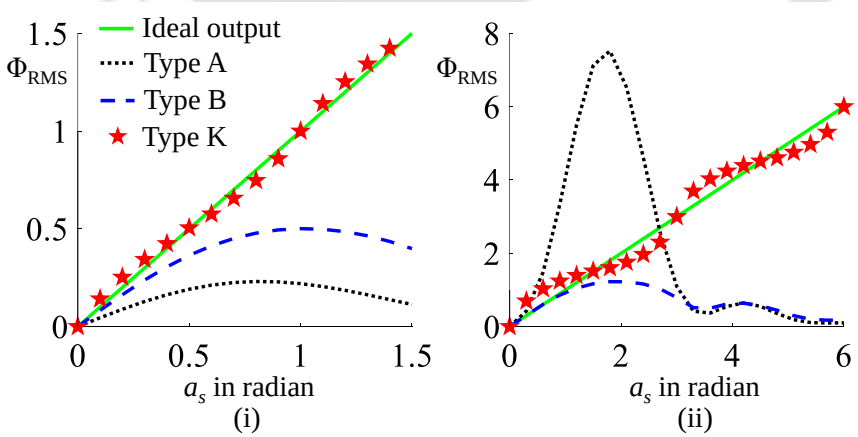


**Figure 6.5:** Simulated plots of $\Phi_{RMS}$ versus $a_s$ of the ideal value of $\Phi_{RMS}$ (green solid curve), type-A (black dotted curve), type-B (blue dashed curve) and type-K (red star marked curve) sensors for $Z_s = Z_{11}$ using (i) $b = 0.7$ radian and (ii) $b = 1.7$ radian.

The proposed scheme of using a few fixed values of $a_v$ to find the output of the type-K sensor is demonstrated through numerical simulations. Here we choose $a_v = [-2, -1, 0, 1, 2]$ and follow the above steps to calculate the type-K sensor output for the sensor mode $Z_s = Z_{11}$. The RMS amplitude $b$ of the bias is taken as 0.7 radian while the RMS amplitude $a_s$ of the sensor mode varies from 0 to 1.5 radians. The output of type-A and type-B sensors are also calculated for the same $Z_s$, $b$ and $a_s$. The resulting plots of $\Phi_{RMS}$ versus $a_s$ are shown in Fig. 6.5(i). The figure indicates that the type-K sensor shows a linear response over the whole range of $a_s$ with a standard deviation of 0.037 radian relative to the ideal output whereas the linear response range in case of the type-A and type-B sensors lag way behind the type-K sensor. The linear response range of a type-K sensor can be further enhanced by using a higher bias value of $b$. Figure 6.5(ii) shows the plot of $\Phi_{RMS}$ versus $a_s$ of the three type of sensors for $Z_s = Z_{11}$, $b = 1.7$ radian and $a_s = 0 \rightarrow 6$ radian. Here the output of type-K sensor is calculated by taking $a_v = [-6, -3, 0, 3, 6]$. From Fig. 6.5(ii) it is clear that by increasing the bias to $b = 1.7$ radian, the linear response range of the type-K sensor can be extended up to 6 radian (with a standard deviation of 0.3 radian relative to the ideal output). Such a linear response range cannot be achieved in case of a type-A or type-B sensor.

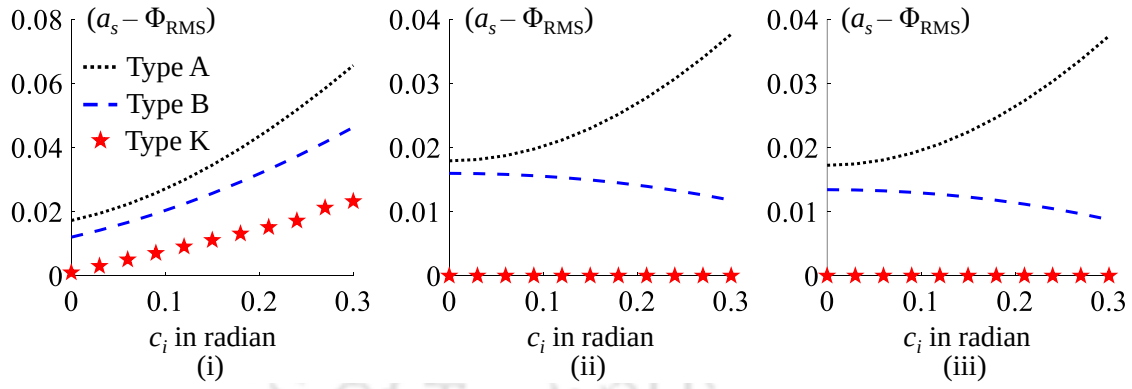


**Figure 6.6:** Simulated plots of $a_s - \Phi_{RMS}$ versus $c_i$ of type-A (black dotted curve), type-B (blue dashed curve) and type-K (red star marked curve) sensors for the $(Z_s, Z_i)$ combinations: (i) $(Z_4, Z_{11})$, (ii) $(Z_5, Z_{12})$ and (iii) $(Z_7, Z_{16})$. Here $a_s = 0.3$ radian, $b = 0.7$ radian.

Numerical simulations are also carried out to assess the effect of inter-modal cross talk on the type-K sensor output estimated using the above scheme of fixed number of $a_v$ values ($a_v$=$[-0.4, -0.2, 0, 0.2, 0.4]$). Similar to that of Figs. 6.3(i $\rightarrow$ iii), Figs. 6.6(i $\rightarrow$ iii) show the plots of $a_s - \Phi_{RMS}$ versus the RMS amplitude $c_i$ of

the input mode $Z_i$ for the $(Z_s, Z_i)$ combinations $(Z_4, Z_{11})$, $(Z_5, Z_{12})$ and $(Z_7, Z_{16})$, respectively. Here $b$ is taken to be 0.7 radian, $a_s$ is kept fixed at 0.3 radian, $c_i$ is varied from 0 radian to 0.3 radian. From the three figures (Figs. 6.6(i $\rightarrow$ iii) ) it is evident that the immunity of the type-K sensor towards the presence of inter-modal cross talk persists even when the estimation process involves only five values of $a_v$.

To assess the performance of the type-K sensor relative to the type-B sensor, a numerical simulation is carried out considering the presence of poisson noise in a bias orders. Figure 6.7 shows the simulation plots of the $\Phi_{RMS}$ versus the amplitude of sensor mode $a_s$ in presence of Poisson noise where the peak signal to noise ratio (PSNR)$\approx$ 40dB. From the figure it is seen that the outputs of both the type-B and

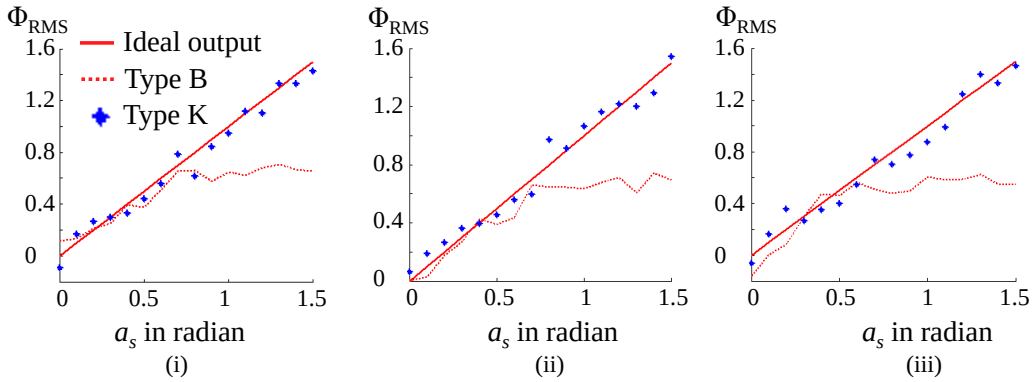


**Figure 6.7:** Simulated plots of $\Phi_{RMS}$ versus $a_s$ of the ideal value of $\Phi_{RMS}$ (red solid curve), type-B (red dotted curve) and type-K (blue star marked curve) sensors for (i) $Z_s = Z_5$, (ii) $Z_s = Z_6$ and (iii) $Z_s = Z_{11}$ in presence of poisson noise where the PSNR $\approx$ 40 dB. Here $b = 0.7$ radian.

type-K sensors show comparable effect of the noise. However, the type-K sensor still shows better linear response compared to that of the type-B sensor.

The use of only a few fixed $a_v$ values to operate the type-K sensing scheme thus eliminate the requirement of a dynamic phase or amplitude manipulating device and can be implemented using a passive (where no current and voltage source involved) optical element. This passive optical element can be a multiplex hologram in the form of a phase plate that gives rise to multiple bias orders at the focal plane of a lens placed just after it. The use of a multiplex hologram further enables the estimation of the aberration modes from a single measurement of the focal spot pattern of the bias order beams. In the next section, we demonstrate the experimental implementation of the proposed type-K sensor using such a multiplex hologram.

## 6.6 Experimental implementation of the type-K sensor

We experimentally implement the type-K sensor using binary multiplex hologram based proof of principle setup.

### 6.6.1 Multiplex hologram design for type-K sensor

The design and construction of a multiplex hologram has already been discussed in chapter 3. Let us consider a multiplex hologram that gives rise to $n$ number of $+1$ diffracted order beams such that the phase profile incorporated to the $k^{th}$ diffracted beam is $\phi_k(x,y)$. If the $k^{th}$ diffracted beam is to be sent to a location $(px_k, py_k)$ in the detector plane, the resultant complex amplitude of $n$ such diffracted beam is $A(x,y) = \sum_{k=1}^{n} exp\{i[\phi_k(x,y) + \alpha px_k x + \alpha py_k y]\}$, where $\alpha$ is a scaling factor and each of the diffracted beams is assumed to have an uniform amplitude profile. Now, for simultaneous measurement of multiple sensor modes $Z_s$ using multiple values of $a_v$ for each mode, the resultant complex amplitude profile of the diffracted beams can be represented as,

$$\begin{aligned} A(x,y) &= \sum_{k=Z_s}\sum_{k=a_v} [exp\{i[(a_v + b_k)Z_s(x,y) + \alpha px_k x + \alpha py_k y]\} \\ &+ exp\{i[(a_v - b_k)Z_s(x,y) + \alpha px'_k x + \alpha py'_k y]\}] \end{aligned} \tag{6.19}$$

Here, the two terms represent the beams with positive and negative bias. The transmittance function of the desired binary amplitude hologram (referred to as the type-K binary hologram) can now be obtained from the condition given by

$$H(x,y) = \begin{cases} 1, & \text{for} \quad \text{Real}[A(x,y)] > 0 \\ 0, & \text{otherwise} \end{cases} \tag{6.20}$$

If we take five values of $a_v$, say $[-2,-1,0,1,2]$, then for a given sensor mode $Z_s$ the type-K binary hologram gives rise to five pairs of bias order beams. If $\Phi$ is the phase profile of the incident beam, then the phase profile of the positive and negative bias order beams of each pair are $\Phi + (a_v + b)Z_s$ and $\Phi + (a_v - b)Z_s$, respectively. The type-B sensor output for each $a_v$ is obtained from the central intensities of the focal

spots of each corresponding pair of bias order beams. We have already mentioned that the type-K binary hologram can be fabricated using lithography technique, as a phase plate or can be realized using a spatial light modulating device.

### 6.6.2 Experimental arrangement

The experimental arrangement used for the implementation of the proposed type-K sensor is same as the setup shown in Fig. 5.3. The DMD has a computer interface ($PC_1$) that enables the display of a binary hologram on the DMD panel. The binary hologram is used to incorporate the desired phase profile to the +1 order beam diffracted from it. The +1 order beam then falls on a ferroelectric liquid crystal spatial light modulator (FLCSLM). A type-K binary hologram is displayed on the FLCSLM panel with the help of another computer interface ($PC_2$). The beams diffracted by the type-K hologram is then focused on the second iris diaphragm $I_2$ by a lens $L_5$. $I_2$ allows only the +1 order beams to pass through it. These beams are then focused by another lens $L_6$ on to the CMOS camera sensor that is interfaced with $PC_2$. It is to be noted that the binary holograms displayed on the DMD and the LCSLM panel are created with the help of the Labview program in $PC_1$ and $PC_2$, respectively. The Labview program in $PC_2$ is further used to process the information of the central intensities recorded by the camera to calculate the output of the type-K sensor. The phase profile carried by the +1 order beam from the DMD acts as the incident beam to the FLCSLM and the type-K sensor as well. The DMD incorporates a user-defined phase profile in terms of Zernike modes $Z_s = Z_{4\rightarrow 22}$ into the incident beam which is received by the type-K binary hologram and whose phase is to be measured. It is also to be noted that the type-K binary hologram displayed on the FLCSLM is a static pattern and the dynamic phase modulating capability of the FLCSLM is not utilized. Also, in place of a CMOS camera, the proposed sensor can make use of a number of point detectors that are appropriately positioned to measure the central intensities of the focal spots of the +1 order beams. In this case, an analogue to digital converter needs to be connected with the $PC_2$ to convert the data from the point detectors in the form of analogue signals (such as voltage or current) into digital values. The type-K binary hologram is constructed by taking $Z_s = Z_5, Z_7, Z_{11}$, $a_v = [-2. -1, 0, 1, 2]$ and $b = 0.7$ radian.

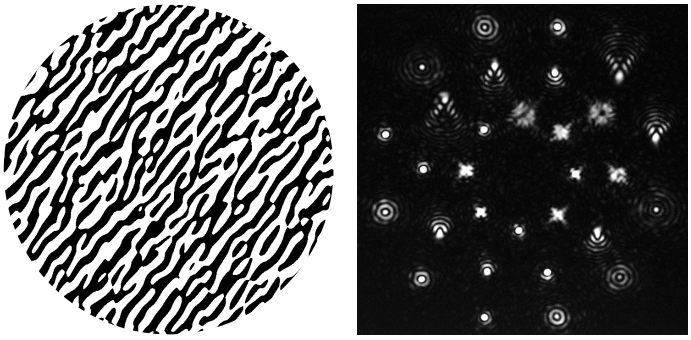

(i) (ii)

**Figure 6.8:** (i)Representative type-K binary hologram used for implementing type-K modal wavefront sensor for simultaneous detection of three sensor modes $(Z_5, Z_7, Z_{11})$ and (ii) the image of the resulting focal spot patterns captured by the CMOS camera.

### 6.6.3 Results and discussion

The binary hologram on the DMD panel is first modified to remove the residual aberrations present in the beam incident on the FLCSLM with the help of Zernike mode combinations $Z_{4\to22}$. The type-K binary hologram is designed for three sensor modes ($Z_s = Z_5, Z_7, Z_{11}$) using five $a_v$ values $(-2, -1, 0, 1, 2)$ and two bias values for each $a_v$ value. Thus the hologram gives rise to thirty +1 order beams which act as 15 pairs of bias order beams and are focused on the camera screen. Figures 6.8(i) and (ii) show a representative type-K binary hologram and the focal spot pattern as captured by the camera, respectively. The hologram is so designed that the focal spots are arranged in three concentric circles as shown in Fig. 6.8(ii). Among the focal spots, there are three pairs of bias orders, one for each sensor mode $Z_s$, for which $a_v = 0$. The central intensities of the focal spots of these three pairs of bias order beams give the output of type-A and type-B sensors for the three sensor modes. Thus the output of all the three sensors (type-A, type-B and type-K sensor) can be measured together.

An unaberrated beam falling on the camera plane has an array disk of diameter $\approx 26$ camera pixels. The central intensity of each focal spot is taken as the mean pixel value of a square area of $4 \times 4$ pixels located at the center of the focal spots. The use of a detector area of $4 \times 4$ pixels for the measurement of the central focal spot intensity to obtain the sensor output gives a reasonable signal to noise ratio compared to that of a single pixel. Also, the square area of length 4 pixels can be considered to be very small compared to that of the array disc diameter of 26 pixels.

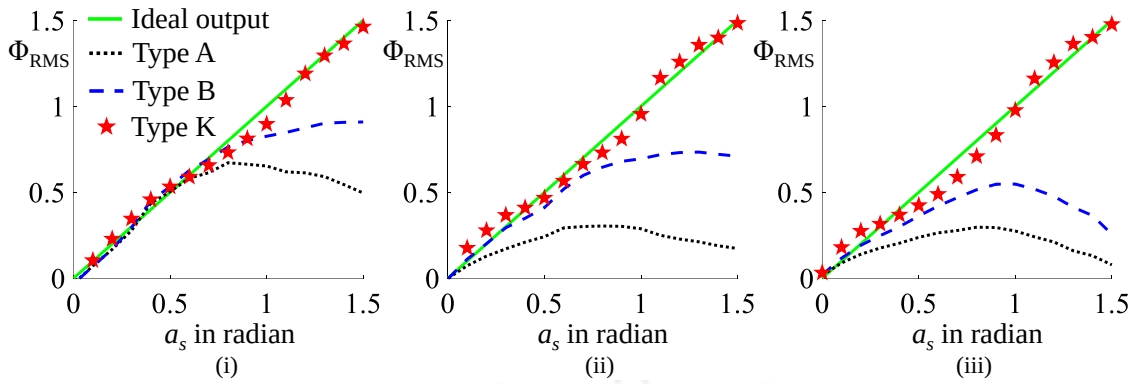


**Figure 6.9:** Experimental plots of $\Phi_{RMS}$ versus $a_s$ of the ideal value of $\Phi_{RMS}$ (green solid curve), type-A (black dotted curve), type-B (blue dashed curve) and type-K (red star marked curve) sensors for (i) $Z_s = Z_5$, (ii) $Z_s = Z_7$ and (ii) $Z_s = Z_{11}$. The RMS error of type-K sensor output is $\approx 0.053$ radian

Now using the type-K binary hologram (with $Z_s = Z_5, Z_7, Z_{11}$ and $a_v = [-2, -1, 0, 1, 2]$) displayed on the FLCSLM panel, the output of all the three sensors are measured for different RMS amplitudes $a_s$ of the sensor mode $Z_s$, with $a_s$ varying from 0 radian to 1.5 radian, in step of 0.1 radian. The incident beam with a varying phase profile $a_s Z_s$ can be achieved by updating the hologram on the DMD panel, each time a phase profile with different $a_s Z_s$ is required. The output of the three type of sensors is recorded for sensor modes $Z_s = Z_5, Z_7, Z_{11}$. Figures 6.9(i $\rightarrow$ iii) show the plot of $\Phi_{RMS}$ versus $a_s$ for the three types of sensors in the presence of Zernike modes $Z_5, Z_7$ and $Z_{11}$, respectively, in the incident beam. The figures indicate a distinct enhancement in the linear response range for the type-K sensor compared to that of the type-A and type-B sensor, especially for the large amplitude of sensor modes.

Further, to test the effect of the inter-modal cross talk on the type-K sensor, we consider an incident beam with two input modes of fixed amplitudes (1 radian of $Z_5$ and $-1$ radian of $Z_7$) apart from the sensor mode $Z_s = Z_{11}$. The type-K binary hologram at the FLCSLM panel is reconstructed for $Z_s = Z_4, Z_7, Z_{11}$ and $a_v = [-2, -1, 0, 1, 2]$. Further, the binary hologram at the DMD panel is updated so that a beam of phase profile $\Phi = a_s Z_s + Z_5 - Z_7$ is incident on the FLCSLM panel. $a_s$ is varied from 0 radian to 1.5 radian in steps of 0.1 radian and $\Phi_{RMS}$ is measured for each value of $a_s$. A numerical simulation analogous to the experiment is also carried out. Figures 6.10(i) and (ii) show the plots of $\Phi_{RMS}$ versus $a_s$ of the three sensors obtained through numerical simulation and experiment, respectively. From

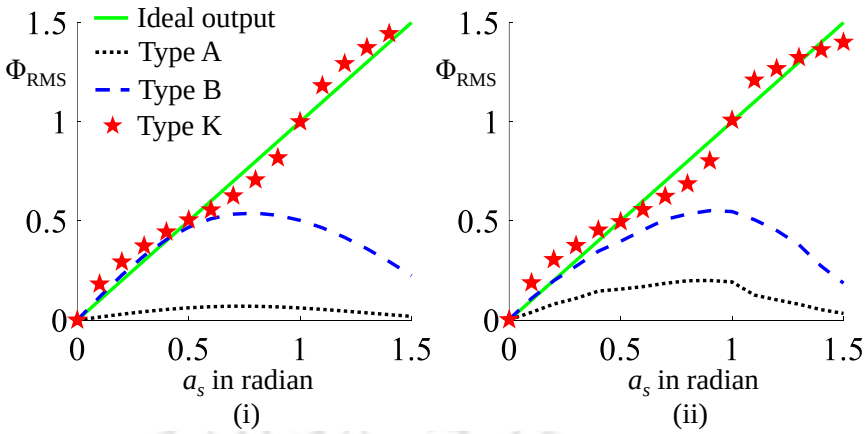


**Figure 6.10:** Experimental plots of $\Phi_{RMS}$ versus $a_s$ of the ideal value of $\Phi_{RMS}$ (green solid curve), type-A (black dotted curve), type-B (blue dashed curve) and type-K (red star marked curve) sensors for $Z_s = Z_{11}$ obtained (i) using numerical simulation and (ii) experimentally, when the incident beam has a phase profile $\phi = a_s Z_s + Z_5 - Z_7$.

the figures, it is observed that even in the presence of two input modes the type-K sensor shows a near-perfect linear response for the entire range of $a_v$ values from 0 radian to 1.5 radian with a reasonable accuracy. Thus, the type-K modal wavefront sensor shows a large improvement in the immunity to the inter-modal cross talk. However, the linear response of the type-A and type-B sensors are limited to a small range, of which the type-A sensor is the worst affected. It can also be mentioned that the experimental data agrees quite well with that of the theoretical prediction.

The DMD is then used to modify the incident beam phase profile such that the beam incident on the FLCSLM has a phase profile which is a combination of three Zernike modes. All the three Zernike modes are measured simultaneously using the relevant type-K binary hologram on the FLCSLM. Table 6.1 shows the measured $\Phi_{RMS}$ of the three types of sensors for two Zernike mode combinations, $(Z_5, Z_7, Z_9)$ and $(Z_4, Z_6, Z_8)$, as the incident beam phase profile. The type-K binary hologram is generated for the respective $Z_s$ combinations and taking $a_v = [-2, -1, 0, 1, 2]$. From the table, it is evident that the type-K sensor gives a more accurate estimate of the incident beam phase profile compared to that of the type-A and type-B sensors. The table also indicates a lesser effect of inter-modal cross talk in the case of the type-K sensor compared to the other two sensors.

The values of $\Phi_{RMS}$ obtained from the experimental investigations indicate a small amount of disagreement from that of the expected values. This disagreement can be attributed to the limited number of pixels of the FLCSLM, which in turn

**Table 6.1:** Table showing the experimentally estimated $\Phi_{RMS}$ (in radian) for type-A, type-B and type-K sensors for a linear combination of three Zernike modes as the incident beam phase profile.

| **Sensor modes $Z_s$** | **(5, 7, 9)** | **(4, 6, 8)** |
|---|---|---|
| $a_s$ | (0.5, 0.5, -1) | (0.5, -1, 0) |
| $\Phi_{RMS}$(type-A) | (0.08, 0.20, -0.35) | (0.10, -0.24, 0.02) |
| $\Phi_{RMS}$(type-B) | (0.17, 0.43, -0.48) | (0.30, -0.59, 0.06) |
| $\Phi_{RMS}$(type-K) | (0.30, 0.43, -1.11) | (0.44, -0.74, -0.10) |

limits the number of pixels defining the multiplex hologram, leading to inaccuracy in the complex amplitude profile of the bias order beams. Further, the inaccuracy in the experimental measurement can be due to the finite number of gray levels of the CMOS camera that leads to inaccuracy in finding the point of intersection $a_{v0}$ from the basic type-B sensor output. In our case, $a_{v0}$ may lie in a range of about $-0.03$ radian to 0.03 radian, thus incorporating inaccuracy in measurement. Moreover, the residual aberration of the partially corrected beam and background noises also affect the measurements.

The results obtained from the experimental investigation validate that the proposed type-K sensor gives an excellent linear response even for the larger amplitude of the sensor modes and also is highly immune to the presence of a few low order aberration modes in the incident beam. While measuring the large amplitude of aberration modes, the proposed sensor requires only one camera image of the focal spot pattern. In contrast the type-A and type-B modal wavefront sensors will require a dynamic phase correcting mechanism and capturing of multiple camera images for just one measurement. Thus, a passive wavefront modulating device such as a phase plate serves the purpose for a type-K modal wavefront sensor whereas an active (a voltage or current controlled) wavefront modulating device is required in case of a type-A or type-B modal wavefront sensor, when the sensor mode has a large amplitude..

In all the above experimental implementations of type-K modal wavefront sensor above, the type-K binary hologram employs five fixed $a_v$ values (say $[-2, -1, 0, 1, 2]$). However, for the smaller amplitude of aberration modes (limited to $\pm 1$ radian), the same level of accuracy can be achieved by reducing the number of $a_v$ values to three (say $[-1, 0, 1]$). Further to cope with applications having extremely low light or

require low incident light, one can reduce the number of sensor modes used while computing the hologram or can increase the diffraction efficiency of the type-K sensor by the use of binary phase hologram or blazed grating hologram.

## 6.7 Conclusion

In this chapter, we have introduced a new modal wavefront sensing scheme that provides an enhancement in the linear response range and improvement in the immunity from inter-modal cross talk. The proposed sensor exhibits superior performance without any compromise of its speed and sensitivity. The enhancement in the linear response and the immunity from the inter-modal cross talk have been established theoretically. Further, the performance of the proposed sensor has been assessed through numerical simulation. Towards the later part of the chapter, we have discussed the experimental implementation of the new modal wavefront sensor using LCSLM that displays a binary multiplex hologram through a computer interface. However, a passive optical element such as a phase plate can also serve the purpose. The multiplex hologram is used to simultaneously measure three aberration modes from just one measurement of the focal spot intensity data. It has also been discussed that the number of aberration modes can be increased or decreased according to the requirement of the application and the configuration of the LCSLM and camera used. Experimental results have also been provided towards the end of the chapter to validate the improvement of the proposed wavefront sensor in terms of linear response and inter-modal crosstalk.

# Chapter 7

# Application of type-K Sensor in Free Space Optical Communication

## 7.1 Introduction

Free space optical communication (FSOC) system uses a laser beam to carry the user information from the transmitting station to the receiving station through a certain path in the free space. FSOC links can be established between satellites, satellite to airborne, underwater, ground based and water surface based platforms, and mobile or stationary platforms within the atmosphere [80]. Due to the high frequency in the range $\approx 400-800$ THz of optical signals compared to the frequency of $\approx$ 30 Hz - 300 GHz in case of an radio frequency (RF) signal, the optical communication link can achieve a data rate as high as $\approx$ 100 Gb/s compared to a data rate of $\approx$ 300 Mb/s in case of an RF communication link [81]. Further, due to the low beam divergence of the optical beams compared to the RF beam, an optical communication link can achieve a higher data rate even with a smaller antenna size compared to that of the RF communication link [81, 82]. It therefore reduces the power consumption and cost while setting up an optical communication link. The free space communication links have been demonstrated successfully in the laboratory, in the atmosphere and in the space [80, 83].

However, it is observed that if the free space link is established through a turbulent atmosphere it may lead to severe perturbation of the phase and scintillation of the intensity of the optical signal in the pupil of the receiver of the communication

system [84]. Such distortion of the optical signal can be compensated with the help of adaptive optics correction at the receiving end [13, 85]. Another important issue of a free space optical communication system is the extent of information security the communication system provides from eavesdropper or intruders [86]. Efforts are also made to secure the information of an optical communication link by adopting various cryptographic techniques [87, 88, 89]. The introduction of the optical angular momentum (OAM) states as the encoding parameter has further upgraded the FSOC system [90]. There are reports of achieving a very high data rate through OAM multiplexing in a FSOC system [91, 92]. However, beam with OAM states, if travels through turbulent atmosphere, gets severely effected resulting in vortex instability [93].

In this chapter we introduce the use of Zernike aberration modes to encode the phase profile of a laser beam which then travels through certain space in the laboratory environment. The beam is incident on a type-K sensor at the receiving station which decodes the information. We show that one can use not just different aberration modes but different strengths of the same mode to encode the laser beam in the transmission station. We also develop a scheme to compensate the effect of external perturbations. In this chapter we describe a proof of concept experimental setup and some results obtained using the setup.

## 7.2 Basic operations of the wavefront encoded free space communication system

We first discuss the basic building blocks comprising a free space line of sight optical communication system using a Zernike mode encoded laser beam and their operations. Figure 7.1shows a schematic of the building blocks in the receiving and transmitting stations. The user information which can be text, numbers or images are first read as an array of bytes (maximum decimal value of 255). Information which is by default in a multi dimensional array of bytes are reshaped as a one dimensional array of equal number of pixels. We employ the computer generated holography technique as described in chapter 3 to design a laser beam whose phase profile carries a linear combination of one or more number of specific Zernike modes. The co-efficient of a Zernike mode can take certain specific values. Based of the number of Zernike modes used and the number of allowed values of the

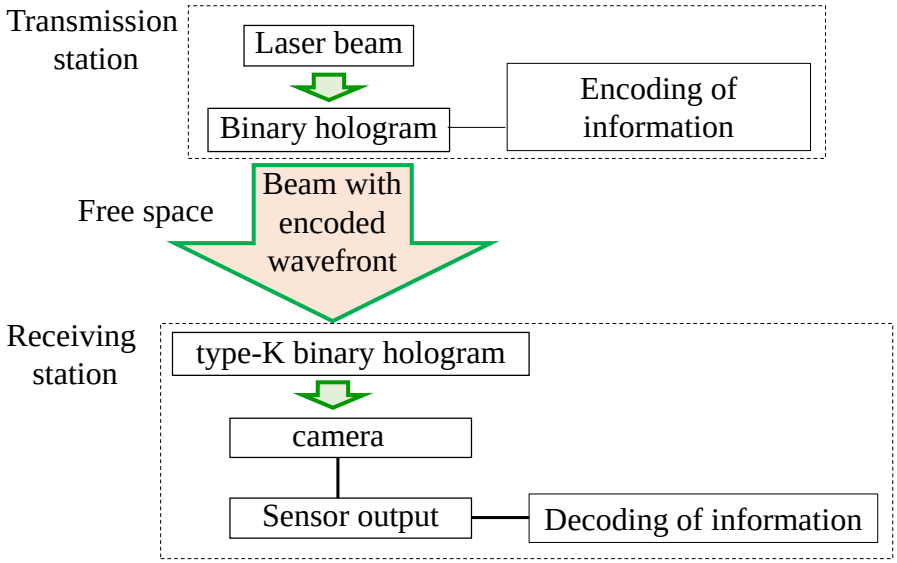


**Figure 7.1:** Schematic illustrating the basic operations of the free space optical communication system using type-K sensor in the receiving station.

co-efficients, there can be a specific (say $n$) number of different resultant wavefront of the laser beam. Thus the 8 bit user information in each pixel in decimal number system is to be converted to base-n number system. Each digit of the resulting base-n number is then used to construct a binary hologram. When a plane wavefront is incident on the binary hologram the +1 diffracted order beam carry the required resultant wavefront. After sending the wavefront corresponding to the first digit, the binary hologram is updated with a pattern corresponding to the second digit and the process continues till the whole user information is encoded.

The wavefront encoded laser beam travels a certain distance in free space before it is incident on a type-K modal wavefront sensor in the receiving station. The +1 order beams diffracted by the multiplex hologram of the type-K sensor are focused on a camera which captures at least one image for each wavefront of the incident laser beam. The RMS amplitudes $\Phi_{RMS}$ of the Zernike modes as measured by the type-K sensor are converted to the digits of a base-n number. Each base-n number is then converted to a decimal number to eventually get the user information.

## 7.3 Encoding and decoding of user data

The user information is usually available in the form of decimal numbers with the maximum size of a byte which is to be converted to a base-n number system. In the case of base-n numbers the binary hologram in the transmission station should be able to generate a +1 diffracted order beam with $n$ different phase profiles corresponding to $n$ different combination of Zernike modes. Figure 7.2 shows the conver-

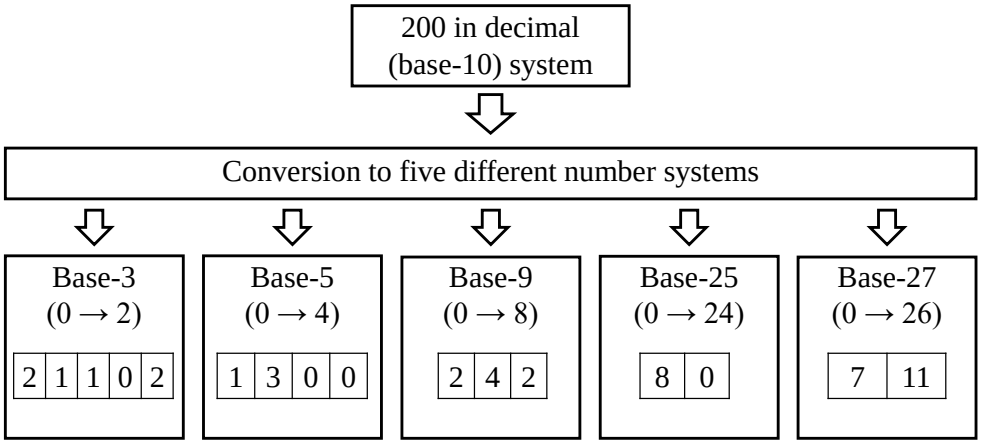


**Figure 7.2:** Conversion of a decimal number, 200, into base-3, base-5, base-9, base-25 and base-27 number systems.

sion of a decimal number, 200, into five different number systems with base 3, 5, 9, 25 and 27. It is noticed that, as the value of $n$ increases the number of digits required to describe the decimal number decreases. In order to describe the decimal number 200 the base-3 number system requires 5 digits (five different wavefronts of the laser beam) while the base-25 number system requires just 2 digits (two wavefronts of the laser beam). A 5 digit base-3 number can describe a maximum decimal number equal to 242 while a 2 digit base-25 number can describe a maximum decimal number equal to 624. The binary hologram in the transmission station is constructed using one or more number of different Zernike modes. For each Zernike mode again multiple values of the co-efficients are used. Table 7.1 shows how a single Zernike mode (say $Z_{i1}$) can be used to represent the digits of a base-3 and base-5 number systems.

One may use three different $\Phi_{RMS}$ or five different $\Phi_{RMS}$ of two Zernike modes $Z_{i1}$ and $Z_{i2}$ to represent the digits of a base-9 and base-25 number systems as shown

**Table 7.1:** Table showing $\Phi_{RMS}$ of a single Zernike mode $Z_{i1}$ corresponding to base-3 and base-5 number systems.

| Base-n | digit | $\Phi_{RMS_1}$ in radian of $Z_{i1}$ |
|---|---|---|
| Base-3 | 0 | 0 |
| | 1 | 0.5 |
| | 2 | -0.5 |
| Base-5 | 0 | 0 |
| | 1 | 0.5 |
| | 2 | -0.5 |
| | 3 | 1 |
| | 4 | -1 |

in the table 7.2. The Zernike modes $Z_{i1}$ and $Z_{i2}$ are chosen which have least amount of inter-modal cross talk with respect to one another (discussed in chapter 5). In a similar manner the digits of a base-27 number systems can be obtained by using three different $\Phi_{RMS}$ of three Zernike modes, say $Z_{i1}$, $Z_{i2}$ and $Z_{i3}$. The resultant phase $\phi$ of the +1 order beam in the case three Zernike mode combinations can be written as $\phi = \Phi_{RMS_1} Z_{i1} + \Phi_{RMS_2} Z_{i2} + \Phi_{RMS_3} Z_{i3}$. Figure 7.3 illustrates how the

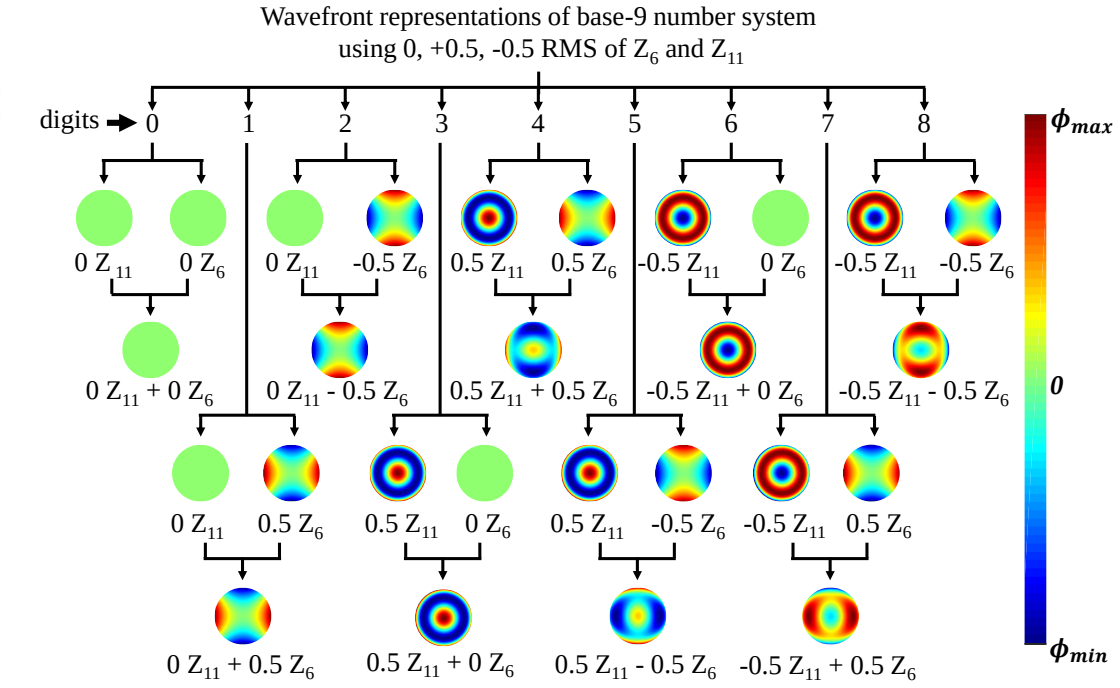


**Figure 7.3:** Wavefront representations of all the digits of base-9 number system using phase profiles in terms of 0, +0.5, -0.5 radian RMS amplitude of $Z_6$ and $Z_{11}$.

resultant phase profiles, representing the 9 digits of the base-9 number system, are obtained by combing two Zernike modes $Z_6$ and $Z_{11}$.

**Table 7.2:** Table showing $\Phi_{RMS}$ of two Zernike modes, $Z_{i1}$ and $Z_{i2}$ corresponding to base-9 and base-25 number systems.

| Base-n | digit | $\Phi_{RMS_1}$ in radian of $Z_{i1}$ | $\Phi_{RMS_2}$ in radian of $Z_{i2}$ |
|---|---|---|---|
| Base-9 | 0 | 0 | 0 |
| | 1 | 0 | 0.5 |
| | 2 | 0 | -0.5 |
| | 3 | 0.5 | 0 |
| | 4 | 0.5 | 0.5 |
| | 5 | 0.5 | -0.5 |
| | 6 | -0.5 | 0 |
| | 7 | -0.5 | 0.5 |
| | 8 | -0.5 | -0.5 |
| Base-25 | 0 | 0 | 0 |
| | 1 | 0 | 0.5 |
| | 2 | 0 | -0.5 |
| | 3 | 0 | 1 |
| | 4 | 0 | -1 |
| | 5 | 0.5 | 0 |
| | 6 | 0.5 | 0.5 |
| | 7 | 0.5 | -0.5 |
| | 8 | 0.5 | 1 |
| | 9 | 0.5 | -1 |
| | 10 | -0.5 | 0 |
| | 11 | -0.5 | 0.5 |
| | 12 | -0.5 | -0.5 |
| | 13 | -0.5 | 1 |
| | 14 | -0.5 | -1 |
| | 15 | 1 | 0 |
| | 16 | 1 | 0.5 |
| | 17 | 1 | -0.5 |
| | 18 | 1 | 1 |
| | 19 | 1 | -1 |
| | 20 | -1 | 0 |
| | 21 | -1 | 0.5 |
| | 22 | -1 | -0.5 |
| | 23 | -1 | 1 |
| | 24 | -1 | -1 |

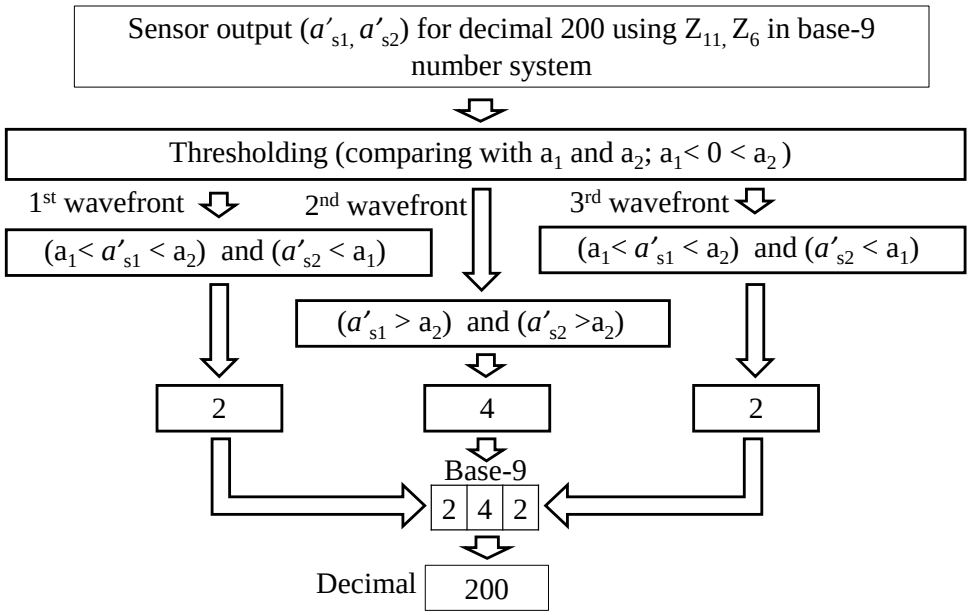


**Figure 7.4:** The decoding of a decimal number 200, sent as a base-9 number in the form of a wavefront comprising $Z_{11}$ and $Z_6$.

The beam incident on the type-K sensor therefore carries the phase profile $\phi$ which is a combination of one or more Zernike modes. Figure 7.4 depicts the decoding scheme for a laser beam carrying linear combination of two Zernike modes, $Z_{11}$ and $Z_6$, in the phase profile. The type-K sensor can simultaneously detect all the aberration modes present in the beam. Even though the type-K sensor provides an enhanced linear response, however, the estimated $\Phi_{RMS}$ may differ from the value used in the transmission station due to several reasons such as the separation between the $a_v$ values used in the type-K binary hologram. Let $a'_{s1}$ and $a'_{s2}$ be the estimated $\Phi_{RMS}$ for a given incident wavefront comprising a linear combination of $Z_{11}$ and $Z_6$. If the transmission station uses 0, or $\pm 0.5$ radian as the co-efficients, then the receiving station uses two values says $a_1$ and $a_2$ which are intermediate between -0.5 and 0 and between 0 and 0.5, respectively, to apply a thresholding on the sensor output. After thresholding a sensor output less than $a_1$ becomes -0.5, a sensor output above $a_2$ becomes 0.5, and a sensor output in between $a_1$ and $a_2$ becomes 0. The thresholded co-efficients of the two Zernike modes are then converted to the digital value of the respective base-n number system. The base-n numbers are then converted into decimal numbers to eventually retrieve the user data. The example depicted in Fig. 7.4 shows the decoding of decimal number 200 which was sent as a base-9 number using $Z_{11}$ and $Z_6$. Thresholded sensor outputs are mapped

to digits of base-9 number as show in table 7.2.

## 7.4 Experimental implementation

Figure 7.5 shows the schematic of the setup to implement the free space line of sight optical communication system inside the laboratory. A laser beam is expanded and collimated using two lenses $L_1$ and $L_2$, which is then incident on an FLCSLM. The FLCSLM displays a color image comprising 24 number of binary holograms. The FLCSLM display panel has a video rate of 60 Hz, such that each binary hologram has a net display time of $\frac{1000}{60\times24}$ millisecond (ms)=694 microsecond ($\mu$s). However the

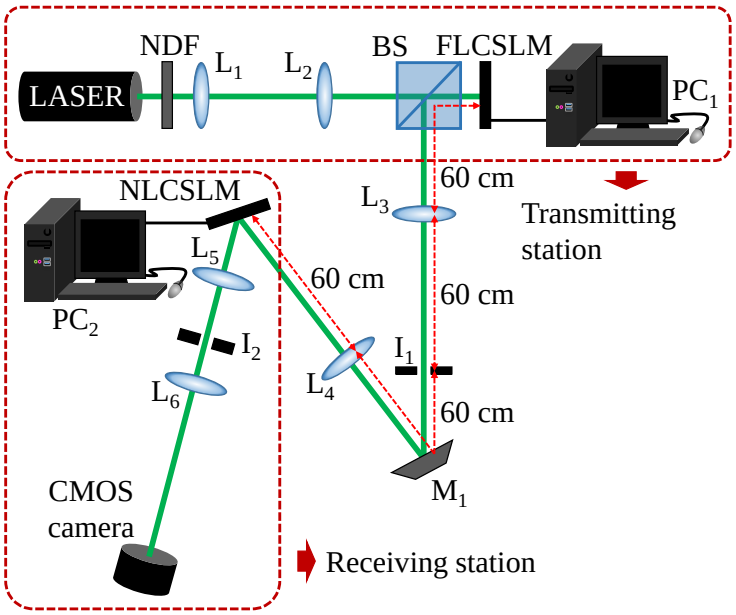


**Figure 7.5:** Schematic of the experimental arrangement to implement the free space optical communication system.

panel displays the exact binary hologram from almost half of this time and in the next half the FLCSLM displays the respective reverse binary hologram (a hologram with pixel values switched relative to the binary hologram). Thus effective display time of a binary hologram is approximately 340 $\mu$s, which can be termed as bit plane display time ($t_b$). Number of binary holograms displayed in one second which is in this case is 1440 is defined as the bit plane display frequency ($f_b$). Binary holograms are constructed using user defined object beam phase profiles such as a linear combination of multiple Zernike modes. The +1 order beam diffracted by the

FLCSLM is reflected by the beam splitter BS to direct it towards the free space. A neutral density filter NDF can be used to regulate the intensity level of the laser beam incident on the FLCSLM.

The +1 order beam carrying the user defined phase profiles at a frequency $f_b$ is incident on the type-K binary hologram displayed on an NLCSLM at the receiving station. We use two lenses $L_3$ and $L_4$, an iris $I_1$ and a mirror $M_1$ to relay the wavefront from the FLCSLM plane to the NLCSLM plane. The entire path, which constitutes the free space, in our case is equal to 2.4 m. The +1 order beams from the type-K binary hologram are focused on a CMOS camera with the help of lenses $L_5$, $L_6$ and an iris $I_2$.

The binary hologram in the transmission station is computed by $PC_1$ while the type-K binary hologram in the receiving station is computed by $PC_2$. The program in $PC_1$ can incorporate aberration correction in the +1 oder beam incident on the NLCSLM such that the beam carries primarily the user defined wavefront only. In order to measure each wavefront corresponding to every bit plane of the FLCSLM the CMOS camera should have a minimum frame rate of $f_b$. However due to limitation of our CMOS camera we can measure wavefront only at rate of $\frac{f_b}{4}$. Therefore the color image displayed in the FLCSLM comprises only 6 user defined binary holograms in 6 uniformly separated bit planes.

## 7.5 Results and discussion

We first generate a partially corrected +1 order beam by writing an appropriate binary hologram on the FLCSLM and the same is incident on the multiplex hologram displayed on the NLCSLM. Initially the multiplex hologram is designed to generate 30 +1 order focal spots in concentric circles without incorporating any aberrations and a reference focal spot also without any aberrations located at the centre of the said circles.

Figure 7.6 (i) shows 31 such focal spots captured by the CMOS camera. We then update the multiplex hologram to a type-K binary hologram for $Z_s = Z_6$ using $b = 0.7$ and $a_v$= [-1 -0.5 0 0.5 1]. The 30 number of +1 orders corresponding to $b = \pm 0.7$ for each $a_v$ value are distributed in concentric circles as seen in Fig. 7.6 (ii). However, even in the case of the type-K binary hologram, we keep the reference focal spot with 0 aberration incorporated at the centre of the pattern. Figure 7.6 (iii) shows similar focal spot pattern captured by the camera for $Z_s = Z_6$ and $a_v$=

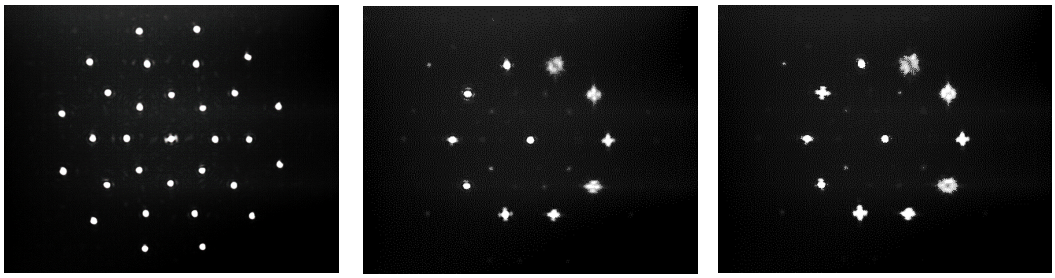

(i) (ii) (iii)

**Figure 7.6:** Focal spot patterns as captured by the CMOS camera showing (i) 31 focal spots with no additional aberrations, (ii) 11 focal spots from a type-K binary hologram using $Z_s = Z_6$, $b = 0.7$ and $a_v$= [-1 -0.5 0 0.5 1], and (iii) 11 focal spots from a type-K binary hologram using $Z_s = Z_6$, $b = 0.7$ and $a_v$= [-1.5 -0.75 0 0.75 1.5].

[-1.5 -0.75 0 0.75 1.5]. The type-K binary holograms corresponding to the focal spot patterns shown in Figs. 7.6 (ii) and (iii) are designed to measure wavefront encoded with base-3 and base-5 digits. We then update the type-K binary hologram

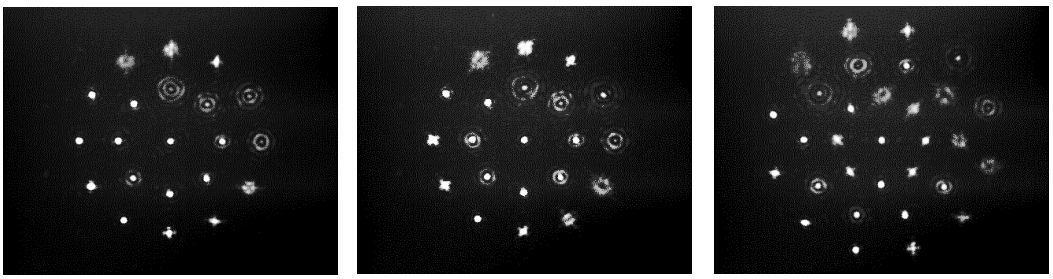

(i) (ii) (iii)

**Figure 7.7:** Focal spot patterns as captured by the CMOS camera corresponding to (i) $a_v$ = [-1 -0.5 0 0.5 1] and sensor modes $Z_6$ and $Z_{11}$, (ii) $a_v$ = [-1.5 -0.75 0 0.75 1.5] and sensor modes $Z_5$ and $Z_{11}$, and (iii) $a_v$ = [-1 -0.5 0 0.5 1] and sensor modes $Z_6$, $Z_{11}$ and $Z_5$, respectively.

to measure multiple sensor modes and Figs. 7.7 (i), (ii) and (iii) show the captured focal spots of the +1 orders using $a_v$ = [-1 -0.5 0 0.5 1], sensor modes $Z_6$ and $Z_{11}$; $a_v$ = [-1.5 -0.75 0 0.75 1.5], sensor modes $Z_5$ and $Z_{11}$; and $a_v$ = [-1 -0.5 0 0.5 1], sensor modes $Z_6$, $Z_{11}$ and $Z_5$, respectively. The type-K binary holograms corresponding to the focal spot patterns shown in Figs. 7.7 (i), (ii) and (iii) are designed to measure wavefront encoded with base-9, base-25 and base-27 digits.

We then examine the consistency of the type-K sensor outputs for three different sensor modes. A fixed wavefront comprising 0.5 radian of $Z_6$ is incident on the type-

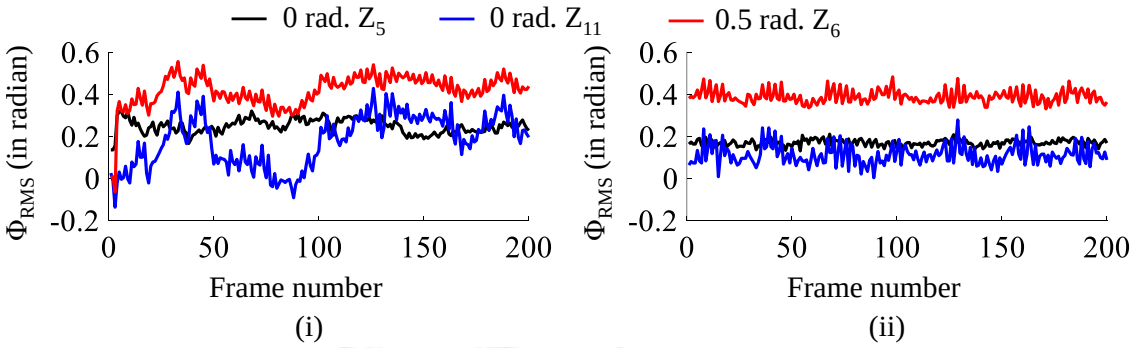


**Figure 7.8:** Sensor outputs of the type-K sensor, simultaneously detecting 3 sensor modes over several camera frames (i) before incorporating beam movement compensation and (ii) after incorporating beam movement compensation.

K sensor and the type-K binary hologram is designed for sensor modes $Z_6$, $Z_{11}$ and $Z_5$. As indicated by the plot in Fig. 7.8 (i), it is seen that even though the binary hologram in the FLCSLM incorporates $Z_5$=0, $Z_6$=0.5 radian, and $Z_{11}$=0 into the +1 order beam, the output of the type-K sensor for the same three sensor modes fluctuates over different camera frames. The variation in the sensor output is primarily due to beam movements caused by instability in the air in the propagation path and mechanical vibrations of the setup.

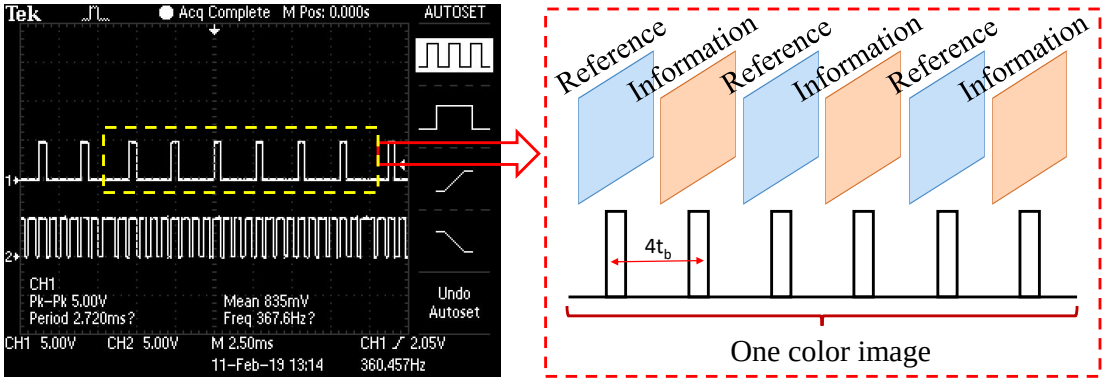


**Figure 7.9:** (i) Snapshot of the FLCSLM bit plane display timing and binary hologram display timings, and (ii) schematic showing the sequence of information wavefront and reference wavefront for beam movement compensation.

In order to compensate for the fluctuations in the sensor output, we modify the construction of the color image displayed on the FLCSLM. The color image

now comprises 3 binary holograms constructed using the user defined phase profiles and other 3 binary holograms constructed using a plane wave. Each information hologram is followed by a reference hologram. Figure 7.9 (i) shows the snapshot of the FLCSLM synchronization signal displaying timings of the inherent bit planes at a rate of 1440 Hz and the binary holograms at a rate of $\frac{f_b}{4}$. Figure 7.9 (ii) shows the sequence of information carrying holograms and the reference holograms. We use the +1 order beam locations of the type-K binary hologram corresponding to each reference wavefronts to calculate the effect of beam movements which is then used to compensate for such effect in the case of the wavefront carrying the user information. After employing this correction at a rate of $\frac{f_b}{8}$, the fluctuation in the type-K sensor output reduces significantly as seen in Fig. 7.8 (ii).

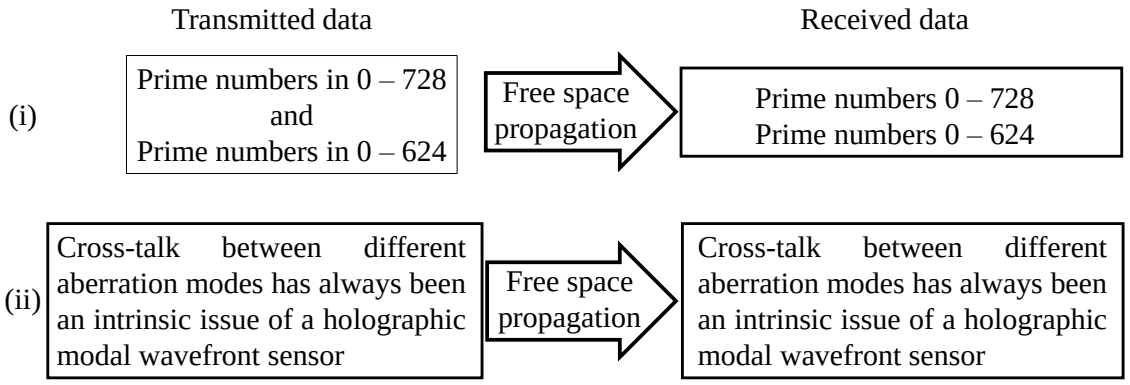


**Figure 7.10:** Schematic depicting the transmission of (i) numbers and (ii) text via the communication system.

In order the demonstrate the data transfer capability of the system, we then construct color images to carry the user information in the form of all the prime numbers lying between 0 and 728 (transmitted as base-3, base-9 and base-27 numbers) and between 0 and 624 (transmitted as base-5 and base-25 numbers). The information wavefronts are transmitted at the rate of $\frac{f_b}{8}$. As seen in Fig. 7.10 (i) we observe that the numbers are decoded with 100% accuracy. We also send some text message in a similar way and as seen in Fig. 7.10 (i) the text message also reaches the receiving station without any loss of information. We also read user provided images to construct color images for the transmission station and the pixel values are transmitted at the same rate as before. Figure 7.11 shows the transmitted image and received image, indicating that the image is received without any loss of

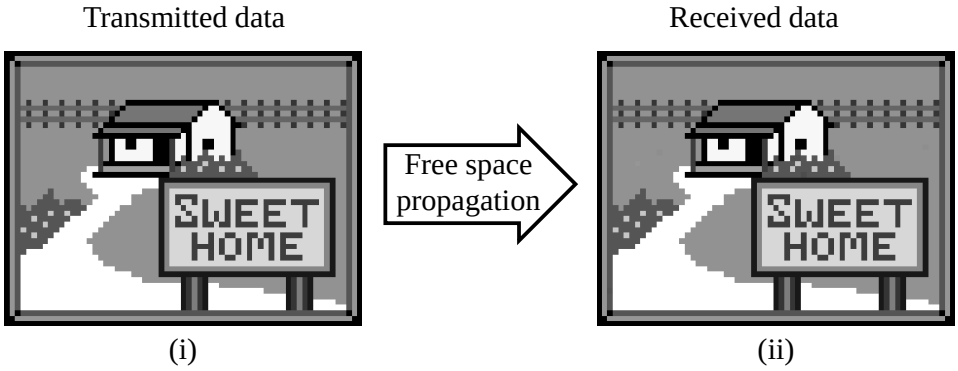


**Figure 7.11:** User image at the transmission station and the receiving station.

information. The user informations shown in Figs. 7.10 and 7.11 are transmitted separately using base-3, base-5, base-9, base-25 and base-27 numbers. The user data in all the cases are received with the same accuracy.

## 7.6 Conclusion

In this chapter we have applied our type-K modal wavefront sensor in a free space line of sight optical communication system. The optical communication system uses Zernike modes to encode the wavefront of a laser beam using appropriate binary holograms displayed on an FLCSLM. The beam travel a certain path in the laboratory environment before getting incident on a type-K sensor. The type-K sensor measures the strength of multiple Zernike modes present in the incident beam to decode the user information. We have also come up with scheme to minimize the external perturbation that effects the accuracy of the communication system. The results of our proof of principle setup demonstrates successful operation of the communication system inclusive of the type-K sensor.

# Chapter 8

# Conclusion and Future Prospects

## 8.1 Conclusion

The bias beam based modal wavefront sensor also referred to as the modal wavefront sensor has evolved as an important wavefront sensor due to its ability to measure an aberration mode directly. It is based on first dividing the incident beam into two identical copies of the incident beam having the same wavefront as the incident beam and of equal intensities. Certain amount of an aberration mode is deliberately added to one of the beams, resulting in the positive bias beam, and an equal amount of the same mode is subtracted from the other, resulting in the negative bias beam. Both the beams are then focused on to two point detectors using two lenses. The difference of the central intensities of these two focused beams gives a measure of the deliberately added aberration mode present in the incident beam. Thus, the modal wavefront sensor gives a direct measure of the amplitudes of the aberration modes present in an incident beam, contrary to a zonal wavefront sensor which requires a computationally intensive reconstruction algorithm to obtain the amplitudes of the aberration modes present in the incident beam. The modal wavefront sensor exploits the orthogonal properties of the aberration modes to get a measure of an aberration mode even when multiple aberration modes are present in the incident beam. The aberration modes in a beam can be conveniently represented by a set of orthogonal polynomials, known as the Zernike polynomials. Further, the use of computer generated holograms provides a simple way of implementing the modal wavefront sensor. The holograms facilitate the generation of a beam with a user-defined phase comprising Zernike modes made to travel in a user-defined direction. This property of

the hologram is used to generate the bias beams of a modal wavefront sensor. Such a modal wavefront sensor that is implemented using computer generated holograms is known as a holographic modal wavefront sensor. The modal wavefront sensor finds applications in diverse areas such as in adaptive optics, ophthalmology, optical shop testing, astronomy, microscopy, optical communication, etc. However there are a number of fundamental issues associated with the basic modal wavefront sensing scheme and issues associated in the holographic implementation of the sensor.

An important device used while implementing a holographic modal wavefront sensor is the liquid crystal spatial light modulator (LCSLM). LCSLM comprises a two-dimensional array of liquid crystal (LC) cells or pixels. The volume of each LC cell is filled with LC molecules which are effected by even a small change in ambient temperature. As the LCSLM is used to display the hologram that generates the bias orders, it is crucial that the diffracted beams remains steady along a fixed direction. However the temperature dependent property of the LC molecules leads to an undesirable beam movement over time which may lead to error in measurements. In this thesis we have first carried out a comprehensive study of the temperature dependent beam movements from an LCSLM. We have also come up with a means to minimize such unwanted beam movements from LCSLM.

The output of a modal wavefront sensor is affected by the presence of an aberration mode which is different from the mode to be measured. This effect, termed as the inter-modal cross talk, is important as the incident wavefront generally comprises multiple aberration modes. In the present thesis, an extensive study on the effect of inter-modal cross talk in a modal wavefront sensor has been carried out. We have developed an expression for the quick quantitative estimation of the effect of the inter-modal cross talk due to a certain input aberration mode on the various sensor aberration modes.

The modal wavefront sensor shows linear response up to a limited range of the sensor mode amplitude. Thus it can not give a direct measure of large aberration amplitudes. In this thesis, we have introduced a new modal wavefront sensing scheme that significantly improves the linear response range of the sensor. Besides the improvement is achieved without any compromise on the sensitivity and sensing speed of the sensor. Our modal wavefront sensor also reduces the inter-modal cross talk relative to the basic sensor. The proposed modal wavefront sensor is referred to as a type-K sensor. We have presented a detail theoretical analysis showing the improvements in terms of immunity to inter-modal cross talk and enhancement in

the linear response. Numerical simulations and experiments have also been carried out to assess the validity of the proposed scheme.

We have also presented an application of the proposed type-K sensor in a free space optical communication system. The communication system uses phase in terms of Zernike modes encoded laser beam to transfer information from one station (transmission station) to the other (receiving station). We have implemented the communication system experimentally and have presented some preliminary results.

## 8.2 Future prospects

A number of findings of the thesis work need further investigation and the techniques proposed can be developed further to be more effective. Below we briefly discuss a few such future works.

- In chapter 5 we have proposed an expression for quick computation of inter-modal cross talk when a maximum of two aberrations are present in the beam. However the beam comprise more number of aberration modes. Thus there is a need to further develop the expression to include effect of more than two aberration modes. Besides the present expression may also be used in an iterative manner to compensate for the effect of inter-modal cross talk when multiple aberration modes are present such that the actual aberration strengths are measured in relatively less number of iterations.

- In the present research work, we implemented the type-K sensor using LC-SLM (a dynamic phase modulating device) and a CMOS camera. In future the CMOS camera can be replaced by an array of photodetectors such as photomultiplier tubes (PMT), leading to increase in the sensing speed. Further, the type-K binary hologram displayed on the LCSLM can be replaced by a passive optical component such as hologram fabricated on a phase plate, which will reduce its implementation cost. One can also work towards blazed grating implementation of the type-K hologram instead of the type-K binary hologram, which will increase the diffraction efficiency of the bias beams making the sensor applicable even in tasks that require low light or that have low light.

- The free space optical communication system presented in the thesis is at the rudimentary stage. Thus the communication system has a great scope

of further improvement. For instance the transfer data rate can be increased by replacing the FLCSLM with a DMD and the CMOS camera by an array of photodetectors (such as PMT). Further, the communication link is set up over a very short distance and within the lab environment. The communication system can be implemented for larger distances and also in outside the laboratory environment.

# References


[1] Jacques M Beckers. Adaptive optics for astronomy: principles, performance, and applications. *Annual review of astronomy and astrophysics*, 31(1):13–62, 1993. 27

[2] Marcos Alejandro van Dam. Wave-front sensing for adaptive optics in astronomy. 2002. 27

[3] Daniel Malacara. *Optical shop testing*, volume 59. John Wiley & Sons, 2007. 27

[4] SA Potanin. Shack-hartmann wavefront sensor for testing the quality of the optics of the 2.5-m sai telescope. *Astronomy reports*, 53(8):703–709, 2009. 27

[5] Ralf B Schulz and Wolfhard Semmler. Fundamentals of optical imaging. In *Molecular Imaging I*, pages 3–22. Springer, 2008. 27

[6] Joel Kubby, Xiaodong Tao, and Oscar Azucena. Adaptive optics for biological imaging using direct wavefront sensing. In *Adaptive Optics: Methods, Analysis and Applications*, pages OM2A–4. Optical Society of America, 2013. 27

[7] Martin J Booth. Adaptive optics in microscopy. *Philosophical Transactions of the Royal Society A: Mathematical, Physical and Engineering Sciences*, 365 (1861):2829–2843, 2007. 27

[8] Xiaodong Tao, Bautista Fernandez, Oscar Azucena, Min Fu, Denise Garcia, Yi Zuo, Diana C Chen, and Joel Kubby. Adaptive optics confocal microscopy using direct wavefront sensing. *Optics letters*, 36(7):1062–1064, 2011. 27

[9] S MacRae, James Schwiegerling, and Robert Snyder. Customized corneal ablation and super vision. *Journal of Refractive Surgery*, 16(2; SUPP/1):S230–S235, 2000. 27

[10] Mahnaz Shahidi, Norman P Blair, Marek Mori, and Ruth Zelkha. Optical section retinal imaging and wavefront sensing in diabetes. *Optometry & Vision Science*, 81(10):778–784, 2004. 27

[11] Martin J Booth, Michael Schwertner, Tony Wilson, Masaharu Nakano, Yoshimasa Kawata, Masahito Nakabayashi, and Sou Miyata. Predictive aberration correction for multilayer optical data storage. *Applied physics letters*, 88(3): 031109, 2006. 27

[12] Daniel R Neal, Timothy J O'Hern, John R Torczynski, Mial E Warren, Randy J Shul, and TS McKechnie. Wavefront sensors for optical diagnostics in fluid mechanics: application to heated flow, turbulence, and droplet evaporation. In *SPIE's 1993 International Symposium on Optics, Imaging, and Instrumentation*, pages 194–203. International Society for Optics and Photonics, 1993. 27

[13] Thomas Weyrauch and Mikhail A Vorontsov. Free-space laser communications with adaptive optics: Atmospheric compensation experiments. *Journal of Optical and Fiber Communications Reports*, 1(4):355–379, 2004. 27, 136

[14] Feng Feng, Ian H White, and Timothy D Wilkinson. Aberration correction for free space optical communications using rectangular zernike modal wavefront sensing. *Journal of Lightwave Technology*, 32(6):1239–1245, 2014. 27, 29, 55

[15] SM Zhao, J Leach, LY Gong, J Ding, and BY Zheng. Aberration corrections for free-space optical communications in atmosphere turbulence using orbital angular momentum states. *Optics express*, 20(1):452–461, 2012. 27

[16] Max Born and Emil Wolf. Principles of optics, 7th (expanded) ed. *Cambridge U. Press, Cambridge, UK*, 890, 1999. 28, 36, 42

[17] Guang-Ming Dai. Zernike aberration coefficients transformed to and from fourier series coefficients for wavefront representation. *Optics letters*, 31(4): 501–503, 2006. 28

[18] Robert J Noll. Zernike polynomials and atmospheric turbulence. *JOsA*, 66(3): 207–211, 1976. 28, 42

[19] M De and LN Hazra. Walsh functions in problems of optical imagery. *Optica Acta: International Journal of Optics*, 24(3):221–234, 1977. 28

[20] Ben C Platt and Roland Shack. History and principles of shack-hartmann wavefront sensing. *Journal of refractive surgery*, 17(5):S573–S577, 2001. 28, 48

[21] Bertrand P Ramsay. A grating interferometer. *JOSA*, 24(9):253–258, 1934. 28

[22] Jerome Primot. Three-wave lateral shearing interferometer. *Applied optics*, 32 (31):6242–6249, 1993. 28

[23] Francois Roddier, Claude Roddier, and Nicolas Roddier. Curvature sensing: a new wavefront sensing method. In *Statistical Optics*, volume 976, pages 203–210. International Society for Optics and Photonics, 1988. 28, 49

[24] Roberto Ragazzoni. Pupil plane wavefront sensing with an oscillating prism. *Journal of modern optics*, 43(2):289–293, 1996. 28

[25] Mark AA Neil, Martin J Booth, and Tony Wilson. New modal wave-front sensor: a theoretical analysis. *JOSA A*, 17(6):1098–1107, 2000. 28, 30, 49, 52, 121

[26] Carl Paterson and JC Dainty. Hybrid curvature and gradient wave-front sensor. *Optics letters*, 25(23):1687–1689, 2000. 28

[27] William H Southwell. Wave-front estimation from wave-front slope measurements. *JOSA*, 70(8):998–1006, 1980. 28, 49

[28] Biswajit Pathak and Bosanta R Boruah. Improved wavefront reconstruction algorithm for shack–hartmann type wavefront sensors. *Journal of Optics*, 16 (5):055403, 2014. 28, 49

[29] Martin J Booth. Direct measurement of zernike aberration modes with a modal wavefront sensor. In *Advanced Wavefront Control: Methods, Devices, and Applications*, volume 5162, pages 79–91. International Society for Optics and Photonics, 2003. 28, 29, 55

[30] Mark AA Neil, Martin J Booth, and Tony Wilson. Closed-loop aberration correction by use of a modal zernike wave-front sensor. *Optics letters*, 25(15): 1083–1085, 2000. 29

[31] Martin J Booth, Mark AA Neil, Rimas Juškaitis, and Tony Wilson. Adaptive aberration correction in a confocal microscope. *Proceedings of the National Academy of Sciences*, 99(9):5788–5792, 2002. 29

[32] Alexander D Corbett, Timothy D Wilkinson, Jiang J Zhong, and Luis Diaz-Santana. Designing a holographic modal wavefront sensor for the detection of static ocular aberrations. *JOSA A*, 24(5):1266–1275, 2007. 29

[33] Michael J Wilby, Christoph U Keller, Frans Snik, Visa Korkiakoski, and Alexander GM Pietrow. The coronagraphic modal wavefront sensor: a hybrid focal-plane sensor for the high-contrast imaging of circumstellar environments. *Astronomy & Astrophysics*, 597:A112, 2017. 29

[34] Florian Loosen, Johannes Stehr, Lucas Alber, Irina Harder, and Norbert Lindlein. A holography-based modal wavefront sensor for the precise positioning of a light emitter using a high-resolution computer-generated hologram. *IEEE Photonics Journal*, 10(1):1–11, 2018. 29, 73

[35] Sanjay K Mishra, Rahul Bhatt, Devendra Mohan, Arun Kumar Gupta, and Anurag Sharma. Differential modal zernike wavefront sensor employing a computer-generated hologram: a proposal. *Applied optics*, 48(33):6458–6465, 2009. 29, 55

[36] Sanjay Kumar Mishra, Arun Kumar Gupta, and Anurag Sharma. An ocular wavefront sensor based on binary phase element: design and analysis. *Journal of Modern Optics*, 59(12):1034–1048, 2012. 29, 55

[37] Shihao Dong, Tobias Haist, Wolfgang Osten, Thomas Ruppel, and Oliver Sawodny. Response analysis of holography-based modal wavefront sensor. *Applied optics*, 51(9):1318–1327, 2012. 29, 55

[38] Fanpeng Kong and Andrew Lambert. Improvements to the modal holographic wavefront sensor. *Applied optics*, 55(13):3615–3625, 2016. 29, 56

[39] Lifa Hu, Li Xuan, Yongjun Liu, Zhaoliang Cao, Dayu Li, and QuanQuan Mu. Phase-only liquid-crystal spatial light modulator for wave-front correction with high precision. *Optics express*, 12(26):6403–6409, 2004. 30

[40] Joseph W Goodman. *Introduction to Fourier optics*. Roberts and Company Publishers. 38, 59, 61, 64, 77, 79

[41] Virendra N Mahajan. Zernike polynomials and aberration balancing. In *Current Developments in Lens Design and Optical Engineering IV*, volume 5173, page 517302. International Society for Optics and Photonics, 2003. 40

[42] Frits Zernike. Diffraction theory of the knife-edge test and its improved form, the phase-contrast method. *Monthly Notices of the Royal Astronomical Society*, 94:377–384, 1934. 42

[43] Virendra N Mahajan. Zernike circle polynomials and optical aberrations of systems with circular pupils. *Applied optics*, 33(34):8121–8124, 1994. 42

[44] Eric P Goodwin and James C Wyant. Field guide to interferometric optical testing. SPIE Bellingham, WA, 2006. 45

[45] Francois Roddier. Wavefront sensing and the irradiance transport equation. *Applied optics*, 29(10):1402–1403, 1990. 50

[46] Esdras Anzuola, Andreas Zepp, Szymon Gladysz, and Karin Stein. Holographic wavefront sensor based on karhunen-loève decomposition. In *Laser Communication and Propagation through the Atmosphere and Oceans V*, volume 9979, page 99790X. International Society for Optics and Photonics, 2016. 56

[47] Parameswaran Hariharan. *Basics of holography*. Cambridge university press, 2002. 60

[48] BR Boruah. Dynamic manipulation of a laser beam using a liquid crystal spatial light modulator. *American Journal of Physics*, 77(4):331–336, 2009. 65, 67

[49] Ranjan Kalita, Md Gaffar, and Bosanta R Boruah. The generation of arbitrary vector beams using a division of a wavefront-based setup. *Journal of Optics*, 18(7):075604, 2016. 66

[50] Frank L Pedrotti, Leno M Pedrotti, and Leno S Pedrotti. *Introduction to optics*. Cambridge University Press, 2017. 66

[51] Harry Nyquist. Certain topics in telegraph transmission theory. *Transactions of the American Institute of Electrical Engineers*, 47(2):617–644, 1928. 67

[52] Uzi Efron. *Spatial light modulator technology: materials, devices, and applications*, volume 47. CRC Press, 1994. 76, 77, 79, 83

[53] Holoeye. *LC-R 720*. URL `https://holoeye.com/spatial-light-modulators/discontinued-devices/`. 78

[54] 4D Display. *SXGA-R3*. URL `https://www.forthdd.com/products/`. 80

[55] Benjamin Lee. Introduction to±12 degree orthogonal digital micromirror devices (dmds). *Texas Instrument Incorporated*, 3, 2018. 80

[56] Texas Instruments. *DLP9000*. URL `http://www.ti.com/product/DLP9000`. 80

[57] Willard S Boyle and George E Smith. Charge coupled semiconductor devices. *Bell System Technical Journal*, 49(4):587–593, 1970. 81

[58] Abbas El Gamal and Helmy Eltoukhy. Cmos image sensors. *IEEE Circuits and Devices Magazine*, 21(3):6–20, 2005. 81

[59] Thorlab. *USB 3.0 CMOS camera*. URL `https://www.thorlabs.com/newgrouppage9.cfm?objectgroup_id=4024`. 81

[60] Basler. *A504K User's manual*. Basler, 2012. 81

[61] Spectra-Physics. *Excelsior-532-200-CDRH*. URL `https://www.spectra-physics.com/products/cw-lasers/excelsior`. 82

[62] Melles Griot. *05-LHR-991*. URL `https://www.global-optosigma.com/en_jp/Catalogs/gno/?from=page&pnoname=05-LHP&ccode=W5002&dcode=&gnoname=05-LHP-991`. 82

[63] Santanu Konwar and Bosanta R Boruah. Observation of thermally induced movement of a beam deflected by a liquid crystal spatial light modulator. In *SPIE OPTO*, pages 976915–976915. International Society for Optics and Photonics, 2016. 83

[64] Santanu Konwar and Bosanta R Boruah. Note: Current induced fluctuations in the orientation of the beam diffracted by a liquid crystal spatial light modulator. *Review of Scientific Instruments*, 88(6):066104, 2017. 83

[65] Juan Carlos Torres, Braulio García-Cámara, Isabel Pérez, Virginia Urruchi, and José Manuel Sánchez-Pena. Temperature-phase converter based on a lc cell as a variable capacitance. *Sensors*, 15(3):5594–5608, 2015. 83

[66] IC Khoo, SL Zhuang, and S Shepard. Self-focusing of a low power cw laser beam via optically induced birefringence in a nematic liquid-crystal film. *Applied Physics Letters*, 39(12):937–940, 1981. 83

[67] Hideki Ono, Kazuhiko Takeda, and Kitao Fujiwara. Thermal lens produced in a nematic liquid crystal. *Applied spectroscopy*, 49(8):1189–1192, 1995. 83

[68] Jeroen Beeckman, Katarzyna Chałubińska, and Kristiaan Neyts. Lateral light propagation in ssflc devices and thermal optical nonlinearities. *Ferroelectrics*, 344(1):225–231, 2006. 83

[69] Satoshi Inoue, Hiroyuki Ohshima, and Tatsuya Shimoda. Analysis of degradation phenomenon caused by self-heating in low-temperature-processed polycrystalline silicon thin film transistors. *Japanese journal of applied physics*, 41 (11R):6313, 2002. 88

[70] Shinichiro Hashimoto, Yukiharu Uraoka, Takashi Fuyuki, and Yukihiro Morita. Analysis of thermal distribution in low-temperature polycrystalline silicon p-channel thin film transistors. *Japanese journal of applied physics*, 45(1R):7, 2006. 88

[71] Y Yin, Sergij V Shiyanovskii, and OD Lavrentovich. Electric heating effects in nematic liquid crystals. *Journal of applied physics*, 100(2):024906, 2006. 89, 90

[72] Jun Li, Sebastian Gauzia, and Shin-Tson Wu. High temperature-gradient refractive index liquid crystals. *Optics express*, 12(9):2002–2010, 2004. 89

[73] Fuzi Yang, JR Sambles, and GW Bradberry. Measurement of the refractive indices of a ferroelectric liquid crystal. *Journal of applied physics*, 78(4):2187–2192, 1995. 89

[74] JH Wray and John T Neu. Refractive index of several glasses as a function of wavelength and temperature. *JOSA*, 59(6):774–776, 1969. 91

[75] Santanu Konwar and Bosanta R Boruah. An analytical study on the presence of inter-modal cross-talk in a modal wavefront sensor. In *Unconventional and Indirect Imaging, Image Reconstruction, and Wavefront Sensing 2018*, volume 10772, page 107720A. International Society for Optics and Photonics, 2018. 99

[76] Santanu Konwar and Bosanta R Boruah. Estimation of inter-modal cross talk in a modal wavefront sensor. *OSA Continuum*, 1(1):78–91, 2018. 103

[77] Santanu Konwar and Bosanta R Boruah. Improvement in modal wavefront sensing in terms of cross-talk reduction and linearity. In *Unconventional and*

*Indirect Imaging, Image Reconstruction, and Wavefront Sensing 2018*, volume 10772, page 107720D. International Society for Optics and Photonics, 2018. 115

[78] Santanu Konwar and Bosanta R Boruah. Improved linear response in a modal wavefront sensor. *JOSA A*, 36(5):741–750, 2019. 116

[79] Richard Hamming. *Numerical methods for scientists and engineers*. Courier Corporation, 2012. 120

[80] Vincent WS Chan. Free-space optical communications. *Journal of Lightwave technology*, 24(12):4750–4762, 2006. 135

[81] Vincent WS Chan. Optical satellite networks. *Journal of Lightwave Technology*, 21(11):2811, 2003. 135

[82] WS Vincent. Coherent optical space communications system architecture and technology issues. In *Control and communication technology in laser systems*, volume 295, pages 10–18. International Society for Optics and Photonics, 1981. 135

[83] Tobias Schmitt-Manderbach, Henning Weier, Martin Fürst, Rupert Ursin, Felix Tiefenbacher, Thomas Scheidl, Josep Perdigues, Zoran Sodnik, Christian Kurtsiefer, John G Rarity, et al. Experimental demonstration of free-space decoy-state quantum key distribution over 144 km. *Physical Review Letters*, 98 (1):010504, 2007. 135

[84] B Martin Levine, Elizabeth A Martinsen, Allan Wirth, Andrew Jankevics, Manuel Toledo-Quinones, Frank Landers, and Theresa L Bruno. Horizontal line-of-sight turbulence over near-ground paths and implications for adaptive optics corrections in laser communications. *Applied optics*, 37(21):4553–4560, 1998. 136

[85] Charles A Primmerman, Thomas R Price, Ronald A Humphreys, Byron G Zollars, Herbert T Barclay, and Jan Herrmann. Atmospheric-compensation experiments in strong-scintillation conditions. *Applied Optics*, 34(12):2081–2088, 1995. 136

[86] F Javier Lopez-Martinez, Gerardo Gomez, and José María Garrido-Balsells. Physical-layer security in free-space optical communications. *IEEE Photonics Journal*, 7(2):1–14, 2015. 136

[87] Geraldo A Barbosa, Eric Corndorf, Prem Kumar, and Horace P Yuen. Secure communication using mesoscopic coherent states. *Physical Review Letters*, 90 (22):227901, 2003. 136

[88] Valerio Annovazzi-Lodi, Giuseppe Aromataris, Mauro Benedetti, and Sabina Merlo. Secure chaotic transmission on a free-space optics data link. *IEEE journal of quantum electronics*, 44(11):1089–1095, 2008. 136

[89] Ning Wang, Xuegui Song, Julian Cheng, and Victor CM Leung. Enhancing the security of free-space optical communications with secret sharing and key agreement. *IEEE/OSA Journal of Optical Communications and Networking*, 6 (12):1072–1081, 2014. 136

[90] Graham Gibson, Johannes Courtial, Miles J Padgett, Mikhail Vasnetsov, Valeriy Pasko, Stephen M Barnett, and Sonja Franke-Arnold. Free-space information transfer using light beams carrying orbital angular momentum. *Optics express*, 12(22):5448–5456, 2004. 136

[91] Yongxiong Ren, Zhe Wang, Peicheng Liao, Long Li, Guodong Xie, Hao Huang, Zhe Zhao, Yan Yan, Nisar Ahmed, Asher Willner, et al. Experimental characterization of a 400 gbit/s orbital angular momentum multiplexed free-space optical link over 120 m. *Optics letters*, 41(3):622–625, 2016. 136

[92] Long Li, Runzhou Zhang, Zhe Zhao, Guodong Xie, Peicheng Liao, Kai Pang, Haoqian Song, Cong Liu, Yongxiong Ren, Guillaume Labroille, et al. High-capacity free-space optical communications between a ground transmitter and a ground receiver via a uav using multiplexing of multiple orbital-angular-momentum beams. *Scientific reports*, 7(1):17427, 2017. 136

[93] Martin PJ Lavery. Vortex instability in turbulent free-space propagation. *New Journal of Physics*, 20(4):043023, 2018. 136

# Patents and Publications

**(a) Patents:**

1. **Santanu Konwar** and Bosanta R Boruah, "Free space optical communication system apparatus and a method thereof", Patent Application No.: PCT/IB2016/054233, July 15, 2016; Publication number: WO 2017/009808, January 19, 2017 (International).

2. **Santanu Konwar** and Bosanta R Boruah, "Free space optical communication system apparatus and a method thereof", Patent Application No.: 2153/DEL/2015, July 15, 2015 (National).

**(b) Journals and Proceedings:**

1. **Santanu Konwar** and Bosanta R Boruah, "Steady information transfer through free-space employing orthogonal aberration mode division multiplexing", arXiv preprint arXiv:1910.02019 (2019).

2. **Santanu Konwar** and Bosanta R Boruah, "Improved linear response in a modal wavefront sensor", J. Opt. Soc. Am. A 36, 741-750 (2019).

3. **Santanu Konwar** and Bosanta R Boruah, "Improvement in modal wavefront sensing in terms of cross-talk reduction and linearity", Proc. SPIE, 107720D (2018).

4. **Santanu Konwar** and Bosanta R Boruah, "An analytical study on the presence of inter-modal cross-talk in a modal wavefront sensor", Proc. SPIE, 107720A (2018).

5. **Santanu Konwar** and Bosanta R Boruah, "Estimation of inter-modal cross talk in a modal wavefront sensor", OSA Continuum 1, 78-91 (2018).

6. **Santanu Konwar** and Bosanta R Boruah, "Note: Current induced fluctuations in the orientation of the beam diffracted by a Liquid Crystal Spatial Light Modulator", Review of Scientific Instruments 88, 066104 (2017).

7. **Santanu Konwar** and Bosanta R Boruah, "Observation of thermally induced movement of a beam deflected by a liquid crystal spatial light modulator", Proc. SPIE, 976915 (2016).

**(c) Conference Presentations:**

1. "An analytical study on the presence of inter-modal cross-talk in a modal wavefront sensor", **Santanu Konwar** and Bosanta R Boruah, at SPIE Optics + Photonics, Convention Center, San Diego, United States (19 - 23 August, 2018).

2. "Improvement in modal wavefront sensing in terms of cross-talk reduction and linearity", **Santanu Konwar** and Bosanta R Boruah, at SPIE Optics + Photonics, Convention Center, San Diego, United States (19 - 23 August, 2018).

3. "Modal Wavefront sensing with reduced cross-talk and improved accuracy in detecting static aberrations", **Santanu Konwar** and Bosanta R Boruah, at the International Conference on Advances in Optics and Photonics (ICAOP-17), Guru Jambheshwar University of Science and Technology, Haryana, India (23 - 26 November, 2017).

4. "Wavefront sensing and computer generated holography: some basic concepts" (**Invited Talk**), **Santanu Konwar**, at the UGC sponsored National Workshop on Recent Trands in Physical Science Research, Silapathar Science College, Assam, India (21 - 22 October 2017).

5. "Analysis of the Inter-modal Cross-talk in a Modal Wavefront Sensor", **Santanu Konwar** and Bosanta R Boruah, at the International Topical Meeting on APPLIED AND ADAPTIVE OPTICS (INTOPMAA-17), Indian Institute of Space Science Technology (IIST), Kerala, India (11 - 13 August, 2017).

6. "Study of cross-talk in the detection of various Zernike modes by a Modal Wavefront Sensor", **Santanu Konwar** and Bosanta R Boruah, at the National Seminar on Advances in Electronics and Allied Science and Technology (NaSAEAST-2017), Gauhati University, Assam, India (27 - 28 June 2017).

7. "Liquid Crystal Spatial Light Modulator based Wavefront sensing and its application", **Santanu Konwar**, Biswajit Pathak and Bosanta R Boruah, at the Research conclave'17, IIT Guwahati, Assam, India (16 - 19 March, 2017).

8. "Fluctuations in the orientation of the beam diffracted by a Liquid Crystal Spatial Light Modulator", **Santanu Konwar** and Bosanta R Boruah, at the International Conference on Light and Light based Technologies (ICLLT), Tezpur University, Assam, India (26 - 28 November, 2016).

9. "Propagation of aberrated beam through atmospheric turbulence", presented at the International Conference on Light and Light based Technologies (ICLLT), **Santanu Konwar** and Bosanta R Boruah, Tezpur University, Assam, India (26 - 28 November, 2016).

10. "Observation of a peculiar movement in the beam diffracted by a Liquid Crystal Spatial Light Modulator", **Santanu Konwar** and Bosanta R Boruah, at the National Seminar on Advances in Electronics and Allied Science and Technology (NaSAEAST-2016), Gauhati University, Assam, India (4 - 5 November 2016).

11. "Wavefront Sensing using Computer Generated Holography Technique", Nagendra Kumar, **Santanu Konwar**, Biswajit Pathak and Bosanta R Boruah, at the Research conclave'16, IIT Guwahati, Assam, India (17 - 20 March, 2016).

12. "Observation of thermally induced movement of a beam deflected by a liquid crystal spatial light modulator", **Santanu Konwar** and Bosanta R Boruah, at Photonics West, California, USA, (16 - 18 February, 2016).

13. "Comparative Study on the Performance of the Multiplex and Singlex Hologram Based Modal Wavefront Sensor", **Santanu Konwar** and Bosanta R Boruah, at the South Asian Workshop on Optics and Photonics (SAWOP-2015), IIT Guwahati, Assam, India (17 - 18 November, 2015)

14. "Hologram Based Wavefront Sensor of Light Beams", **Santanu Konwar** and Bosanta R Boruah, at the TEQIP Symposium to Celebrate the 2015 International Year of Light, IIT Guwahati, Assam, India (31 October 2015).

15. "Simultaneous detection of Zernike modes present in a laser beam with a high frame rate modal wavefront sensor", **Santanu Konwar** and Bosanta R Boruah, at the International Conference on Optics and Photonics (ICOP-2015), University of Calcutta, West Bengal, India (20 - 22 February 2015).

**(d) Schools/Workshops attended:**

1. One Day Workshop on Vacuum Technology and Its application In Optical Science, at IIT Guwahati, Assam, India (19 September, 2017).
2. Workshop on Intellectual Property Right, at IIT Guwahati, at IIT Guwahati, Assam, India (30 November - 1 December, 2016).
3. 3rd IEEE Workshop on Advanced MATLAB Application - "ADMAT 2016", at IIT Guwahati, organized by IEEE student branch IIT Guwahati, Assam, India (1 - 2 October, 2016).
4. SERB School on Optical Metrology, at Tezpur University, Assam, India (1 - 21 June, 2016).
5. SERB School on Modern Optics and Its Application, at IIT Patna, Bihar, India (30 November - 18 December, 2015).
6. IEEE Workshop on "Power, Mechatronics, Robotics and Control" (PMRC2015), at IIT Guwahati, Assam, India (29 and 30 August, 2015).

**(e) Achievements (Related to Ph. D Work):**

1. Received **"SPIE Student Author Travel Grants" (USD 1150)** to present two contributory papers at SPIE Optics + Photonics at San Diego, California, United States from 19 - 23 August, 2018, organized by SPIE.
2. Received **Departmental (Physics) best poster award** for the poster entitled "Liquid crystal spatial light modulator based wavefront sensing and its application", at the Research Conclave'17 organized by IIT Guwahati, Assam, India (2017).
3. Received **OSA (Optical Society of America) best contributory paper award** in the poster session for the paper entitled "Propagation of aberrated beam through atmospheric turbulence", at the International Conference on

Light and Light based Technologies (ICLLT) held at Tezpur University, Assam, India (2016).

4. Received **Departmental (Physics) 1st runner-up** for the poster entitled "Wavefront sensing using computer generated holography technique", at the Research Conclave'16 organized by IIT Guwahati, Assam, India (2016).

***